Exploring Low Dimensions: Building Novel Superconducting Nanodevices to Discover New Physics

by

Tyler Morgan-Wall

A dissertation submitted to The Johns Hopkins University in conformity with the requirements for the degree of Doctor of Philosophy.

Baltimore, Maryland

May, 2015

© Tyler Morgan-Wall 2015

All rights reserved

Abstract

This thesis reports on experimental progress in the understanding of superconducting transport properties of low-dimensional nano-structures, focused on lithographically produced aluminum nanowires. The nanowires were studied using transport measurements at temperatures down to 0.25K. A new method is presented on lithographically fabricating one-dimensional nanowires with high control over the final size and size of the wire, enabling the production of wires in a new size regime.

Evidence for Weber blockade, a new type of "vortex quantum dot," is presented for superconducting nanowires. The evidence for this new effect will enable better understanding and control over future superconducting devices that employ vortex dynamics in their operation. Finally, evidence for the various features of vortex transport in thin, narrow superconducting nanowires is shown.

This work was conducted under the supervision of Professor Nina Markovic.

Reader: Professor Nina Markovic

Acknowledgments

First and foremost, I would like to thank my advisor, Prof. Nina Marković, for all of her help and guidance in my years here. I wouldn't have had nearly as enriching an experience as I did if not for her patience, steadfastness in a face of adversity, and commitment to producing quality research. I would also like to thank Prof. Tyrel McQueen, whose knowledge and input was invaluable both in my oral exams as well as in my research.

In addition, I would like to thank all of the lab mates who I have worked with over the years. Nik Hartman in particular, for being there with me in maintaining an entire cryogenic measurement and fabrication facility by ourselves, as well as always being up for talking shop and troubleshooting whatever needed troubleshooting. I want to thank Atikur Rahman and Soo Hyung Lee for their part in helping teach me the basics of fabrication and measurement. In addition, I would also like to thank all of the talented undergrads I have had the pleasure to work closely with over the years: Katie Sparks, Benjamin Leith, and Hannah Hughes.

Finally, I would like to thank everyone that supported me outside of the lab.

ACKNOWLEDGMENTS

Starting with my family for supporting and encouraging me to pursue my passion in science (and more tangibly: for paying my cellphone bill). I'd like to thank my incredible cohorts who came in with me at Johns Hopkins in 2009 and who have all supported one another through the whole graduate school process. I'd also like to thank my Philadelphia and Baltimore friends who kept me sane and grounded when work was tough, and whose enthusiasm and support made the good moments that much better. And finally, I'd like to thank my amazingly intelligent and incredibly supportive fiancée, Pamela Dopart, for being along with me on this journey through long nights in the lab and long days spent staring at my data. I would be a lesser man without your love and support.

Contents

List of Figures

Chapter 1

Introduction

Superconductivity was discovered in 1911 by Kamerlingh Onnes in his attempt to measure the resistance of mercury at cryogenic temperatures.[1] At the time, it was not known what would happen to a metal's resistance as temperature approached zero. As the temperature was lowered, the resistance unexpectedly dropped to down to zero (see Figure 1.1). Perfect conductivity was the first and most striking feature of superconductivity discovered. This dramatic change was immediately recognized as a change in the phase of the material, but the details of why it occurred would remain a relative mystery for half a century.

A superconductor is more than just a good conductor. A superconductor differs from a perfect conductor in that magnetic fields are actively expelled from the interior of the superconductor after the temperature drops below T_C, while a material that transitioned to perfect conductor would only lock the existing fields in place. The

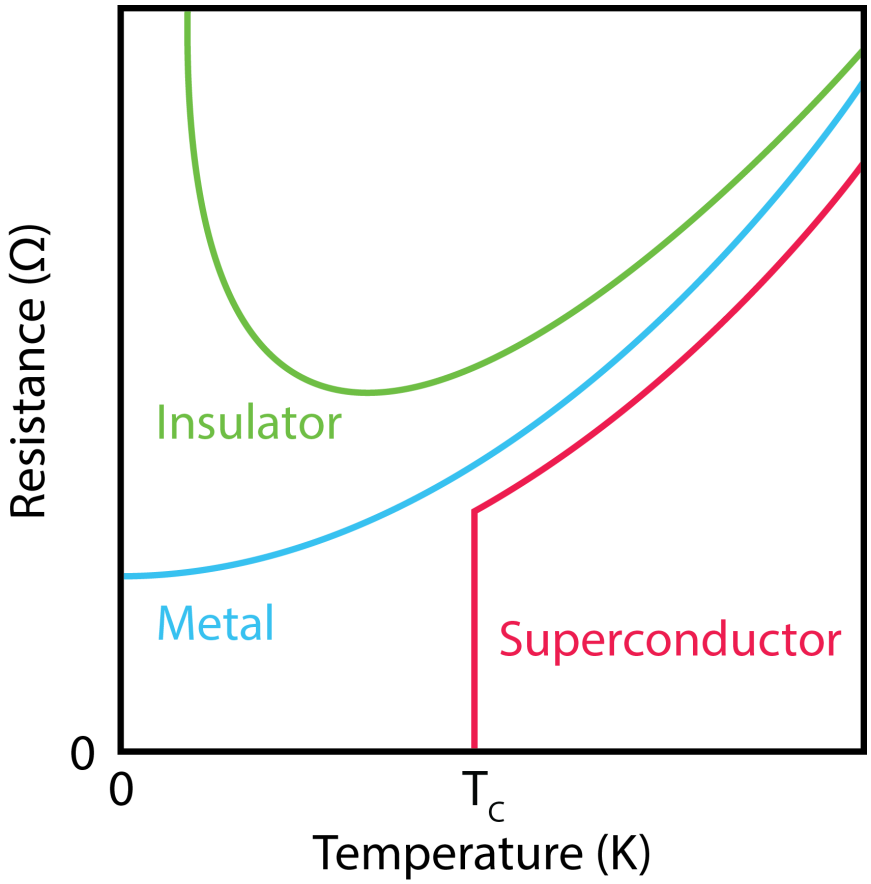

Figure 1.1: Behavior of insulators, metals, and superconductors as T→ 0. As T approaches 0K for a metal (blue), it levels out at a finite value. For an insulator (green), the resistance tends to infinity, and for a superconductor (red) it drops to zero at some temperature T_C.

superconductor actively expels fields up to some critical field H_C, after which it returns to its normal state. This aspect of perfect diamagnetism is called the Meissner effect,[2] and this particular property and superconductivity's interaction with magnetic fields is where much of the rich phenomena of superconductivity arises.

Understanding superconductivity has inspired generations of both experimental and theoretical physicists due to the wide range of applications superconductivity enables. The absence of resistance enables the lossless transfer of current across long distances. It also allows the creation of high-field superconducting magnets which can produce magnetic fields an order of magnitude larger than magnets made from regular conductors. The latter property by itself has enabled everything from the creation of MRIs to find tumors without radiation exposure to the massive particle accelerator that found the Higgs boson.

More recently, utilizing superconducting materials in combination with topological materials or states of matter with topological properties has been proposed as a building block for the creation of a quantum computer. In addition, the lack of dissipation inherent in superconductivity means they are ideal as the basis of logic for large computing clusters, where heat and energy cost is the main concern. Understanding the fundamental properties of superconductors becomes important when pushing the limits of what they can do.

1.1 Smaller is Different

Nanoscale devices not only let us observe the underlying mechanisms more clearly, but occasionally have intrinsically different properties than the bulk material. Limiting the size of a material can lead to the emergence of phenomena completely dissimilar to the bulk material. As an example, aluminum is normally a Type-I superconductor, which expels all magnetic flux from its interior. However, as aluminum is made thinner, it transitions from type-I to type-II, which allows magnetic field to penetrate the superconductor in a lattice of flux quanta. If this film is then further constrained in both its width and length down to a 1-D limit, the device begins to exhibit properties arising from individual flux quanta (see Chapter 6).

However, it is difficult to create devices that are small enough to show these phenomena, as the size scale required is often at the limits of the manufacturing equipment. Indeed, this nanoscale regime is often on the order of tens of nanometers or less, which is difficult to obtain even with advanced lithographic techniques. This issue is what motivated me to develop a more flexible technique for creating nanodevices described in Chapter 5.

By developing techniques to create devices with extremely reduced dimensions and investigating their transport properties, we can better understand superconductivity in general. Probing such small dimensions will help guide the creation of future superconducting devices and sensors both in the knowledge it provides and the potential new phenomena it could discover.

Chapter 2

Theory

Since a superconductor actively expels a magnetic field up to some critical field H_C, we can express the energy required to condense the superconducting condensate in terms of the critical field. This is because a field in a certain volume contains some energy

$$\frac{H_c^2(T)}{8\pi} = f_n(T) - f_s(T) \tag{2.1}$$

where f_s and f_n are the Helmholtz free energies of the superconducting and normal states respectively. Energy is required to prevent the magnetic field from penetrating the superconductor, so if the applied magnetic field is higher than that the material will lower its free energy by transitioning to the normal state.[3]

2.1 The London equations

In 1935, F. and H. London proposed a series of equations[4] that described the essential properties of superconductivity

$$\mathbf{E} = \frac{\partial}{\partial t}(\Lambda \mathbf{J_s}) \tag{2.2}$$

$$\mathbf{h} = -c\nabla \times (\Lambda \mathbf{J_s}) \tag{2.3}$$

where

$$\Lambda = \frac{4\pi\lambda^2}{c^2} = \frac{m}{n_s e^2} \tag{2.4}$$

is a phenomenological parameter (n_s is the number density of superconducting electrons). The important thing we want to take away from these equations is that by combining Eqn. 2.3 with the Maxwell equation

$$\nabla \times \mathbf{h} = \frac{4\pi \mathbf{J}}{c} \tag{2.5}$$

you get

$$\nabla^2 \mathbf{h} = \frac{\mathbf{h}}{\lambda^2} \tag{2.6}$$

which implies the magnetic field $\mathbf{h}$ is exponentially suppressed in the interior of the superconductor with penetration depth λ, as per the Meissner effect. This theory

described superconductivity's basic properties of the Meissner effect and perfect conductivity, but failed to provide any explanation for the effects of a magnetic field strong enough to destroy the superconductivity and spatial variation in n_s in the superconductor. We also see that if we set as an upper limit the conduction electron number density n, we can solve Eqn. 2.4 for the parameter λ

$$\lambda_L(0) = \left(\frac{mc^2}{4\pi ne^2}\right)^{1/2} \tag{2.7}$$

where T is set to zero, as near the transition n should go to zero and this equation should diverge.

2.2 Ginzburg-Landau theory

In 1950, Ginzburg and Landau developed a phenomenological theory to help fill in the gaps of London theory based on Landau's theory of second order phase transitions.[5] Ginzburg and Landau described a superconductor by a complex wavefunction, $\psi e^{i\phi}$, where $|\psi|^2$ describes the local density of superconducting electrons n_s. In a second order phase transition, the order parameter (the aforementioned complex wavefunction in this case) increases continuously from zero at the critical temperature. By assuming the free energy of the system could be approximated by the first few terms of a Taylor series expansion of the order parameter around the phase transition (as

it would be small), we arrive at this equation for the free energy,

$$f_s = f_n + \alpha|\psi|^2 + \frac{1}{2}\beta|\psi|^4 + \frac{1}{2m^*}\left|\left(\frac{\hbar}{i}\nabla - \frac{e^*}{c}\mathbf{A}\right)\psi\right|^2 + \frac{h^2}{8\pi} \tag{2.8}$$

where α and β are parameters, m^* is the effective mass of the charge carrier, e^* is the effective charge, $\mathbf{A}$ is the vector potential, h is the applied magnetic field, and $\beta > 0$.

If there are no fields or gradients, we have

$$f_s - f_n = \alpha|\psi|^2 + \frac{1}{2}\beta|\psi|^4 \tag{2.9}$$

corresponding to a Taylor expansion where only the first two terms are kept. If one stays close to the phase transition (where $|\psi|^2$ is small), this approximation should remain valid. Finding the minimum, we see that

$$0 = \alpha\psi + \frac{1}{2}\beta|\psi|^2\psi \tag{2.10}$$

$$|\psi|^2 = -\frac{\alpha}{\beta} \tag{2.11}$$

where $|\psi|^2$ in this case refers to the order parameter far away from any fields or surface currents. Plugging this back into Eqn. 2.9, we get that

$$f_s - f_n = \frac{-\alpha^2}{2\beta} = -\frac{H_c^2(T)}{8\pi} \tag{2.12}$$

by recalling the original definition of the free energy difference in Eqn. 2.1.

Since $\alpha(T)$ must change from positive to negative at T_C (to ensure a non-zero solution for $|\psi|^2$), we expand this term around T_C and keep only the first linear term, so that

$$\alpha(T) = \alpha_0\left(\frac{T}{T_C} - 1\right) \tag{2.13}$$

where $\alpha_0 > 0$.

Looking at the remaining term in Eqn. 2.8 and remember that $\psi = |\psi|e^{i\phi}$, we can simplify it to

$$\frac{1}{2m^*}\left[\hbar^2(\nabla|\psi|)^2 + \left(\hbar\nabla\phi - \frac{e^*\mathbf{A}}{c}\right)|\psi|^2\right]^2 \tag{2.14}$$

which in the London gauge ϕ is constant, so this term is just $e^{*2}\mathbf{A}^2|\psi|^2/2m^*c^2$. If we equate this to the kinetic energy density derived from a London superconductor, we get

$$\lambda^2 = \frac{m^*c^2}{4\pi|\psi|^2e^{*2}} \tag{2.15}$$

Noting that $e^* = 2e$ and $m^* = 2m$ from BCS theory,[6] we can evaluate these parameters for $\alpha(T)$, $\beta(T)$, and $|\psi|^2$:

$$|\psi_|^2 = \frac{mc^2}{8\pi e^2\lambda^2} \tag{2.16}$$

$$\alpha(T) = -\frac{2e^2}{mc^2}H_c^2(T)\lambda^2(T) \tag{2.17}$$

$$\beta(T) = -\frac{16\pi e^4}{m^2c^4}H_c^2(T)\lambda^4(T) \tag{2.18}$$

2.3 Coherence Length

If we apply variational methods to the volume integral of Eqn. 2.8, we are lead to the Ginzburg-Landau differential equation

$$0 = \alpha\psi + \beta|\psi|^2\psi + \frac{1}{2m^*}\left(\frac{\hbar}{i}\nabla - \frac{e^*}{c}\mathbf{A}\right)^2\psi \tag{2.19}$$

If we assume no fields are present, we can investigate this equation further by introducing a normalized wavefunction $f = \psi/\psi_\infty$ where $\psi_\infty^2 = -\alpha/\beta > 0$. Eqn. 2.19 then simplifies to:

$$\frac{\hbar^2}{2m^*|\alpha|}\frac{d^2f}{dx^2} + f - f^3 = 0 \tag{2.20}$$

From this we can define a length scale for this system as:

$$\xi^2(T) = \frac{\hbar^2}{2m^*|\alpha(T)|} \tag{2.21}$$

where $\alpha(T)$ depends on temperature in the way derived in 2.13. Linearizing Eqn. 2.20 with $f(x) = 1 + g(x)$ we get

$$g''(x) = \frac{2}{\xi^2}g(x) \tag{2.22}$$

Which have exponential solutions showing that variations from ψ_∞ will decay with length of order $\xi(T)$. This characteristic length is called the superconducting coher-

ence length. If we substitute in the value for $\alpha(T)$ we derived in Eqn. 2.17 into Eqn. 2.21, we get that:

$$\xi(T) = \frac{hc}{4\sqrt{2}\pi e H_c(T)\lambda(T)} = \frac{\Phi_0}{2\sqrt{2}\pi H_c(T)\lambda(T)} \tag{2.23}$$

where

$$\Phi_0 = \frac{hc}{2e} \tag{2.24}$$

is the flux quantum. This quantity will be important in Chapter 6, as that chapter deals with the manipulation of individual flux quanta.

Using BCS theory in the limit of $T \approx T_c$, , we obtain this equation to relate the zero temperature critical field to the to its properties around T_c

$$H_c(T) = 1.74 H_c(0)\left(1 - \frac{T}{T_C}\right) \tag{2.25}$$

If we combine this equation with the critical field as a function of the coherence length for Type-II superconductors

$$H_c = \frac{\Phi_0}{2\pi\xi^2} \tag{2.26}$$

We can extract the coherence length as a function of the slope of H_c vs T close to T_C. Indeed, that is what we do in Chapter 6 using the data in Figure 6.4.

2.4 Vortices

Type-II superconductors differ from type-I in that magnetic flux can penetrate them, but the flux does so in a particular way. If we take the Bohr-Summerfeld quantum condition and quantized the canonical momentum associated with a line of flux, we get

$$\Phi' = \frac{c}{2e} \oint \left(m^* \mathbf{v}_s + \frac{2d\mathbf{A}}{c} \right) \cdot d\mathbf{s} = \frac{c}{2e} \oint p \cdot d\mathbf{s} \tag{2.27}$$

$$\Phi' = \frac{nhc}{2e} = n\Phi_0 \tag{2.28}$$

This can also be deviated from G-L theory by noting that the phase ϕ needs to be single-valued, so the integral

$$\oint \nabla\phi \cdot d\mathbf{s} = 2\pi n \tag{2.29}$$

can be combined with the canonical momentum to be used to derive the same value.

2.4.1 Flux flow

The flux quanta in a superconductor are collective excitations of the underlying cooper pairs and quasiparticles, but we can treat them as excitations in their own right. If we apply enough magnetic field to allow a flux quantum to enter a superconductor and then apply a current perpendicular to that magnetic field, the vortex

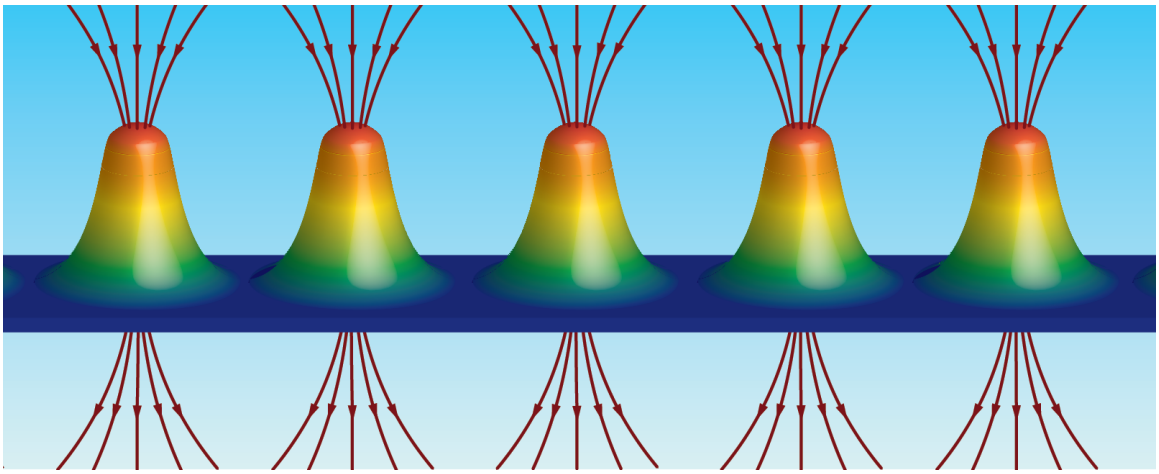

Figure 2.1: Schematic of flux quanta entering a superconductor. The flux enters in tubes penetrating the superconductor and this results in a phase change of 2π around the core of the vortex. This phase change sets up a circulating current around the flux tube, which is why they are also commonly referred to as "vortices."

experiences a Lorentz force

$$\mathbf{F} = \mathbf{J} \times \frac{\mathbf{B}}{c} \tag{2.30}$$

where $\mathbf{J}$ is the current density. B is quantized in units of flux, so the force on our vortex is

$$\mathbf{F} = \mathbf{J} \times \frac{\mathbf{\Phi_0}}{c} \tag{2.31}$$

Ignoring pinning effects, this force will result in the magnetic flux quantum moving through the superconductor transverse to the current. A moving magnetic field induces an electric field

$$\mathbf{E} = \mathbf{B} \times \frac{\mathbf{v}}{c} \tag{2.32}$$

which is parallel to $\mathbf{J}$. An electric field parallel to the current means there will be a

voltage drop, and thus our superconductor will read a non-zero resistance.

If we assume the vortices experience some viscous damping force $-\eta \mathbf{v_f}$, where $\mathbf{v_f}$ is the velocity of the vortex and η is the viscous drag coefficient, we can find the dissipation by simply noting that

$$\mathbf{W} = -\mathbf{F} \cdot \mathbf{v_f} = \eta {\mathbf{v_f}}^2 \tag{2.33}$$

We can also see that the flux flow resistance from the vortices is E/J, so

$$\rho_f = \frac{E}{J} = B\frac{\Phi_0}{\eta c^2} \tag{2.34}$$

If we model a vortex as having some size ξ where the core is normal and currents circulate with velocity $v_s = \hbar/m^* r$ around the core,[7] we can find the microscopic field using the London equation

$$e = \frac{\partial}{\partial t}(\Lambda \mathbf{J}_s) = \frac{\partial}{\partial t}\left(\frac{m^* \mathbf{v_s}}{e^*}\right) \tag{2.35}$$

$$e = -\mathbf{v_f} \cdot \nabla\left(\frac{m^* \mathbf{v_s}}{e^*}\right) = \mathbf{v_f} \cdot \nabla\left(\frac{\hbar}{2e}\frac{\hat{\theta}}{r}\right) \tag{2.36}$$

If we assume v_f is in the x direction, we find a uniform electric field inside the core, given by

$$\mathbf{e}_{core} = \frac{v_f \Phi_0}{2\pi a^2 c}\hat{\mathbf{y}} \tag{2.37}$$

Knowing the normal state conductivity/resistivity of the material, we can see the dissipation **W** is

$$\mathbf{W} = \pi a^2 \sigma_n e_{core}^2 = \frac{v_f^2 \Phi_0^2}{4\pi a^2 c^2 \rho_n} \tag{2.38}$$

where ρ_n is the normal state resistivity.

If we integrate over the fields in the exterior and interior of the vortex surface (denoted by the radius a), this value is doubled. So our overall dissipation is given by

$$\mathbf{W} = \pi a^2 \sigma_n e_{core}^2 = \frac{v_f^2 \Phi_0^2}{2\pi a^2 c^2 \rho_n} \tag{2.39}$$

Combining this with Eqn. 2.33, we can determine the viscous drag coefficient η as

$$\eta = \frac{\Phi_0^2}{2\pi a^2 c^2 \rho_n} \tag{2.40}$$

and using our expression for the flux flow resistance (Eqn. 2.34) and $H_c = \Phi_0/2\pi\xi^2$, we can solve for the flux flow resistance in terms of the magnetic field B, the vortex size a, the coherence length ξ, and H_{c2}

$$\rho_f = \rho_n \frac{2\pi a^2 B}{\Phi_0} = \rho_n \left(\frac{a}{\xi}\right)^2 \frac{B}{H_{c2}} \tag{2.41}$$

If $a = \xi$, the coherence length is equal to the vortex size and there is a continuous transition from the flux flow regime to the normal state resistance as B increases. However, if the vortex size a is different than ξ, we see that there will be a discontinuity

at H_{c2} as the flux flow resistance and normal state resistance will be different below and above the transition. Indeed, we see this discontinuity in data on thin, narrow superconducting wires (see Chapter 7) which in this model implies a vortex size different than that of the coherence length.

Chapter 3

Fabrication

One of the main challenges in the field of nano-electronics is the fabrication of working nano-devices. Before one can study the intricacies of the dynamics and physical processes that occur in various materials, one must manufacture devices best suited to study those materials. Additionally, one of the challenges of experimental condensed matter physics is how to manufacture these devices so that you can actually connect instruments to them and collect meaningful data. Much like the question of whether a tree falling in the woods makes any sound if no one is around to hear it, an interesting nanostructure does not reveal any interesting physics if there is no way to measure it. Thus the challenge of fabrication is central to the study of condensed matter physics.

Much of the interesting physics occurs when you scale a bulk material down to the 1-D and 2-D limit, and thus one of the main challenges a researcher in this field faces

is the best method for manufacturing these devices on such a small size scale. This is not just a purely academic exercise, as reducing the feature size of nano-electronics is one of the main problems faced in the semiconducting processor industry. The smaller you can make a transistor, the more devices you can fit in the same space and make your processor cheaper and more powerful. Thus, understanding the process in which nano-devices are made is a critical process that is in the interest of both industry and academia.

Manufacturing nano-electronics is a difficult process for many reasons. First and foremost, the production of small nano-devices is difficult because of issues of contamination. When manufacturing small devices, even small amounts of impurities can completely ruin or introduce additional effects in your measurement unrelated to what you are trying to study. The latter is much worse than the former, as a non-working sample wastes only the time it took to produce it, while a working-but-faulty sample wastes that time as well as the time spent measuring and analyzing it. Ensuring that the device you are producing is only what you think it is and nothing more is one of the main goals of good manufacturing processes.

Secondly, when reducing the size of nano-electronics you start to run into fundamental issues related to the resolution of your equipment used to produce the devices. As a general rule of thumb, the difficulty and technical capabilities needed to manufacture nano-devices scales inversely with the size of the device. Thus, producing a device with a size scale of 1μm is much easier than producing a device on the scale of

100nm, and producing a device smaller than that is harder still. As devices approach the minimum size scales of what is used to produce these devices, fundamental issues start arising regards the resolution limits of these devices. Much of what I will talk about in this chapter deals with these fundamental problems and workarounds for them.

3.1 Substrate

Small nano-electronic devices are rarely studied in a vacuum, and thus need some sort of substrate. An ideal substrate should be reasonably atomically smooth, non-interacting with the sample, and have good mechanical properties to ensure that the device survives thermal cycling between cryogenic and room temperatures. In this thesis, all the devices were prepared on single crystal silicon wafers which fit all of the criteria above. Silicon is useful in transport measurements both due to its non-interacting oxide layer which isolates the semi-conducting silicon from the sample, as well as for its ability to act as a tunable voltage gate by electrically contacting the silicon underneath the oxide layer.

Before any type of lithographic processing is begun, the substrate needs to mechanically cleaved into a shape appropriate for the process to be used. In this case, a 10cm diameter silicon wafer was cleaved into 3x3cm squares. Each 10cm silicon wafer has a notch in one side that shows the crystal orientation of the wafer. By scoring the

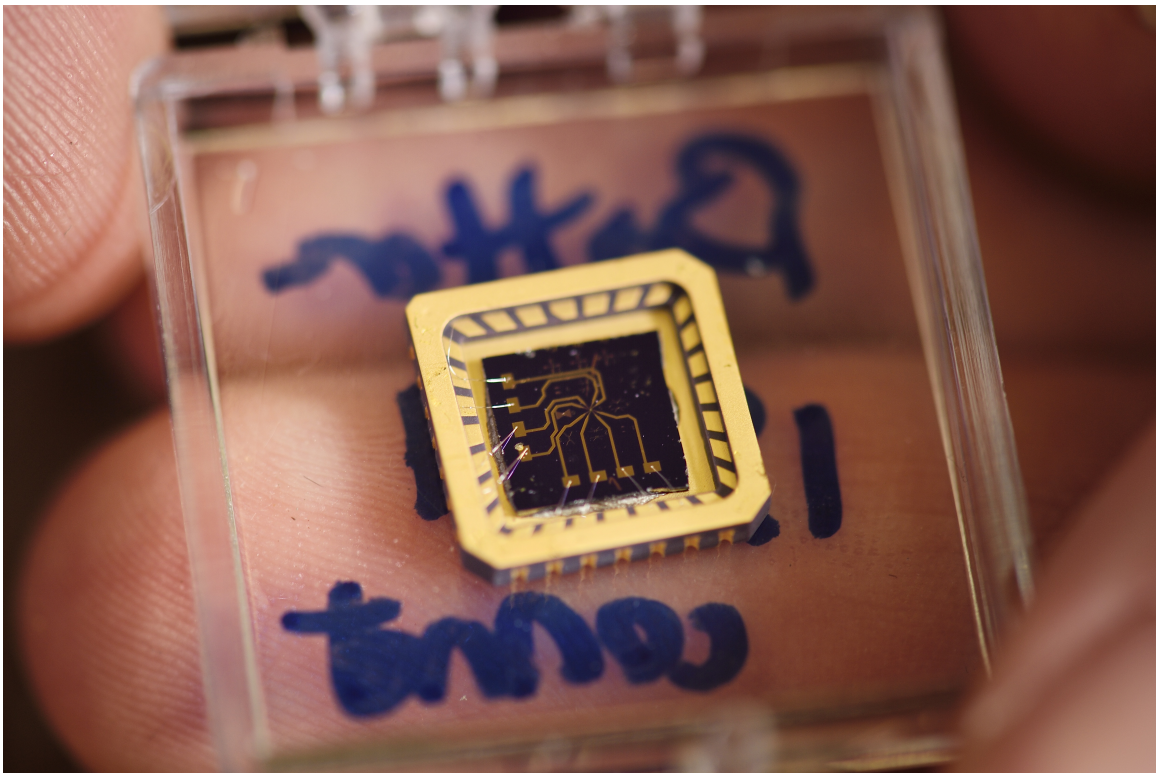

Figure 3.1: Picture of a lithographically produced sample in a chip carrier. The chip carrier is wire bonded to gold leads on the silicon. These gold leads converge at a $100\mu m$ x $100\mu m$ area in the center of the chip, where the actual sample is produced with electron beam lithography.

edge of the wafer parallel or perpendicular to that axis and applying pressure, a clean break across the wafer can be created. By repeating this multiple times along both axes, the round silicon wafer can be broken into smaller, more manageable pieces.

Cleaving the wafer is a dirty process and can leave the substrate covered in microscopic pieces of broken silicon. After the wafer is broken into pieces, they require a cleaning step in order to ensure the surface is clear of all potential contaminants. This is done by placing the silicon pieces in acetone and sonicating them in an ultrasonic cleaner for 5-10 minutes. After the substrate has been sonicated, the pieces are

dipped in isopropanol alcohol (IPA) and then rinsed off in de-ionized water. The last step is important to help clear off the thin layer of organic material that IPA leaves behind when it evaporates. Finally, the wafers are placed either in oxygen plasma or a UV/Ozone cleaner for 5-10 minutes in order to fully remove all organic materials left behind from the cleaning process. The final result is a pristine silicon substrate.

3.2 Optical Lithography

Once the substrate is chosen, you must determine how exactly to create the nano-device you want to make. The choice of how you make your sample is determined by the smallest feature size the design calls for. If the device you are making has features no smaller than 1-2μm or a large area of the substrate needs to be exposed at once, optical lithography can be used. Optical lithography is the creation of tiny plastic "stencils" by selectively exposing a UV-sensitive polymer through a shadow mask. Figure 1 shows the general process for the creation of these stencils. Exposing regions of the polymer to UV light changes their solubility compared to the un-exposed regions. By placing these masks into a developer that is tuned to dissolved only the exposed regions, you can selectively remove those regions and create a stencil for the actual material you want to create your device out of.

In this thesis we used the Shipley 1800 series positive resist S-1813 for all of our optical lithography. In order to get a relatively thin film of the polymer, the resist

was spun on using a Laurell 400B model spinner at 3000 RPM for 45 seconds. This resulted in a polymer thickness of approximately 500nm. The thickness is important, as the resist thickness needs to be much larger than the thickness of the material you are going to evaporate through the resist stencil. If the two are similar in size, the film on top of the resist and the film on the substrate will connect and lift-off will be difficult to achieve. The samples are then baked at 180°C for 90 seconds. This baking process can be extended in order to better remove all of the solvent and moisture from the polymer layer.

After the resist has been spun on, we require one additional step before it can be further processed. The spinning process results in a uniform film everywhere except for the edges of the substrate, where a dune-like ridge forms due to surface tension and the mechanics of the spinning process. In order to have the highest resolution and sharpest features possible, the shadow mask needs to be close to the surface of the resist, so this ridge needs to be removed. This is accomplished by wrapping a small cleanroom wipe soaked in acetone around a set of tweezers and carefully removing the resist all along the edge of the sample. Once the ridge is removed, the sample is ready to be exposed.

3.2.1 UV Mask Aligner

In order to expose the spun resist layer, we need a source of UV light and a way to align the mask to the substrate. This is accomplished with a mask aligner,

which is a piece of equipment that allows one to precisely align a shadow mask to a substrate with a combination of microscopes and high-precision stage alignment tools. The amount of UV exposure needed depends on the resist being used and can be looked up in its datasheet. The UV source also changes over time due to aging of the filament, so before each exposure the intensity of the light source needs to be measured with a UV light meter. Taking the total exposure and dividing it by the light intensity gives the overall exposure time. Once the sample has been exposed, it is then developed and cleaned in the methods described in the beginning of this section. Making sure the substrate is clean by using either oxygen plasma or a UV/Ozone cleaner is important, as one of the main sources of contaminants in nano-lithography comes from the resists used in the optical lithography step.

3.3 Electron Beam Lithography

When features below 1μm are required, standard UV lithography is no longer able to produce the desired design. Producing features with optical lithography below the wavelength of light is an extremely difficult process without specialized equipment. However, we can produce feature sizes much smaller than what we can with optics by instead exposing our sample with a beam of electrons from a scanning electron microscope. By choosing a resist that is sensitive to high energy electrons and sweeping an electron beam across the sample, selectively turning on the beam when it is over

a) b)

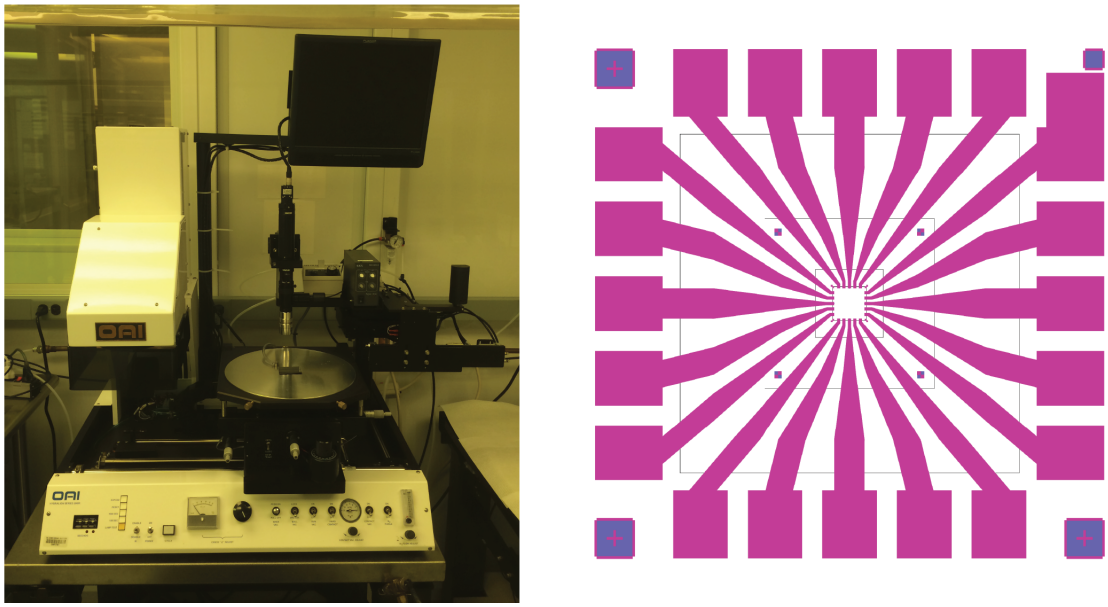

Figure 3.2: **a)** Photo of the UV mask aligner used to make the large optical leads. **b)** Example pattern for the UV mask.

the area we want exposed, we can expose the design we want into the resist layer, and develop it in a similar manner to the optical process.

3.3.1 Mask Design

Compared to the optical lithography process, electron beam lithography (EBL) is much more flexible in that an expensive custom shadow mask does not need to be developed for every different design. Indeed, the wide variety of devices we can produce on this size scale is entirely do to the flexibility of EBL. However, because EBL is a raster process (in that it exposes the design one sweep of the election beam at a time), the time it takes to complete the exposure scales linearly with the amount

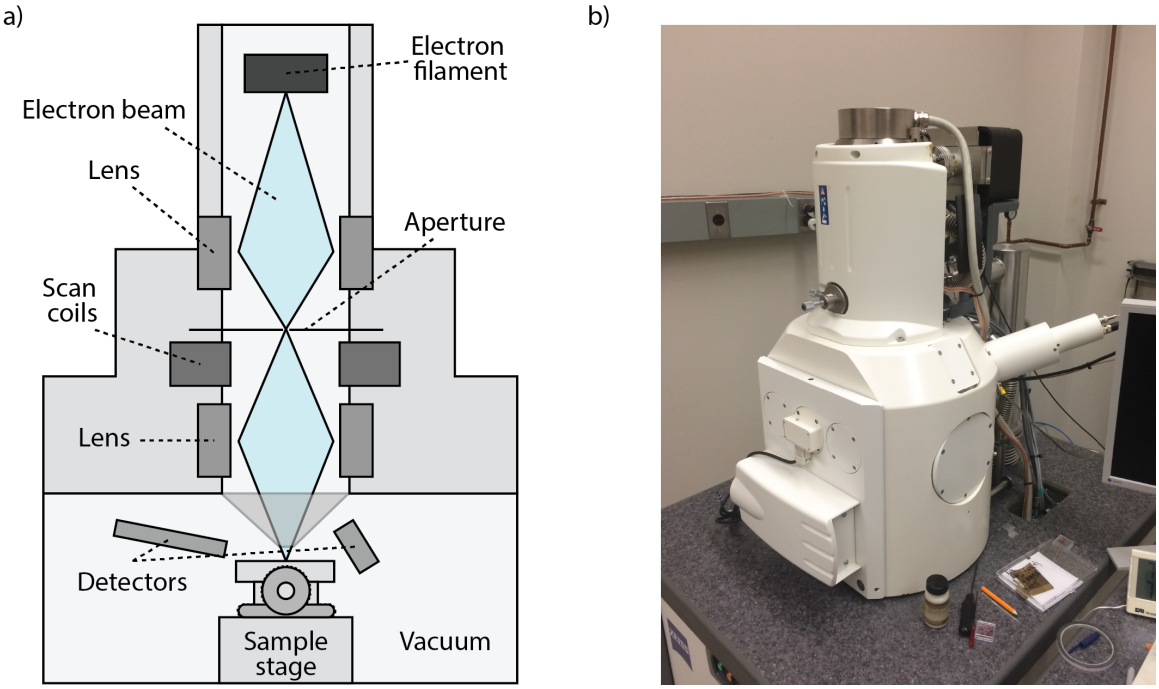

Figure 3.3: **a)** Schematic of an SEM. A filament is heated up in vacuum and electrons are accelerated downwards. These elections are collimated and focused into a thin beam by a series of magnetic lenses, which is scanned across the sample by a set of scan coils. The electrons hit the sample on the moveable stage and are scattered to the detectors. **b)** The Zeiss EVO SEM used for the imaging and creation of all the nano devices in this thesis. The unit is located in the basement of the building to minimize vibrations from the shaking of the building. In addition, the SEM itself rests on an air column to further decouple it from the environment.

of resist to be exposed. Keeping the exposure time under 10-15 minutes produces superior results due to a more consistent beam current over the entire write time as well as less time for the stage to drift due to thermal expansion of the materials. Thus, using EBL for only the small features while producing the large features with UV lithography gets the best of both worlds.

The resist we use for EBL is poly(methyl)methacrylate (PMMA). PMMA is particularly good as a EBL resist due to its high sensitivity to electrons and extremely high resolution. It is a positive resist at low exposures (around sub-5000μ C/cm^2), but becomes a negative resist at exposures higher than that. All of the devices in this thesis were created in the low-exposure regime.

3.3.2 Raith Lithography Software

The actual lithographic process is not controlled by the SEM software; rather, a separate lithography system with a high-speed beam blanker is what controls the writing. This system was developed by Raith Nanofabrication. The SEM itself works by scanning an electron beam across the field of view one line at a time, and the Raith hardware and software controls when the beam is on and off as it scans as to only expose the regions of the resist where the design dictates. The Raith ELPHY software takes CAD DXF files that are either created in the Raith software itself or in other software and is imported.

Most of the designs in this thesis were wholly created in the Raith software,

but some were created in Adobe Illustrator and exported as a DXF file. If a file is created in Illustrator, further processing is sometimes required in the Raith software to adjust the exposure of certain layers. The amount of exposure required is a function of the feature size–larger features require less exposure. This is because writing large features results in increased secondary electron scattering in that region, which effectively increases the exposure level. For large features (above 2x2μm), scaling the exposure down by a factor of 0.6 resulted in full development with a minimum amount of overexposure.

Before the EBL layer can be placed down, it must be first aligned to the underlying UV lithography layer (or vice-vers**a)**. This is accomplished with the use of designed alignment markers in the Raith lithography software, which has an alignment functionality. In practice, aligning features down to an accuracy of approximately 20 nm was possible. This was accomplished by first creating alignment markers with EBL which will be more smaller and thus more precise than aligning to the rough UV markers.

3.4 Development

Once the device is exposed by the SEM, the resist needs to be developed. The development step can be divided into two categories: room temperature development and cold development. For low resolution features (greater than 100nm), room tem-

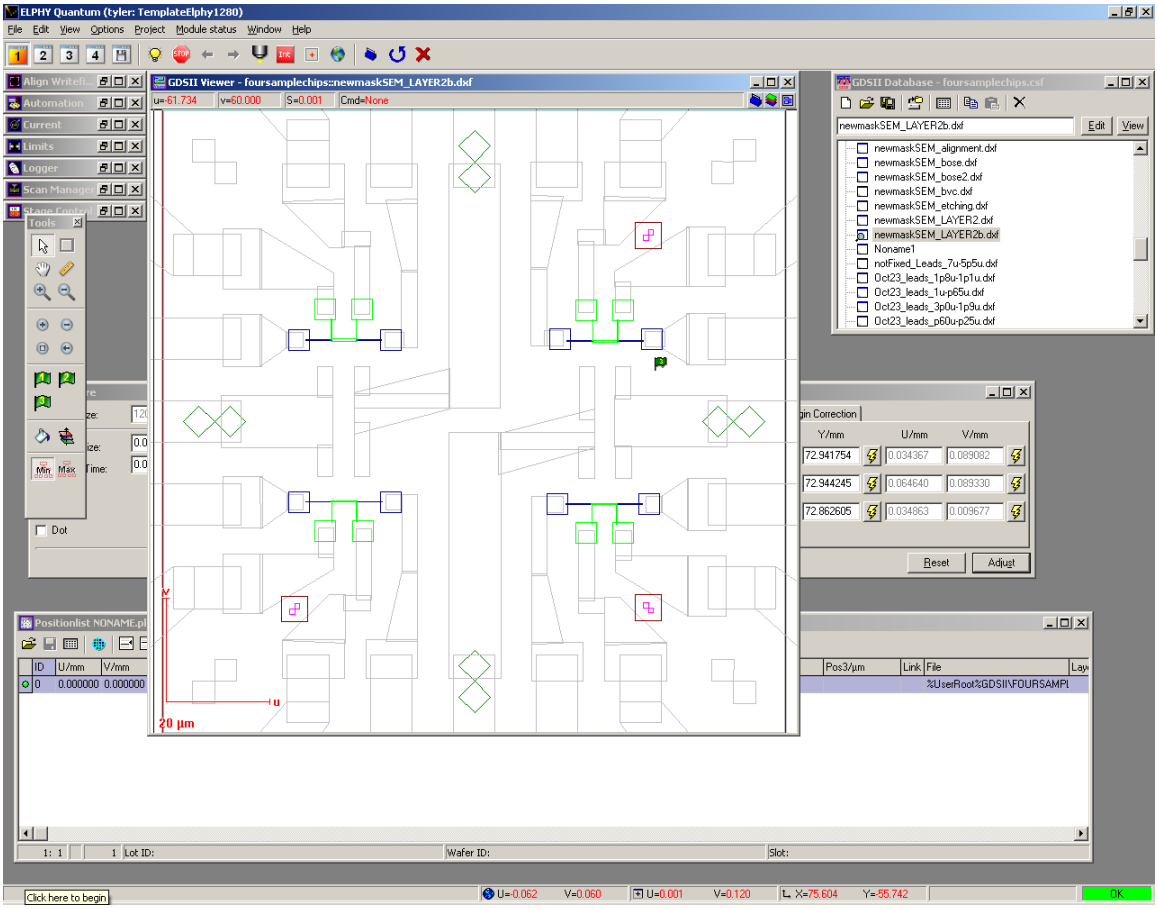

Figure 3.4: Picture of Raith nanolithography software. The different colors on the lithography pattern represent different layers. By calibrating to the alignment markers (shown in purple), these different layers can be precisely aligned to build our device.

perature development has the advantage of requiring a lower dosage during the writing step. This is desired if very large features are being written and drift in the stage or beam current could be particularly disadvantageous to the required design. However, if smaller features or higher resolution features are needed, cold development creates highly superior results with minimal extra processing steps.

3.4.1 Room Temperature Development

The standard development process is as follows: once the sample is developed, it is placed in a developer solution bath. There are two solutions that we use that develop PMMA: an IPA:MIBK 3:1 mixture, and a 7:3 IPA:H20 mixture.[8,9] The former is the standard developer used in most PMMA processes, but is disadvantageous in that it has a tendency to swell the PMMA layer,[10] which causes non-uniformity in extremely small features. The latter is useful in both its simplicity and low-cost, as well as avoiding the swelling at small sizes.

3.4.2 Cold Development

One of the main issues with the development process and EBL in particular is the issue of partially exposed regions of resist. The mechanism that the PMMA becomes "exposed" can be explained by the molecular structure of the PMMA polymer. PMMA consists of a long chain of molecules that can be cut by the electron beam.

When enough of these chains are cut in a certain area, that area's solubility increases in the developer and thus is removed when placed in solution. However, when the electron beam hits the resist, more than just the designed area is exposed. The high energy electrons travel into the substrate and some of them bounce back and hit the resist. In addition, some of the electrons bounce through the material multiple times before hitting the resist. Both the direct backscattering and the secondary electron backscattering result in a much wider area exposed than what was designed. With an accelerating voltage of 30kV in our SEM, feature sizes smaller than 100nm are difficult to produce due to this effect.

Cold development ameliorates much of this issue. The solubility of a solution is a function of its temperature.[11] The regions that are only partially exposed have a different solubility than the regions directly exposed (due to the decreased number of polymer cuts), so by reducing the solubility below that threshold but still above the region where the resist was fully exposed only the designed regions can be targeted. In practice, this increases the resolution of our lithography from 100nm to a smallest feature size of 20nm. This problem is what motivated much of my work on alternative methods for the creation of small nano-devices. More information can be found in Chapter 5.

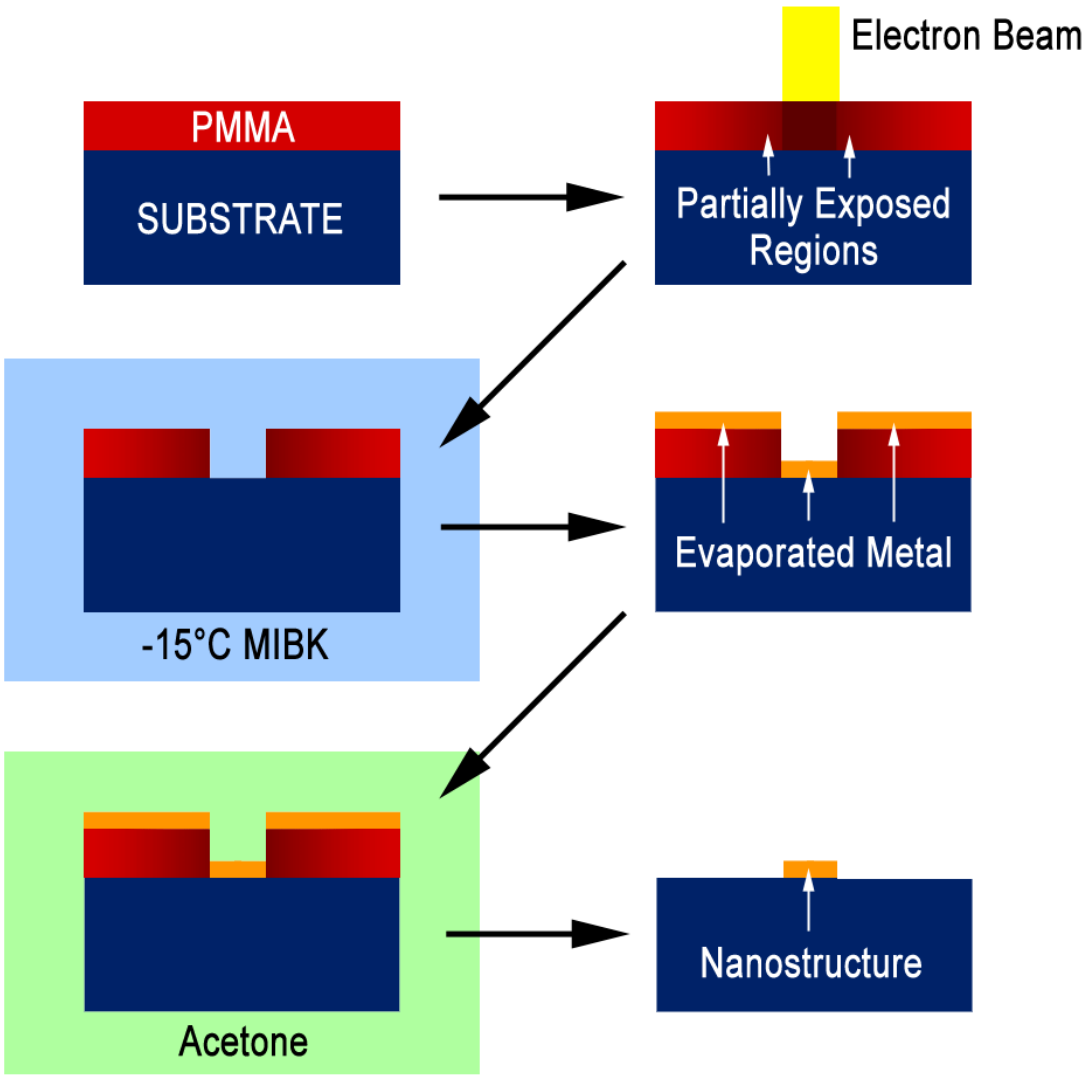

Figure 3.5: The cold development process. We first start with our bare substrate and spin a layer of resist on (in this case, PMMA). We then expose it with to an electron beam in the nano device's designed pattern. Adjacent to the designed exposed regions are regions that become partially exposed due to the scattering of electrons in the substrate. When placed in a cold developer (in this case, -15°C MIBK, but also 0°C 7:3 IPA:H20), these partially exposed regions freeze out and only the fully exposed regions are dissolved. This ameliorates process enables the creation of much smaller and higher resolution features.

3.5 Deposition

Once the lithography steps are done, the material that the device is made of needs to be laid down through the resist. There are many methods that are able to do this, each with their own advantages and disadvantages. Primarily there are three distinct methods: Thermal evaporation, electron beam evaporation, and sputtering. Thermal evaporation is the simplest: a metal is heated up in a crucible with a large current providing the heating power. When the metal is past its melting point in the vacuum, the metal vaporizes and condenses onto the much cooler substrate. Electron beam evaporation is the same process, but with an electron beam doing the heating instead of the crucible. This allows cleaner evaporations due to the more targeted nature of what is being heated up, but also bars certain magnetic metals from being used due to interactions with the electron beam. Sputter deposition involves hitting a metal with highly energetic particles which cause the metal ions to eject from the surface. This process is useful for creating thin films of materials with very high melting points (which would make them inaccessible to thermal evaporation), but disadvantageous in that achieving lift-off for sputtered films is difficult due to the fact that it evenly coats the entire surface of the substrate. I will focus on thermal evaporation, as all of the devices in this thesis were made with this process.

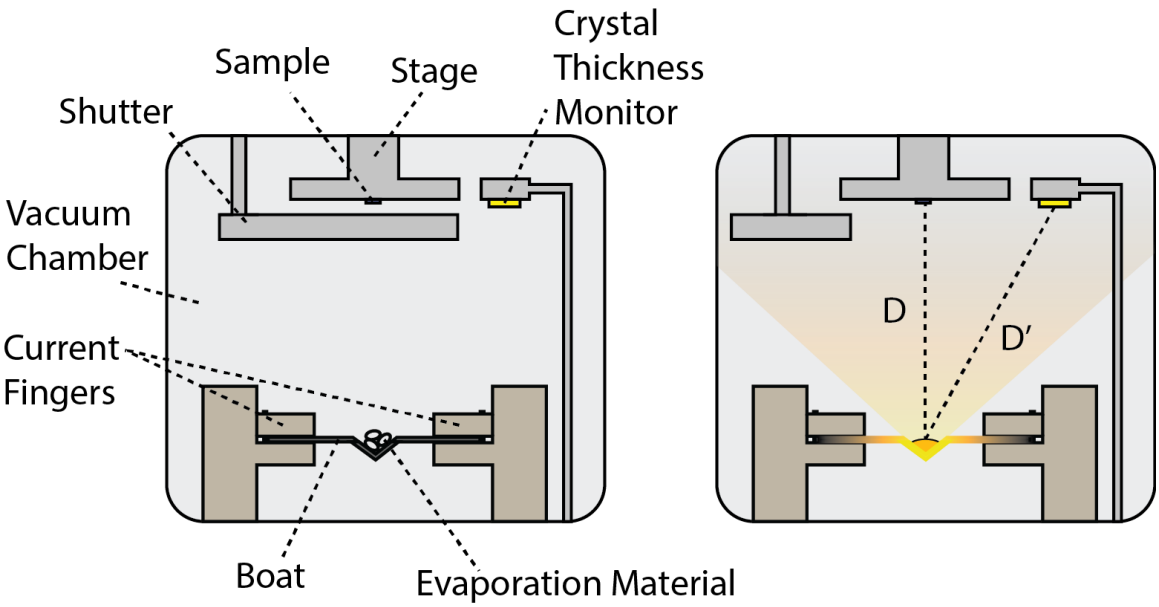

Figure 3.6: Schematic of a thermal evaporator. The sample is secured to the stage with carbon tape and the chamber is pumped down. When a suitable vacuum is reached, current is applied through the current fingers to the crucible/boat holding the material to be evaporated. This crucible heats up until the material reaches its melting point, after which it starts to evaporate. This deposition is line-of-sight from the material, which means that until the shutter is removed nothing is deposited on the sample. The crystal monitor measures the thickness and the rate of the material, corrected by a geometrical factor arising from the different distances D and D' (called the tooling factor). When the desired thickness is reached, the shutter is closed and the current turned off.

3.5.1 Thermal Evaporation

A thermal evaporator is a fairly simple device. The basic principle of a thermal evaporator is described as follows: a material is heated up by applying a large current to a crucible containing highly pure ingots of the desired material. Once the temperature in vacuum reaches the materials melting point, the material begins to evaporate. Up until this point, the substrate has been shielded from the evaporative material by a movable shutter in the vacuum chamber. Once the rate of film deposition reaches the desired amount, the shutter is opened and the film begins to coat the sample.

A vibrating quartz crystal sensor is installed that monitors the thickness of the film as it evaporates. A quartz crystal has a set vibrational frequency that changes as metal is added to it (much like adding weight to the end of a spring). By inputing parameters of the material to be evaporated related to its mass and the acoustic properties of the material (called the z-factor), this change in frequency can be directly correlated with a change in thickness. After the frequency moves too far from its initial value, the crystal is replaced as its thickness tracking ability is reduced.

The thermal coupling of the sample to a cold surface is important in this process. An evaporated film's properties are related to the temperature at which it forms, and if the device is thermally isolated from the metal stage (as an example, by being on a glass slide), the heat will have no where to dissipate. Thus, evaporating films on a glass slide will produce films with different qualities than films evaporated on metal coupled to the chamber. This effect was seen in both gold and aluminum films, in

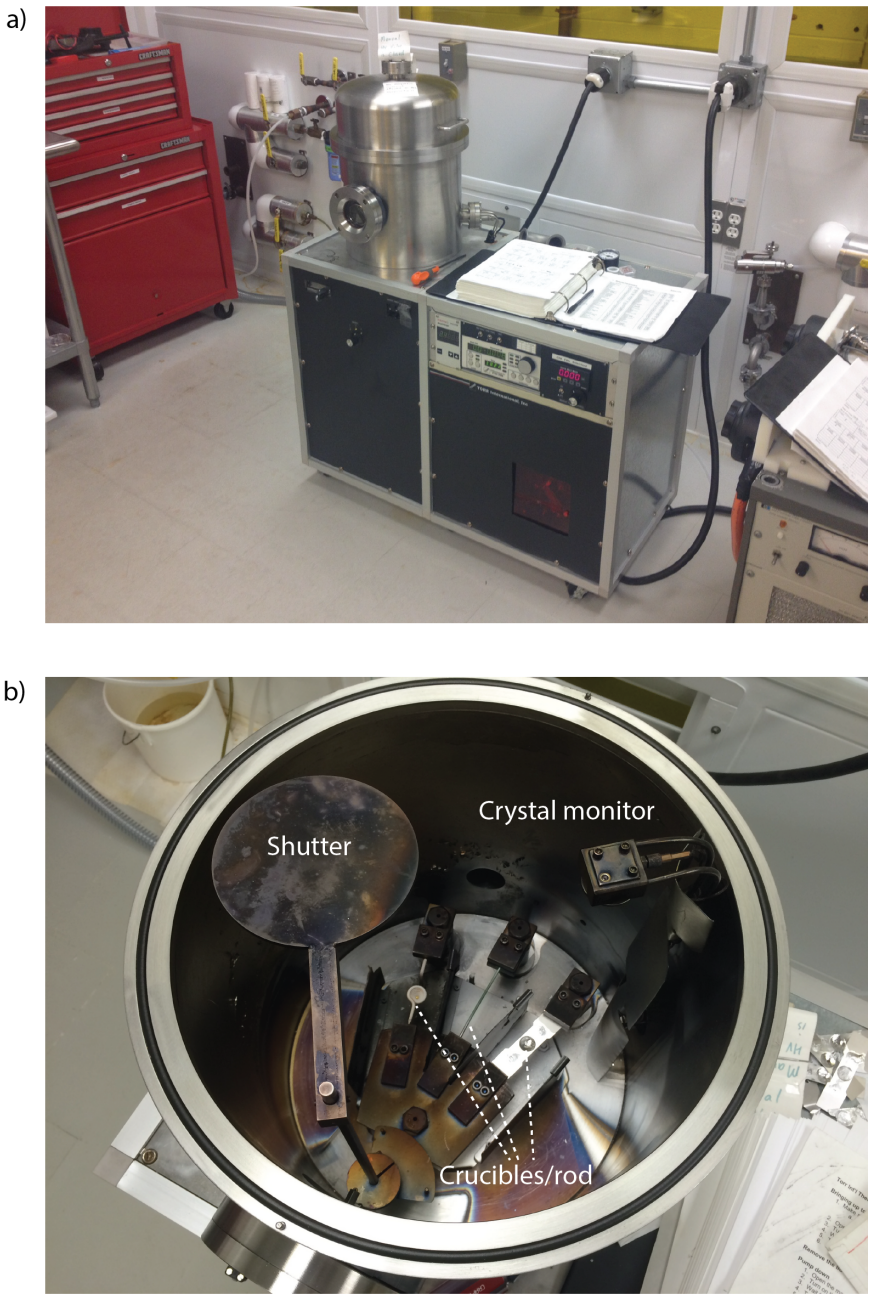

Figure 3.7: Picture of evaporator, inside and out

which a change of thermal coupling from a glass slide to directly connected to the metal stage resulted in decreased the films granularity. This effect can also be seen in changing the rate of evaporation. By evaporating with a high rate and only for a short period of time, less granular films will be produced because the substrate will not have time to equilibrate with the source. Additionally, long evaporations can cause the underlying resist to deteriorate due to this heating effect, so quicker evaporations are desirable in all cases.

In a high vacuum environment, the evaporated metal travels ballistically from the source, so only parts of the substrate with a direct line-of-sight are coated. This aspect of thermal evaporation must be taken into consideration when depositing metal, as this "shadowing" effect from either the resist or other features on the surface can cause gaps in the film that prevent electrical contact. However, this property of shadow evaporation can also be used to produce devices where a small gap between films is desired.

The thermal evaporator we use is made by Torr International. In order to pump the chamber down, two vacuum pumps are used. The first rough pump takes the chamber down from atmospheric pressure to 2×10^{-2} Torr in approximately 5 minutes. If left on, this pump would bring the chamber pressure down another order of magnitude, but at such low pressures oil back streams into the chamber which would contaminate everything inside. So at this point, a turbo pump is turned on that lowers the chamber pressure down to approximately 1.7×10^{-7} Torr. At this point, the

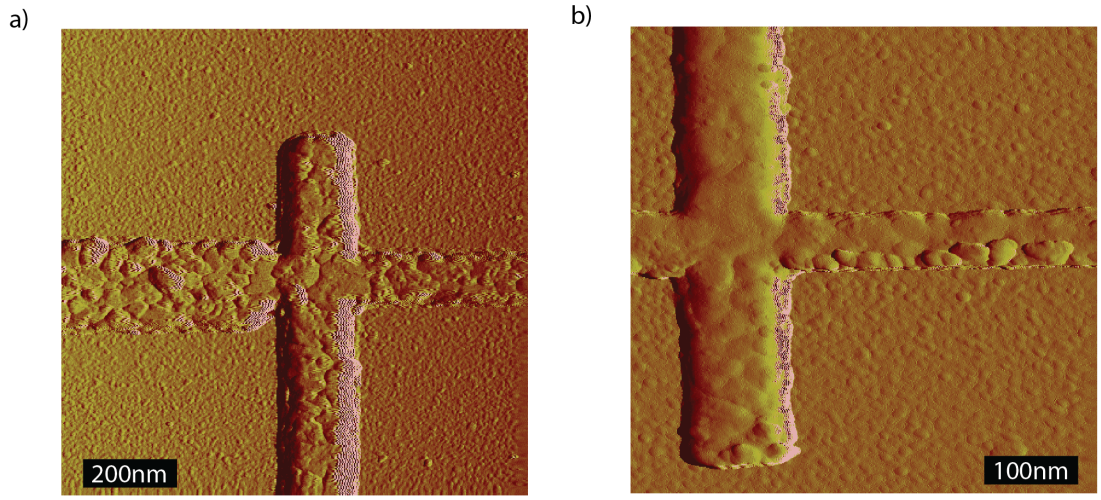

Figure 3.8: **a)** Aluminum film evaporated starting in a chamber with an initial vacuum of 1.7×10^{-7} Torr. **b)** Aluminum film evaporated after chamber pumped down to 3×10^{-8} Torr by evaporating a 1μm titanium film in the chamber. The titanium is highly reactive and absorbs the water vapor in the chamber, which the turbo pump is unable to remove at this pressure. Aluminum is highly reactive with water vapor, so this greatly improves the film quality.

pump cannot lower the chamber pressure any further. This limit is due to the turbo pump's inability to pump out water vapor, which has the largest partial pressure at this vacuum level. This water vapor is undesirable when evaporating certain reactive metals (such as aluminum), as it causes changes in the granularity and film structure (see Figure 3.8). This problem can be ameliorated with a titanium getter evaporation step.

3.5.2 Titanium Getter Pumping

In order to remove the residual water vapor from the chamber and further pump it down, we can add a titanium getter film once the steady state pressure is reached. Titanium is highly reactive and absorbs water vapor, and thus coating the chamber effectively pumps the gas left inside by absorbing it into the fresh titanium film. By preceding our evaporation step by 3-12 hours by a titanium evaporation step, the pressure in the chamber can be lowered an order of magnitude. Using this technique, pressures as low as 2×10^{-8} Torr were reached.

3.5.3 Film Lift-off

Once the material has been deposited, the resist "stencil" needs to be removed. This is accomplished by placing the sample in acetone and dissolving the underlying PMMA. This removes the film on top of the PMMA, but also leaves behind some undesirable features on the remaining film. During the evaporation, metal can build up on the sides of the walls inside of the pattern. These features will often remain after lifting off in acetone, as they are not directly over any PMMA. In order to remove these features, the lift-off process is done in an ultrasonic sonicator. This has the added benefit of speeding up the lift-off process by an order of magnitude. After the film has lifted off, it is cleaned in IPA and DI water and checked in an optical microscope to ensure lift-off was complete.

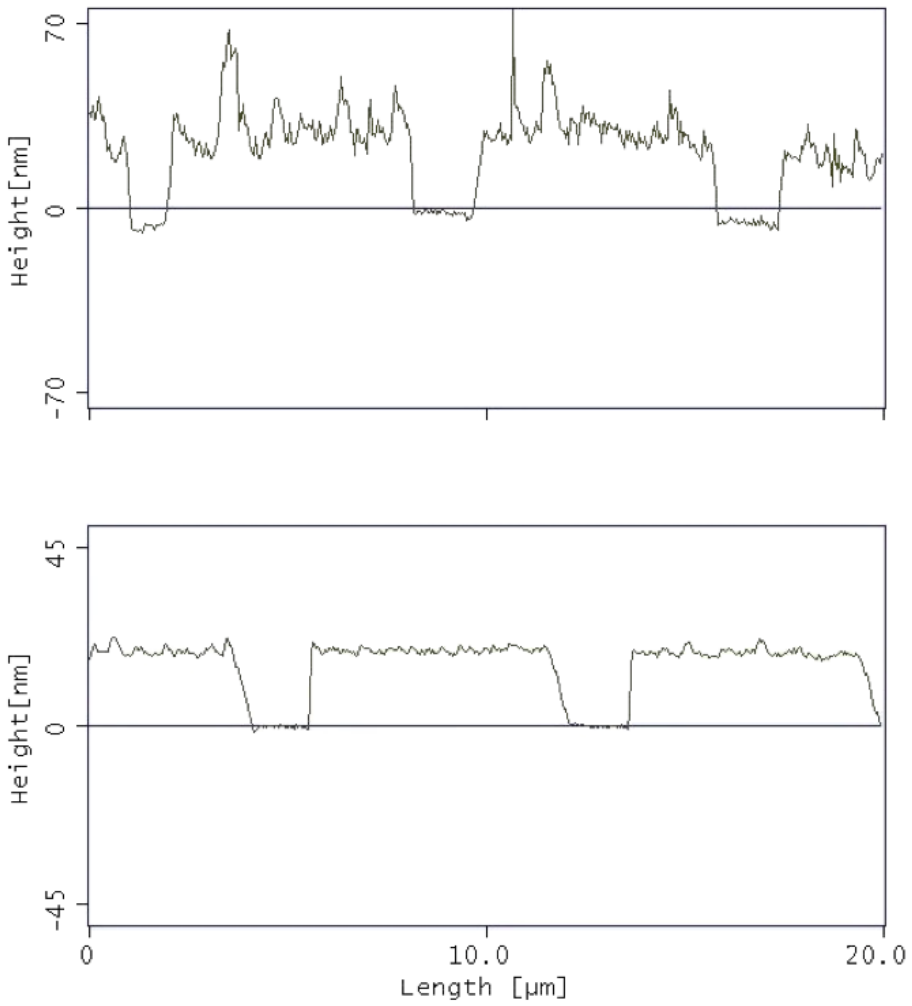

Figure 3.9: AFM cross-section of two wires made with and without sonication during lift-off. The film becomes much more uniform with sonication and unwanted sidewall features are highly diminished. An additional advantage is lift-off in a sonicator takes 15-20 minutes as compared to several hours just in acetone.

3.6 Wirebonding

After the sample has been made and is ready to be measured, it is placed in a Spectrum Semiconducting LCC02834 chip carrier. In order to secure the substrate to the chip carrier, a small amount of silver paint is applied to the chip carrier and the sample is placed on it. The sample is then heated underneath a heat lamp at 100°C for 15 minutes. The silver paint both mechanically and thermally links the substrate to the chip carrier. After the paint is dry, the sample is transferred to a manual wire bonder, and bonded with 25μm radius aluminum wire. The bond placement is important to help ensure contact to the underlying material, as the bonding process often destroys a certain amount of the lead (see Figure 3.10). If the bond is not entirely on the lead, this decreases the probability of a connection.

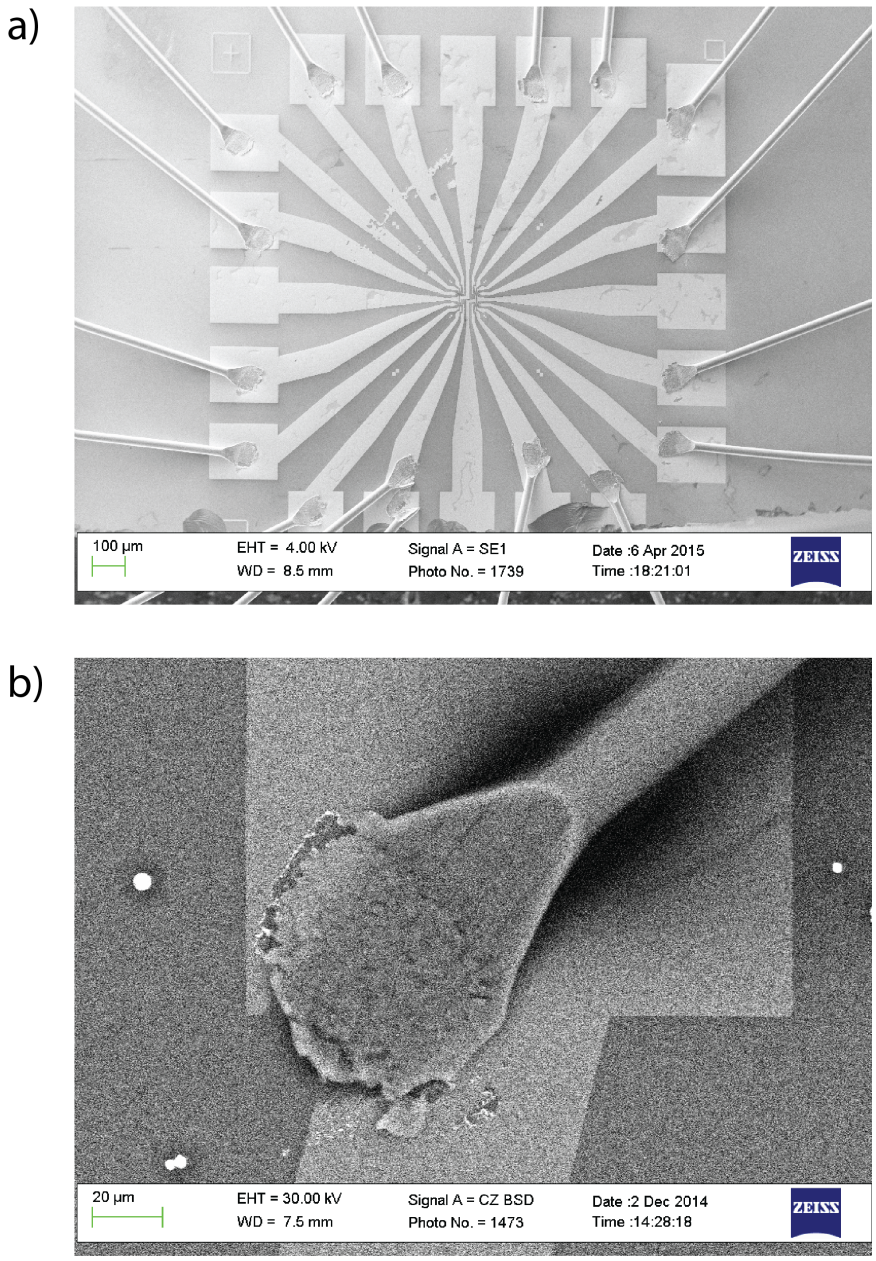

Figure 3.10: **a)** SEM image of a working sample. The wire bonds connect the chip carrier to the sample via the optical leads. **b)** The bond placement on the optical leads is important. The bonding process is relatively violent and can destroy some of the underlying lead (seen here on the left-side of the lead). Placing a bond near the edge of the leads decreases the chance of a successful connection, and thus a bond should be as centered as possible.

Chapter 4

Sample Characterization and Measurement

4.1 Introduction

The characterization and measurement of materials and devices is the main challenge of an experimental physicist. As devices get smaller and the desired physics subtler, an increasing amount of care must be put into the design of the experiment in order to isolate the desired effects. If one performs a measurement and discovers a new and interesting physical phenomena, the burden of proof rests on the experimentalist to prove that the effect is not just a byproduct of the experimental design, but rather something intrinsic to the device being studied. Thus, an experimentalist must understand their equipment inside and out in order to make any reasonable claim to

the discovery of new and interesting physics.

4.2 Sample Characterization

The first step in understanding a material or device is simply to know what it looks like. Characterizing the appearance and dimensions of the device is particularly important when pushing the resolution limits of the lithography process, as variations in the width on the order of tens of nanometers become important when the device is the same order of magnitude. This is accomplished in a number of ways depending on the size of the device and the features of interest.

4.2.1 Optical Microscopy

The first step to characterizing a nano-device is to look at it under an optical microscope. The rough quality of the deposited film can often be seen as variations in the surface texture of the device. High quality films will look uniform under an optical microscope while poor films can have a rough appearance. In addition, this is the point where any impurities (such as residual PMMA, metal and silicon flakes, or dust from the environment) can be seen and the device further cleaned if necessary.

Optical microscopes are limited by the wavelength of light, so extremely small devices cannot be characterized well. However, there are some techniques that can extract some rough information about the size of metal nanowires without having to

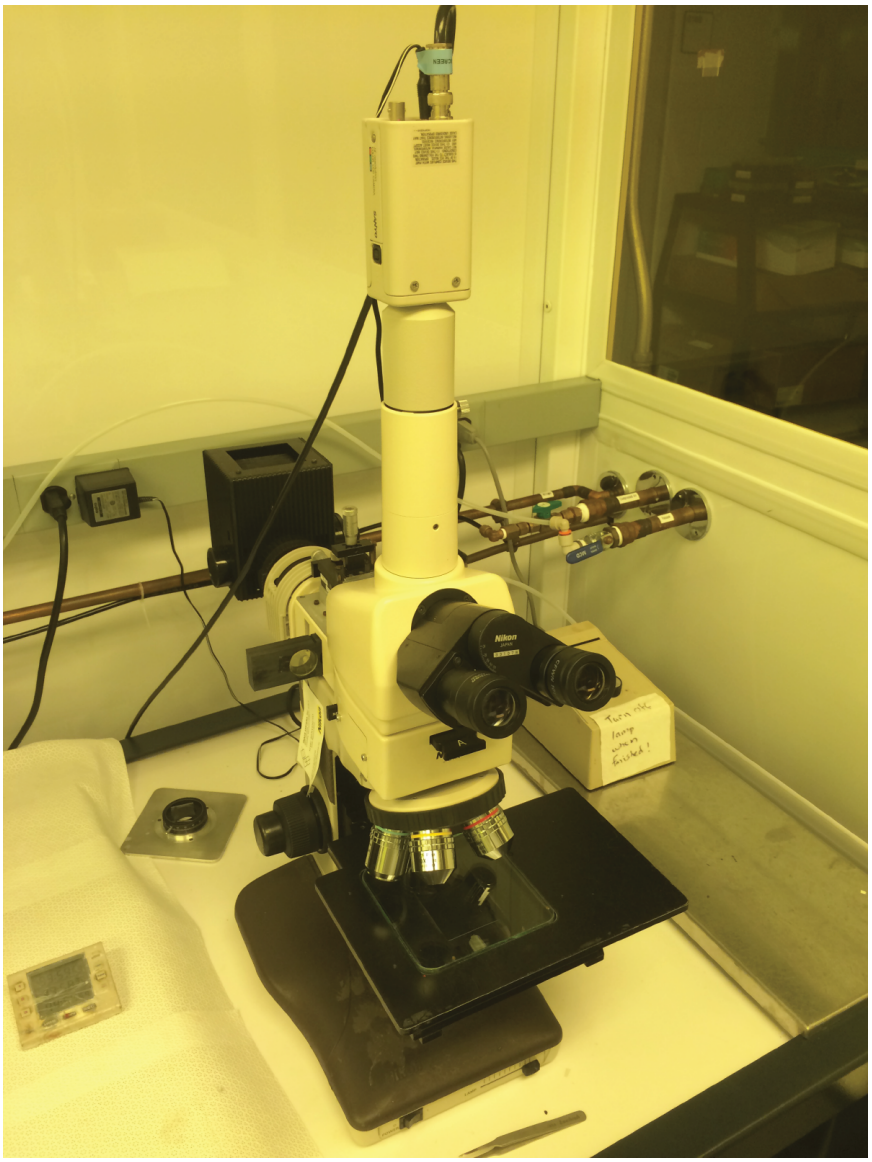

Figure 4.1: Nikon optical microscope used in characterizing samples. The magnification ranges from 50x to 1000x.

use other more complex characterization methods. When light is reflected off of a narrow metal nanowire below the wavelength of optical light, it becomes polarized (due to light polarized perpendicular to the wire not being reflected as well as light polarized parallel to it). This polarization is a function of the wavelength, so higher frequencies (and thus shorter wavelengths) are reflected more readily than lower frequencies. If you put a polarizing filter between the viewfinder and the main lens, the color of a wire will be bluer the thinner the wire is until the wire is thin enough that the blue light is also attenuated (see Figure 4.2.b). This can be used to get a general idea of the size of the wires (before further characterization).

Another trick is to use the source of light to your advantage. Particularly if you can direct the light's direction, you can create long shadows that will highlight features that might be too small to see otherwise. In our set-up, we had a UV filter on the stage light that if pulled out halfway redirected some of the light horizontally. This creates shadows that would emphasize features (such as breaks in the wire) that would not be as apparent otherwise (see Figure 4.2.d).

4.2.2 Atomic Force Microscopy

Below the wavelength of light we need to resort to more complex methods to characterize our samples. Atomic force microscopy is a useful technique to study the shape and especially the thickness of films. An atomic force microscope's (AFM) operation can be thought of as a small tuning fork (called a cantilever) with a sharp

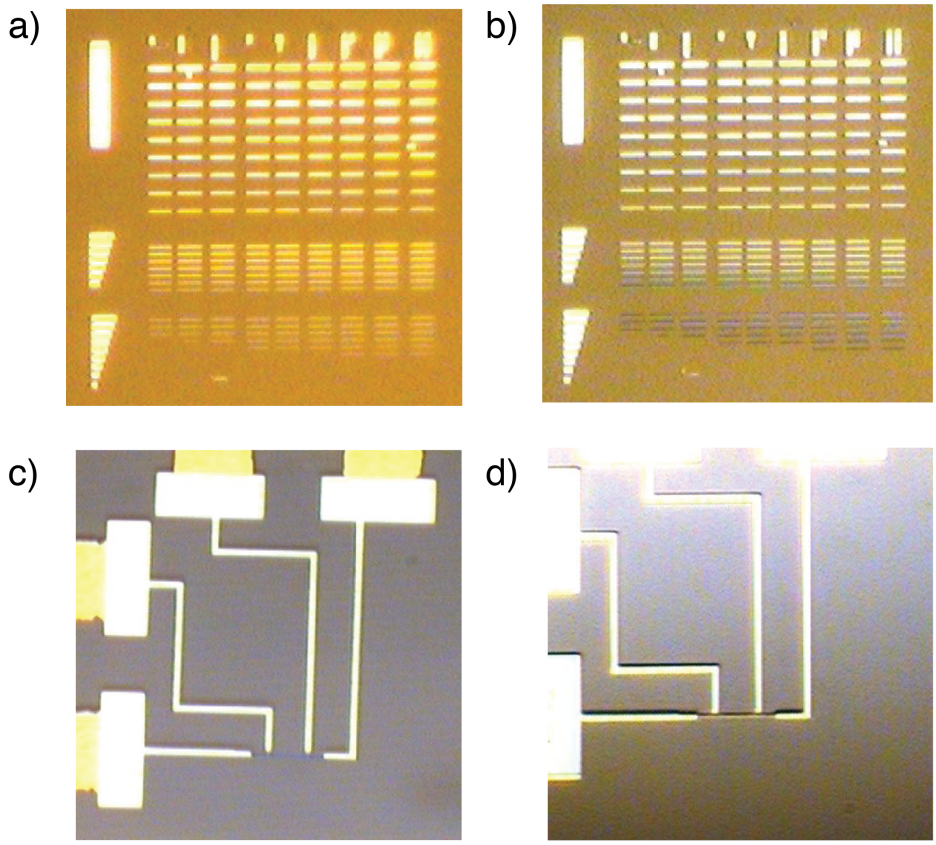

Figure 4.2: Two techniques to assist in characterizing small nanoscale structures using optical microscopy. Below the wavelength of light, it becomes increasingly difficult to use optical microscopy to characterize samples. However, there are some techniques that can use the nature and direction of light in order to get more information on the nanowires without resorting to more complicated characterization methods. Parts a) and b) show a series of wires with the widths decreasing lower on the image. The difference between the two is a polarizing filter oriented perpendicularly to the wire has been added between the eyepiece and the sample. The thinner wires partially polarize the light which make the reflectance a function of frequency, thus leading to the color change. For wires small enough that they are difficult to see even with this method (in part c and d), changing from a stage light to a directional light can create a shadow on small features and thus make them more visible.

probe sticking out of the bottom of one end (see Figure 4.3). Through electromechanical means the cantilever is vibrated at a precise characteristic frequency. As the probe is brought closer to the surface of the sample, it feels a force due to the Van der Waals interaction with the surface. This force changes the oscillation frequency and is a function of the proximity of the tip to the surface, so by moving this tip across the surface and studying how the frequency changes, you get information about the height of the features. This frequency mapping is only one method to extract information from an AFM–anything that exerts a force on the probe tip can be mapped out as well. Thus, changing the probe and mapping out a change potential or using a magnetic tip to map out the magnetic properties of a sample is possible.

Atomic force microscopy's limits come into play when dealing with features with widths below the size of the tip. The image produced is not the true surface topology, but rather the surface features convolved with the shape of the tip. For features with widths much greater than the size of the tip this has no significant effect. Features with widths the same order of magnitude as the tip are distorted significantly. Sharper tips can mitigate this somewhat, but in general width measurements are not entirely accurate on an AFM.

4.2.3 Scanning Electron Microscopy

The problem with optical microscopy is resolving features below the wavelength of light, so one way to get around that is to probe the material with something that has a

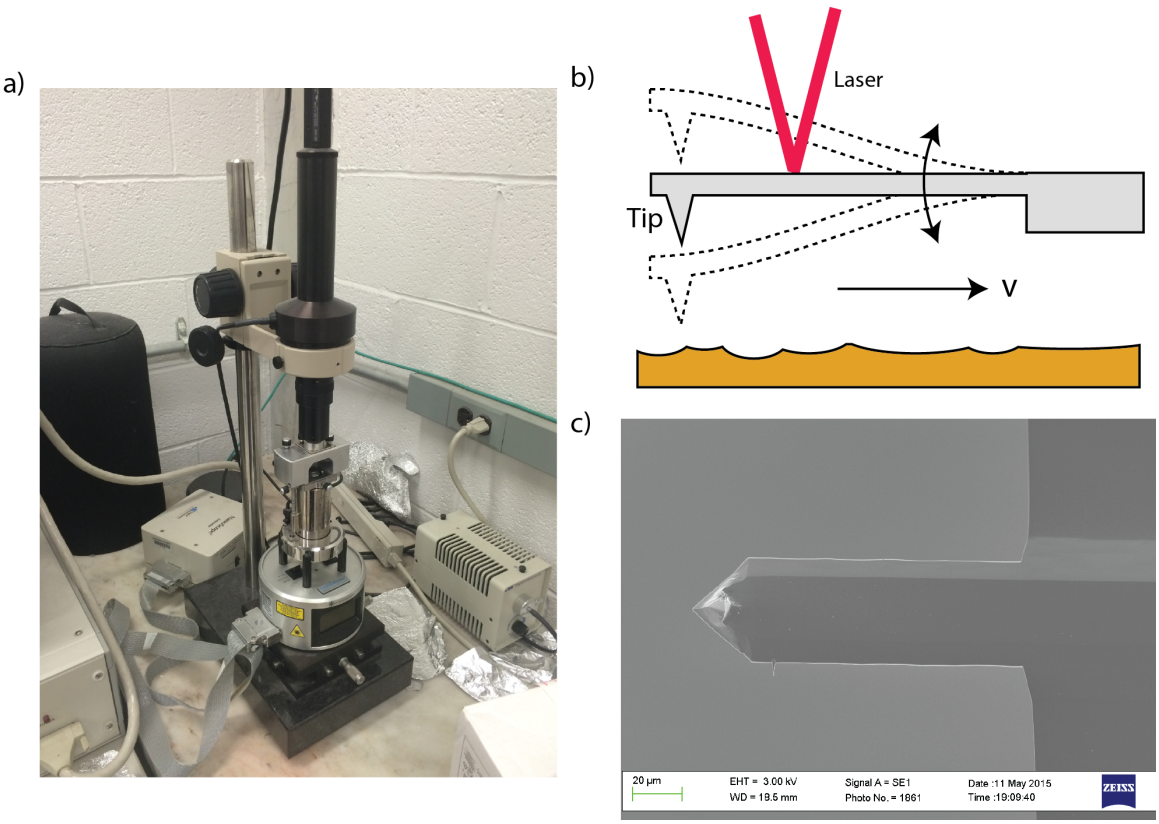

Figure 4.3: **a)** Picture of the atomic force microscope (AFM) used. **b)** Schematic of the functionality of an AFM. The cantilever is electromechanical vibrated at a specific set frequency. As the cantilever and tip is moved across the substrate, the sharp tip point interacts with the surface and changes the frequency of oscillation (measured by a laser reflected off the cantilever). This change in frequency is associated with a change in height of the material being studied. **c)** SEM image of an AFM cantilever. The tip is facing upwards towards the end of the cantilever.

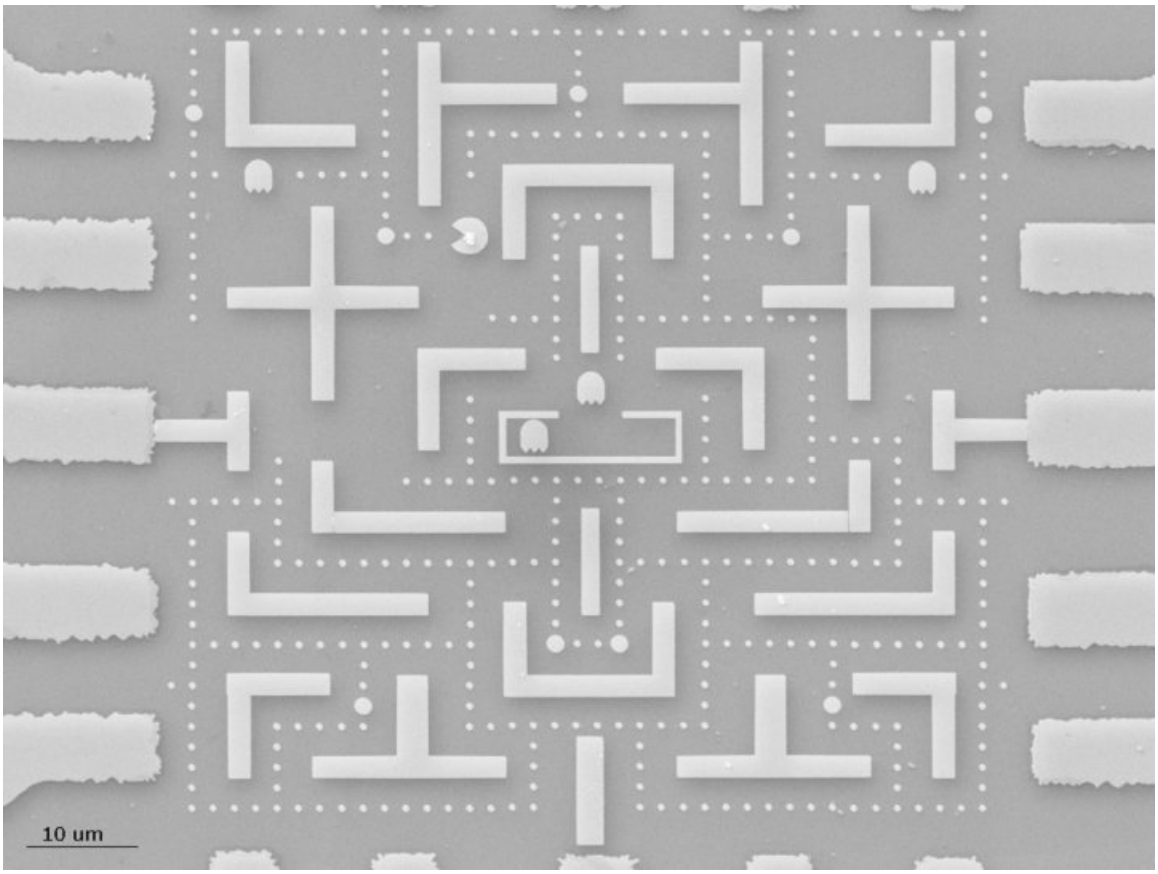

Figure 4.4: A e-beam lithography pattern imaged with an SEM.

much smaller wavelength. An electron's Compton wavelength makes them effectively point particles for probing atomic scale materials, so by using them instead of light we have a much smaller inherent limit. A scanning electron microscope (SEM) works by creating a thin, collimated beam of electrons from a hot filament and accelerating them into the surface of the sample. When they hit the surface, they scatter and are picked up by different detectors. By mapping out the number of electrons hitting the detectors as the beam is swept across the surface, the features of the surface can be mapped out.

Producing a good image with an SEM is an exercise in careful focusing. Much like light can be focused by lenses, electrons are focused and collimated by magnetic fields. To achieve a good image, there must be both enough enough electrons hitting the sample as well as have a well focused beam. The first is accomplished by careful aligning of the electrons coming off the filament to go straight downwards through the accelerating voltage. The second is trickier, as the the beam both needs to be focused as well as corrected for any astigmatisms. A robust technique for adjusting both the focus and astigmatism is to visually adjust the two until it looks focused, and then slightly un-focus the image. Then adjust the focus in the opposite direction until the image is equally unfocused. By splitting the difference between the two, you can be more confident you have the best focus possible.

SEM imaging is particularly useful when the sample you are studying is metallic. For non-metallic features charge has a tendency to build up on the surface, which distorts the beam. Thus, if the goal is simply to visually characterize an insulating device, it helps to coat it with the thin layer of conducting material.

An SEM can be used to map out features on the order of nanometers. The main limiting feature is the beam size, which for our system is on the order of 10nm wide. Features smaller than this need a different characterization technique (such as transmission electron microscopy) to study them. In addition, the vacuum the beam works in is not entirely clean: the solvent used in the lithographic process will often outgas or small amounts of pump oil will be present. When the beam hits this

organic material, it can adhere it to the substrate surface. This process, albeit slow, can result in a build-up of carbon "junk" on the surface substrate (see figure). This carbon film can interfere with connections and cause other negative effects with the device. Thus, the beam should not be placed over one place for too long if a clean device is desired.

Achieving a quality image in an SEM is a different process depending on the dimensions and material of the device. For thick films or devices made of a dense metal that reflects electrons well (such as gold), using a high accelerating voltage (30kV) produces the best image. However, for thin films made of a less dense metal (such as aluminum), most of the electrons will travel right through the device and the image will be faint to nonexistent. Quality images of these thin films require lowering the accelerating voltage to 3-5kV. At this acceleration, the electrons penetrate less deeply into the substrate and thus surface features (such as our films) are more visible.

4.2.3.1 Checking connectivity in the SEM

Lowering the accelerating voltage can also be used to check the connectivity of the device. The lower accelerating voltage charges the surface of what is being imaged. If there are large conductive leads attached to the sample and they are connected, they will dissipate this charge and the device will appear darker. However, if a portion of the device is not connected, the charge will not dissipate and this will be visible. This method of checking he connectivity is much less prone to destroying the sample

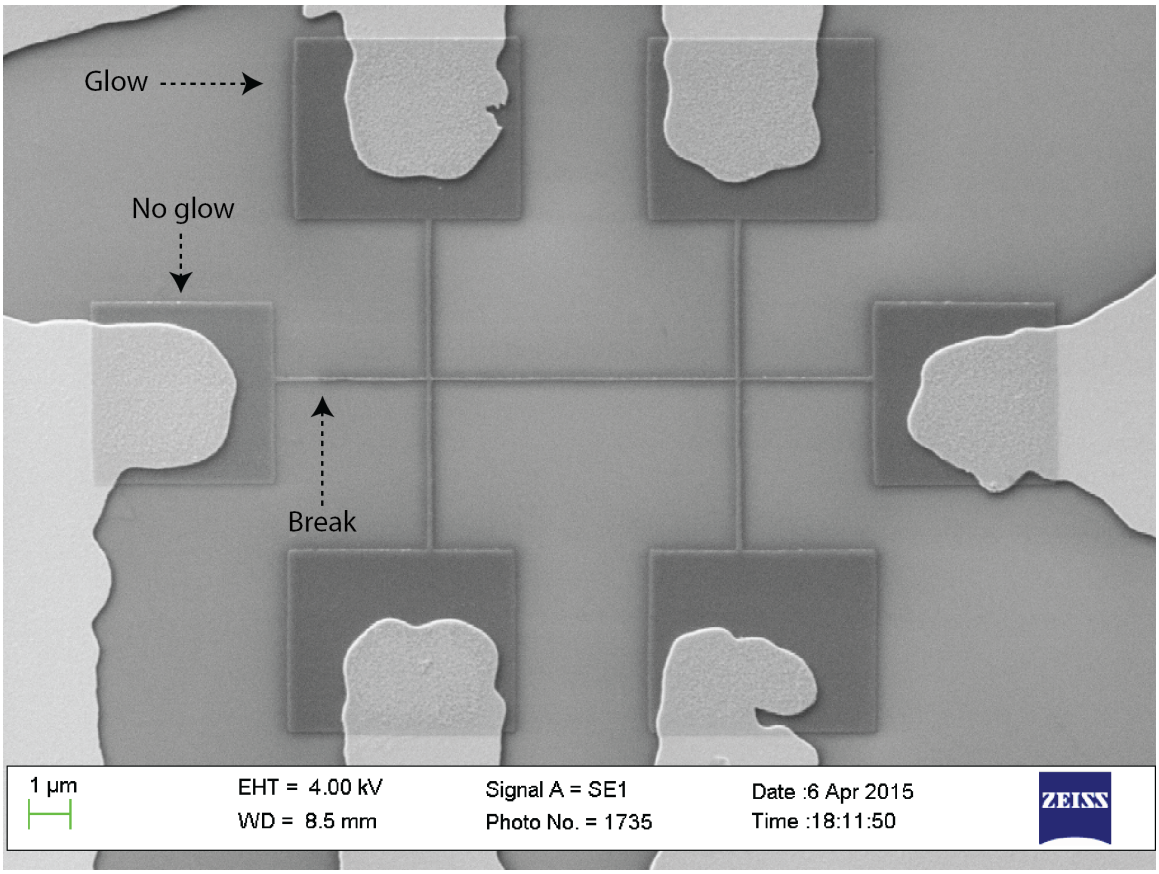

Figure 4.5: Checking connectivity in the SEM. When the sample is coupled to a large metallic object (in this case, the leads), it will reflect fewer electrons than one that is disconnected. This shows up as a slight dark halo around the sample at low accelerating voltages. Here we see a otherwise invisible break in the wire that we are able to image on the SEM.

if it is sensitive to electrostatic discharge. An example of this can be seen in Figure 4.5.

4.3 Sample Measurement

In theory, performing low-temperature transport measurements is a simple act (this is why experimentalists often need to be wary of theorists proposing "simple"

measurements!). One either applies a current and reads a voltage, or applies a voltage and reads a current. In practice, setting up these transport measurements in a way that isolates the effects in the device from the instrumentation and its environment is much more difficult task. The Indeed, the fact that physicists "specialize" in either theory or experiment at the onset of their professional training shows the value placed in this knowledge!

Much of transport measurement boils down to sophisticated ways to measure the device's resistance as a function of some other variable. The field of electronic transport (unsurprisingly) deals with electrons, so that "other variable" is something that interacts with the charge carriers in the system. Thus, in this thesis, we mainly deal with current/voltage/resistance measurements as a function of temperature, magnetic field, and gate voltage. Combinations of these three variables allow us to explore a rich variety of different states and phases of matter in our devices.

4.3.1 Cryogenics

Looking at many electronic systems at room temperature is like trying to read through a frosted glass window: you might be able to make out there is a book on the other side, but you won't be able to tell if it's Tolstoy or Twilight. Thermal fluctuations often mask the much more interesting physics that are occurring in a device, so it is almost always the case that colder is better. However, "colder is better" is only half of the story, and "colder is better and different" is a more complete

description. New electronic phases appear as materials get colder and the energy associated with the thermal fluctuations become smaller than other energy scales in the system. Thus, studying materials at cold temperatures can tell us more about the underlying electronic structure that was hidden by the thermal energy.

However, colder measurements come at a price in both money, time, and complexity. Each order of magnitude closer to absolute zero comes with corresponding increase in all of the aforementioned categories. Thus, we need specialized tools and methods to get down to cryogenic temperatures.

4.3.1.1 Helium Dewar

Liquid helium has the lowest boiling point for all the elements at 4.2K, so it is the cryogen of choice when dealing with extremely low temperatures. Liquid helium needs to be well-isolated from room temperature so that it does not all boil off more quickly than we can do a measurement. This is an issue both because liquid helium is expensive as well as transferring helium constantly is inconvenient and limits the length of measurements. To do that, it is stored in well-insulated storage dewars specifically designed to hold liquid helium. The liquid helium is stored in the middle of the dewar, surrounded by a layer of insulation. In order to decouple the interior from the exterior further, the entire inside is pumped down to high vacuum around 10^{-7} Torr. In addition, an outer liquid nitrogen jacket is also used which reduces the amount of radiative heat transfer to that of liquid nitrogen at 77K. All of this is to

limit the boil off of liquid helium and ensure our experiment stays cold.

Our lab had two helium dewars that we used in cryogenic measurements: an Oxford Kelvinox dewar, and a dewar from Precision Cryogenic Instruments. Both have a superconducting magnet that can be brought up to 8 Tesla. These magnets are controlled by an IPS-120-10 magnet controller and an American Magnetics Power Supply with custom analog equipment, respectively. The Oxford magnet can be brought to a maximum of 10T if a lambda pump is used on the bath.

The easiest way to cool something down to cryogenic temperatures is to place it in a bath of cryogenic liquid. For measurements that do not have to go below 4.2K, simply placing the sample in such a "dunker" will suffice. However, aluminum's superconducting critical temperature is 1.2K, so in order to study its superconducting effects we must reach colder temperatures. One way to do that is to pump on the bath, which due to evaporative heating cools the cryogen. However, pumping on the whole bath itself wastes a great deal of helium, so instead we isolate our sample from the bath in a vacuum chamber and thermally link it to what is called a 1K pot. This chamber pumps liquid helium from the bath into a small secondary reservoir (the 1K pot) which in turn is pumped and evaporatively cooled. This cools the 1K pot down to (unsurprisingly) about 1K, but uses far less helium than cooling the entire bath. By adjusting the impedance of the pumping line and matching the amount of helium being pumping out to the amount being brought in, this process can occur continuously and thus cool down the sample stage to 1K.

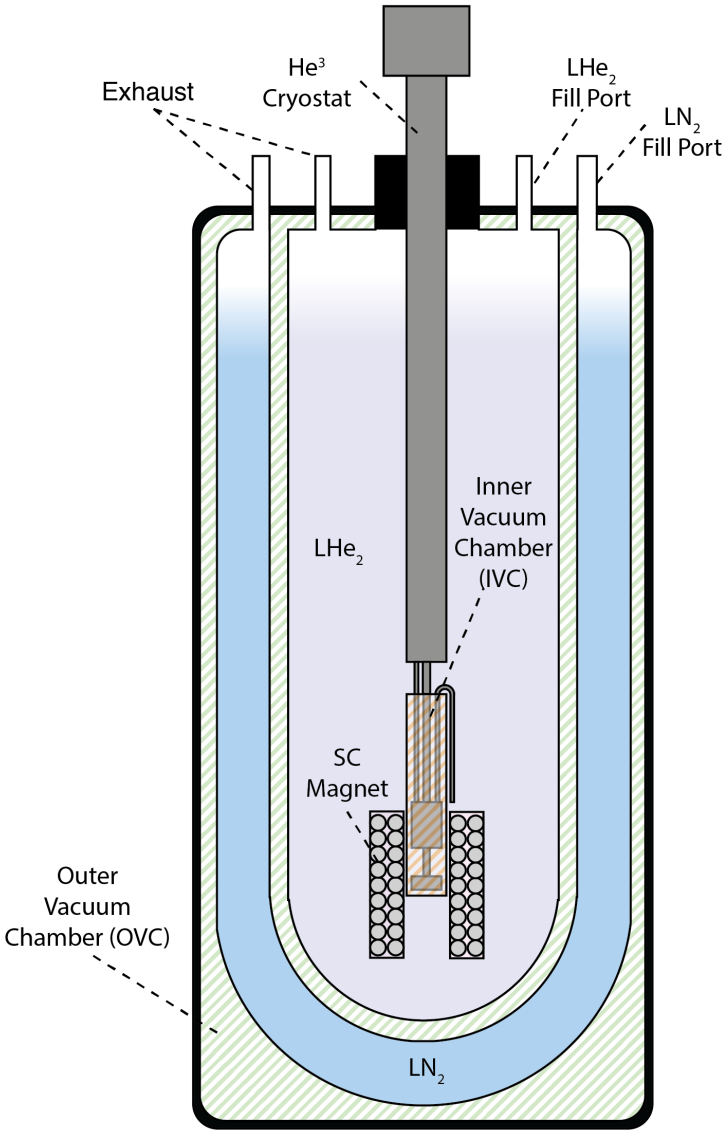

Figure 4.6: Schematic of helium dewar with He^3 cryostat inside. The dewar is designed to minimize heat transfer to the inner helium tank. First, the interior space is pumped to a high vacuum to minimize convective heat transfer. The liquid helium tank is also surrounded by a layer of super insulation and a liquid nitrogen sheath, which lowers the radiative heat transfer to that of liquid nitrogen (at 77K). The sample sits in the middle of a superconducting magnet, which can produce fields up to 8T. This magnet can be run as long as it is covered in helium, otherwise it runs the risk of quenching. The liquid nitrogen exhaust is released to air, but the liquid helium is recycled by outputting the exhaust to our buildings helium reclamation plant.

4.3.1.2 He^3 Refrigerator

Although aluminum goes superconducting at 1.2K and the 1K pot allows us to go just under that temperature, many quantum effects cannot be observed unless the sample is cooled much further away from the superconducting critical temperature. Thus, we need some other technique to get us to an even lower temperature. He^4 cannot be evaporatively cooled below 1K because it becomes a superfluid at 2.2K. We can cool the sample down further by using a different isotope of helium, He^3.

Due to He-3's odd number of nucleons, it obeys fermionic statistics and thus does not turn into a superfluid (at least not until a much lower temperature). It can thus be cooled down using evaporative cooling much lower than He^4 can. However, He^3 is an extremely rare isotope and is only produced as a by-product of nuclear weapon production or extracting in small amounts of natural gas, so it cannot be used in the same manner in which we pump He^4 . A He^3 refrigerator is thus designed around the constraint of preserving the gas.

A He^3 fridge works by evaporatively cooling a small reservoir of He^3 liquid. The He^3 gas is stored in a sealed off chamber with a charcoal sorb and heater inside. The charcoal sorb is at the top of the chamber with part of the chamber in thermal contact with a 1K pot right below it. The charcoal sorb has a extremely large surface area for its size, and when it is cold enough captures He^3 atoms on its surface. When the entire device is cooled down to 4K, the charcoal sorb absorbs the He^3 almost entirely. However, we then apply heat to the heater in the chamber and heat up the sorb to

30K, which releases the He^3 gas. After the gas is released, we then start pumping on the 1K pot. The relatively hot He^3 gas hits the cold surface of the 1K pot, and thus condenses (much like droplets of water condense on the exterior of a cold beverage). These droplets of He^3 condense and fill up the lower half of the chamber. After all of the helium-3 has condensed, the heater is turned off and the sorb cools back down. As it cools, it starts reabsorbing the He^3 gas and thus starts pumping the chamber. This evaporatively cools the He^3 and brings the temperature down to 250-400mK. The fridge can hold this temperature from 12-48 hours, depending on the model of the fridge.

The operation of the fridge is simple, but requires care in ensuring the vacuum in the IVC is robust and that the lines do not have any impurities that can freeze and clog them. The vacuum thermally separates the inner cold He^3 stage from the 4.2K bath, which requires a pressure less than 10^{-6} Torr. The lines are flushed a few times with helium gas and pumped in-between each flushing, which ensures that only helium is inside of them. The chamber is sealed with a cone seal and vacuum grease, but must be cleaned with IPA between each use so the seal is robust each time. If the IVC has a charcoal sorb, it should be heated up with a heat gun to remove any moisture it might have absorbed (as water impedes its ability to pump on the IVC at low temperatures). Before the fridge is cooled down, a small amount of exchange gas (about 1-2cc) needs to be put into the IVC in order to quickly bring the whole interior down to 4K when it's immersed in the bath. If no exchange gas is used, the

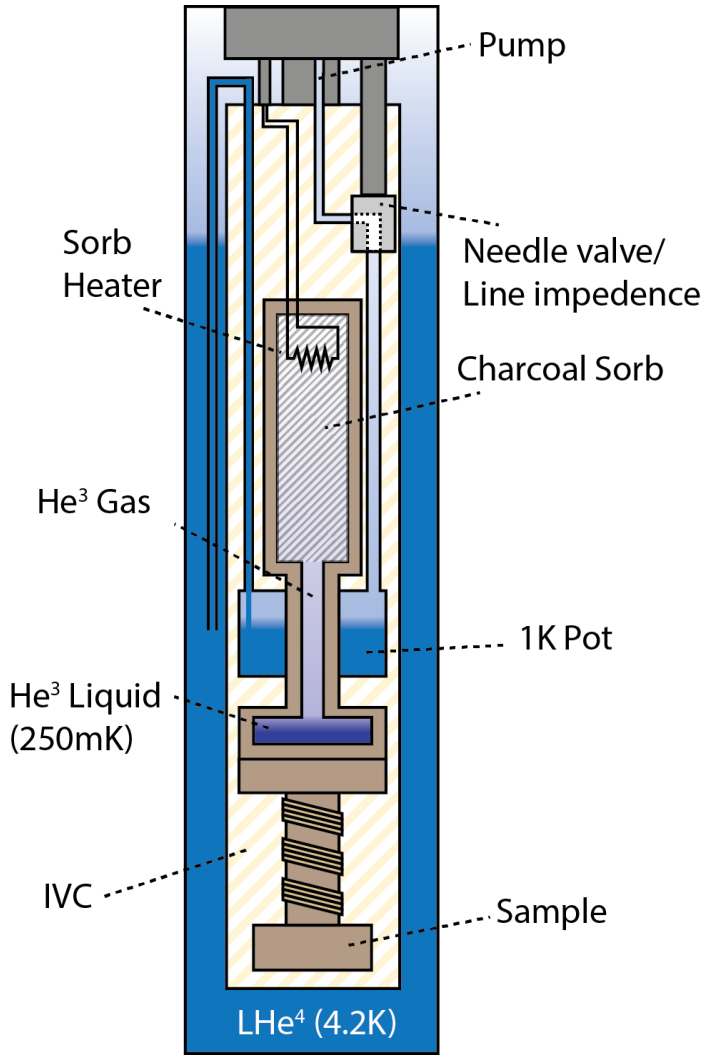

Figure 4.7: Schematic of a He^3 cryostat. A He^3 fridge works by in a closed-cycle by evaporative cooling of a small bath of He^3 liquid. The system starts out at 4.2K once it comes into thermal equilibrium with the helium bath (the vacuum in the IVC decouples its contents from the bath, so this can take a while). The cool down process begins by pumping a small amount of liquid helium into the 1K pot, which is thermally linked to the He^3. By pumping at precisely the right rate (controlled by either a needle valve or by precisely adjusting the pumping impedance) the liquid helium is continuously cooled down to 1.2K. The sorb heater is then turned on, which releases the He^3 gas in the charcoal. This gas condenses on the regions coupled to the 1K pot and drips down to the He^3 chamber. After all the He^3 is condensed, the heater is turned off and the sorb begins to pump on the liquid, evaporatively cooling it down to approximately 250mK.

system can take up to 2 days to reach 4K, as compared to a few hours. If too much exchange gas is used, the system will boil off a great deal of helium, so care must be taken. If it does not have an IVC sorb, the IVC needs to be pumped below 10^{-6} Torr when everything is equilibrated at 4K. Otherwise the system will not be able to be cooled down to base temperature.

He^3 fridges only have a set amount of cooling power before they warm back up to 4K, so any unintentional heat loads on the sample due to the measurement process should be minimized. In order to adjust the temperature of the sample, heat can either be applied to the sample holder itself or to the sorb heater. Applying heat should ideally be done with a well-tuned PID controller, as manual control is quite difficult and time consuming. Unless the temperature sensor is in very good thermal contact with the sample, the temperature needs to be changed adiabatically so everything has time to equilibrate and the temperature sensor is accurately tracking the device. If the temperature sensor is far away from the device itself and the temperature is changed too quickly, the sensor reading will not correspond to the actual temperature of the device being tested.

We have two separate He^3 fridges that have been used for these experiments. The Oxford Heliox system is controlled by an ITC-503 temperature controller, and an older RMC He^3 Insertable Cryostat with the temperature controlled by a Neocera LTC-21 Temperature Controller. The newer system differs from the older in that it has an adjustable pumping impedance to the 1K pot through a needle valve, so the

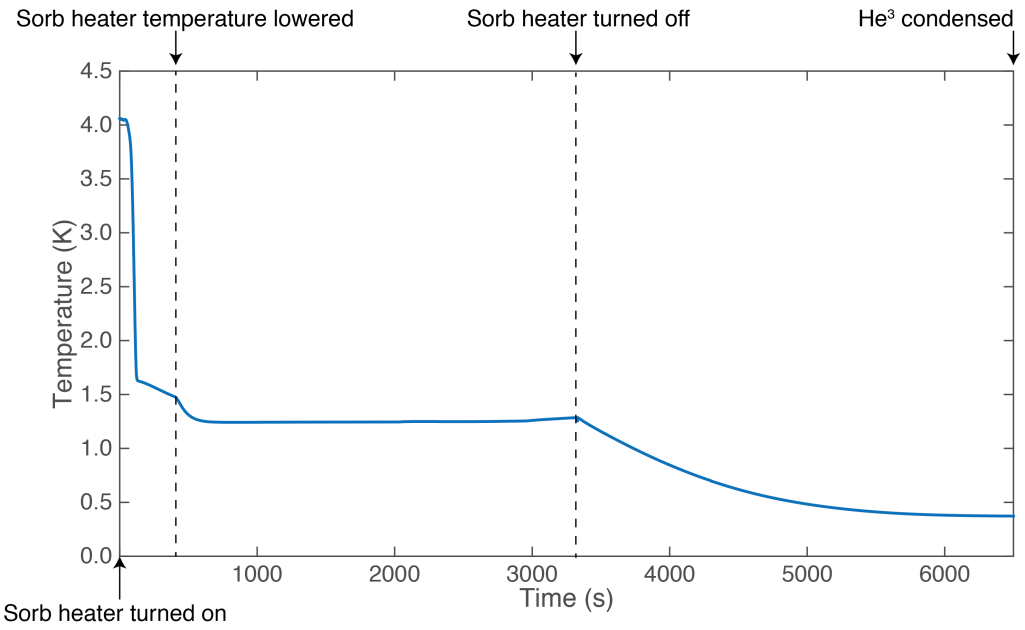

Figure 4.8: Plot of temperature over time during the cool down process in a He^3 fridge.

He^3 gas can be condensed much more quickly and the cooling power can be better controlled. This is in contrast to the RMC system, which has a fixed impedance exactly matched to the one needed to cool down the system. However, the 1K pot control for the newer system eventually failed when the force to overcome the static friction to turn the needle valve increased greatly and it could no longer be controlled by the PID controller. This combined with a leak in the 1K pot forced us to update and use the older system to interface with our equipment.

4.3.1.3 Helium Recovery System

While helium is one of the most abundant elements in the universe, it is a limited resource on Earth because it escapes the atmosphere when released into air. Helium

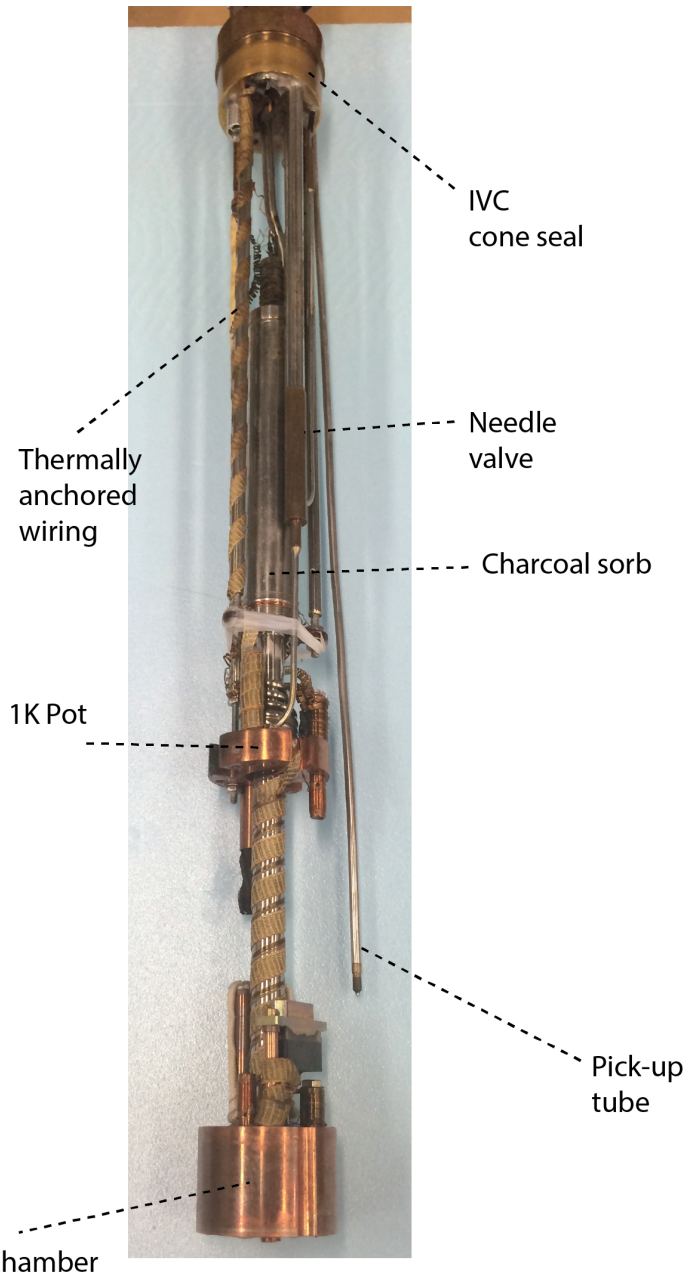

Figure 4.9: Description of a Heliox He^3 cryostat. The sample is attached to a removable sample holder at the He^3 chamber at the bottom. The electric wiring connecting the instruments down the sample is thermally anchored to the 1K pot to minimize heat transfer to the sample.

is an increasingly important resource when it comes to cryogenics used in industry and research, and thus should be preserved if possible. Not only is it important because we only have a limited quantity available, but also because of its increasing cost. Thus, reclaiming the spent helium is important if possible.

Our department has installed a Cryomech helium reclamation plant with those constraints in mind. All of the warm helium gas boiled off from our storage dewars is channeled through pipes leading to a large bag that acts as a buffer. Before entering the bag (and several times through the process) the gas travels through filters filled with desiccation pellets that remove the water vapor from the system so it does not freeze near the cold heads and clog the lines. Once the bag fills up to a certain level, a compressor takes the helium gas and pumps it into high-pressure storage tanks. These tanks then feed the gas through two sets of liquid nitrogen cold traps to get rid of impurities: the first to get rid of the organic material from the PVC pipes bringing in the helium from the building, and the second to get rid of oxygen and nitrogen. After the traps, the now-pure helium gas is condensed on three cold heads into the main storage tank. The helium can then be transferred into smaller portable storage tanks and brought back to the lab storage dewars, completing the cycle.

4.3.2 4-probe measurement

One of the main challenges of doing transport measurements is separating the effects intrinsic to your sample from interference from the outside world and your

instrumentation. A type of measurement schema that minimizes these effects is called a four-probe (or four-point) measurement. In a four-probe measurement, the voltage across your device is read through separate leads from where the current is applied (or vice-versa). The only changes in the potential from the current applied that are recorded are the ones in-between the voltage leads, so this isolates the region being measured to the device being studied. See Figures 4.10 and 4.11 for schematics of this set-up.

If the sample cannot be put into a true four-probe configuration, a pseudo-four-probe measurement that removes the noise from the cryostat can be created by wire-bonding both the voltage and current leads to a single optical lead. This set-up removes the potential offset that results from running current through the cryostat wiring leading down to the sample holder.

4.3.3 DC Measurement

When the device is ready to be measured, we can either apply a current and read a voltage, or apply a voltage and read the current. One way to do this is to simply connect a battery or current source to the sample and read the voltage (or current). By applying a set current and reading the voltage, you can thus interpret the resistance of your sample. By constantly measuring this quantity and changing another variable (such as the magnetic field, temperature, or gate voltage), you can get the resistance/conductance as a function of that variable.

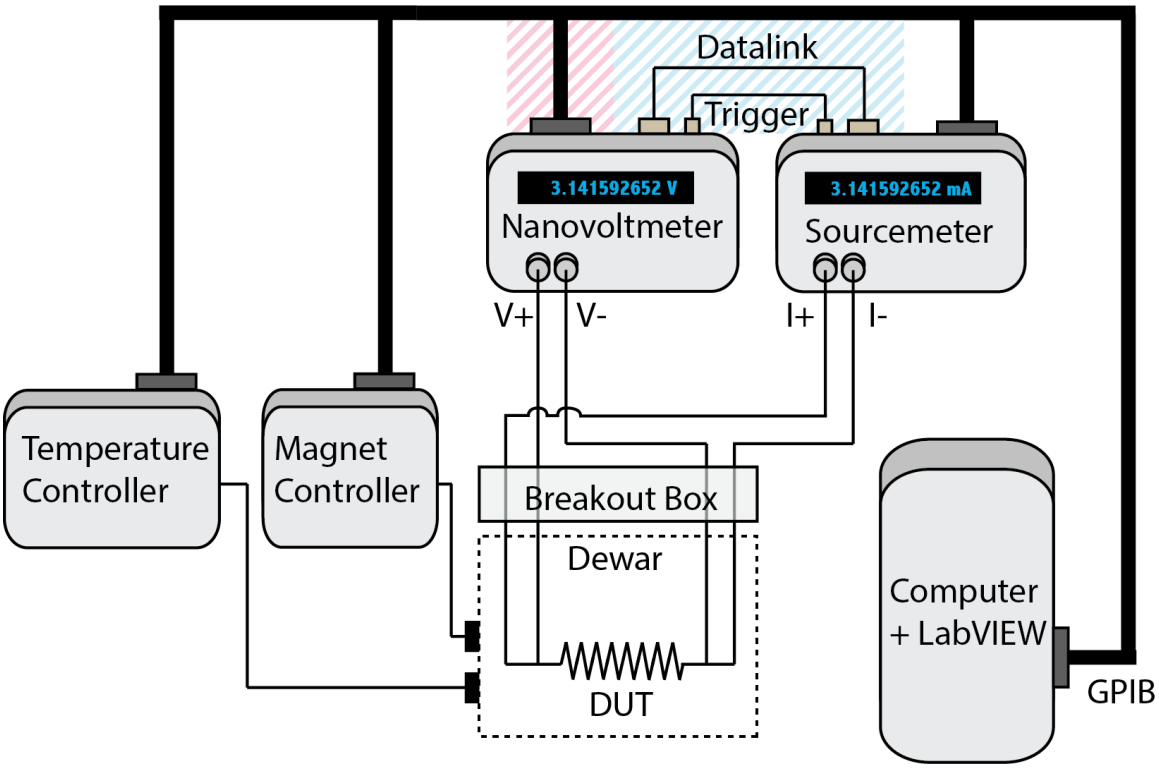

Figure 4.10: Schematic of a DC measurement. All DC measurements were performed with a Keithley 2182A Nanovoltmeter and a Keithley 6220 Sourcemeter. Two measurement set-ups were used: one for resistivity measurements (shown in the red lines, and one for I-V measurements (shown in the blue). The resistivity measurements used the source meter to apply a fixed current across the sample while the nano voltmeter read the voltage through two separate sets of leads, controlling and measuring everything through GPIB. However, the GPIB communication protocol is slow, so acquiring fine-grained I-V data is difficult with this set-up. To fix this, we disconnect the GPIB and control the nanovoltmeter through the sourcemeter, as they are designed to work together as a pair. A 700 point I-V curve can be taken in 30 seconds, as opposed to the approximately 15 minutes it would take via GPIB.

Our lab has several pieces of equipment suitable for running DC measurements. First, we have a Keithley 6220 current source and a Keithley 2182 nanovoltmeter that in combination provide a robust measurement set-up. The current source can output extremely small currents across the device-under-test (DUT) and the nanovoltmeter can read similarly small voltages. These two pieces of equipment are also useful in that they can communicate and trigger each other, which with the proper scripts written for them can speed up data acquisition greatly. Indeed, by using the current source to trigger measurements on the voltage source, sweeps of the current-voltage characteristics can be taken orders of magnitude faster than communicating to them both separately by GPIB.

While simple, DC measurements do have some intricacies that need to be taken into account. Any capacitive link in the measurement will be charged by a DC voltage, and thus might result in an offset in the voltage measurement. By reversing the bias on the measurement, these offsets can be detected and accounted for while analyzing the data afterwards.

4.3.4 Lock-in Amplifier

When noise is a concern and particularly interference from outside the measurement environment, using a lock-in amplifier (LIA) can make your life much easier. A lock-in amplifier uses the orthogonality of the trigonometric functions in order to separate out the signal from the noise. It does this by applying an AC current of

a specific (user-defined) frequency across the sample. By measuring the resulting potential change across the sample and mixing it with the original output voltage, just the signal that is the result of the output current will be read. An AC voltage is thus like an extremely good notch filter, centered on the frequency that you choose to be the output. This set-up is extremely sensitive to both changes in amplitude and phase, as a 90 degree phase offset will result in a signal amplitude of zero. It is then important to adjust the phase for each measurement to be at a maximum, as the capacitance of the system combined with the resistance of the wiring will result in a slight phase change between the source and the signal. In addition, this is a good way to troubleshoot bad connections, as anything greater than a 90 degree offset is usually the result of a bad capacitive connection rather than an ohmic one.

This measurement schema can be shown in Figure 4.11. The Princeton Applied Research 124A LIA outputs a voltage ranging from 0.1V to 10V. By applying this voltage across a resistor much larger than the resistance of the sample (on the order of tens of megohms), the AC voltage output is converted to an AC current. As an example, 10V across 100MΩ gives a current of 100nA. This resistor should either be metal film or wire wound, as carbon film resistors have substantial $1/f$ noise that can interfere with these relatively low-frequency AC measurements. This current is applied across the sample through two leads and the voltage is ideally read through two separate leads. The input voltage range can be changed anywhere from 100nV to 100mV. The 124A is an entirely analog device, so for this value to be recorded

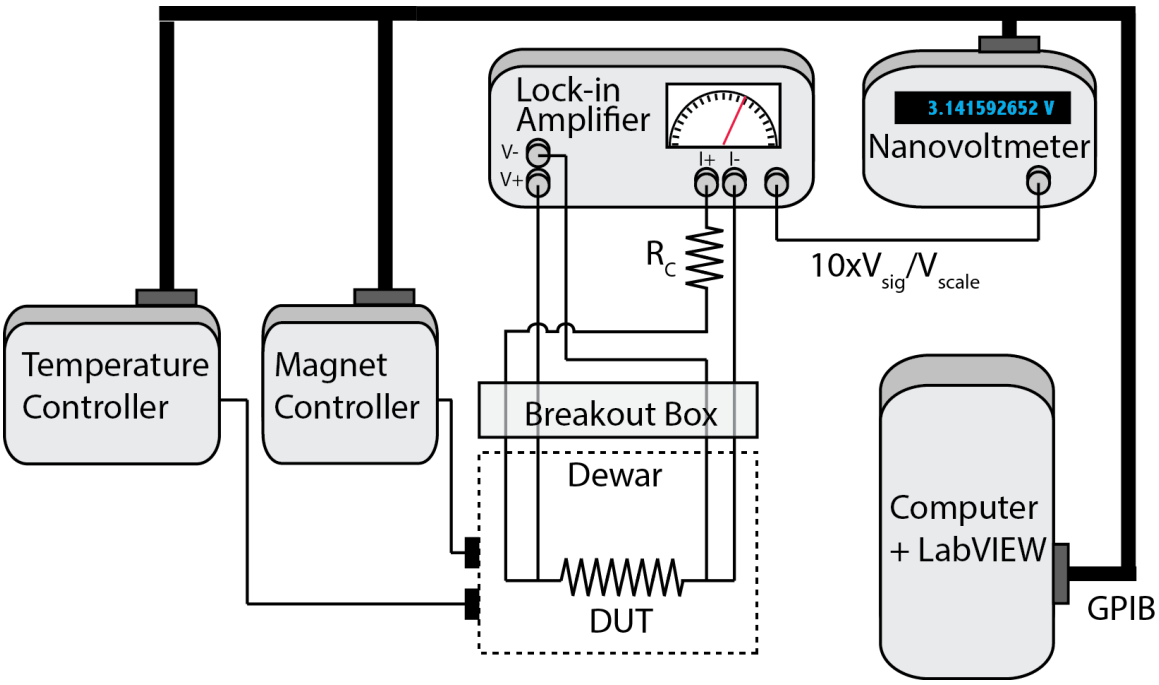

Figure 4.11: Schematic of an AC measurement. The lock-in amplifier outputs an fixed AC voltage at a user-defined frequency. Applying the voltage across a resistor R_C with a resistance much greater than the device-under-test (DUT) in effect transforms this AC voltage source into an AC current source. This signal is then read into the lock-in, which outputs this voltage on the dial divided by the user-defined voltage maximum (V_{scale} in figure). This model of lock-in is purely analog, so there is no way to acquire this directly. Instead, the dial reading is output on a scale of -10V to 10V, and we read this level in via GPIB with the Keithley nanovoltmeter.

it needs to be digitized. To do that, it has a BNC output which outputs a voltage scaled by the input voltage range in this manner

$$V_{out} = \frac{V_{in}}{V_{range}} \tag{4.1}$$

This voltage can be read directly into a DAQ board, but it is rather noisy by itself. Instead we read it into a Keithley 2182 Nanovoltmeter with a low-pass filter enabled.

4.3.5 Noise Measurement

A good portion of an experimentalists toolbook is dedicated to techniques for getting rid and seeing through noise. Complex filtering techniques combined with long averaging times and expensive low-noise equipment is standard for sensitive measurements. However, a distinction needs to be made between intrinsic noise and interference. Interference refers to signals originating from outside the measurement set-up, and is always detrimental. Noise intrinsic to the device itself, such as Johnson-Nyquist noise or shot noise, can be used to tell us information about the sample itself.

A sensitive measurement of the thermal noise knowing the device's resistance can directly tell us its temperature. This is because the thermal noise is directly proportional to the temperature of the device. This can be used to create a heat sensor directly on the sample by fabricating a long meandering line with a set resistance, which will output a noise proportional to the temperature (as long as it remains

metallic through the temperature range being studied).

Shot noise is the fluctuation of the voltage associated with fact that the current is not a continuous substance, but rather is carried by individual charge carriers. The arrival of each charge carrier to the voltage leads results in a pulse of current/voltage, and on average this results in the overall steady state current/voltage we read. Because the arrival is a random process, there are fluctuations around this steady state current/voltage that are proportional to the charge of the carrier itself and the amount of current applied. By measuring this noise and scaling it by the amount of current applied, the actual charge (proportional to the elementary charge) can be determined. This is measuring what is called the Fano factor for the device.

4.3.5.1 Cross-correlation

Noise measurements are notoriously difficult to do, as they often involve very small intrinsic noise signals bathed in a much noisier background. By measuring the noise as a function of time and performing a Fourier transform on it, the noise level as a function of frequency can be seen. The result is usually a large $1/f$ background superimposed on a series of noise spikes from outside interference and line noise. At high enough frequencies, the $1/f$ noise and interference spikes related to harmonics of the line noise disappear, and all that is left is a white noise background (white noise referring to noise that is independent of frequency). This white noise is important, as shot noise and thermal noise both have a white spectrum so reading that level tells

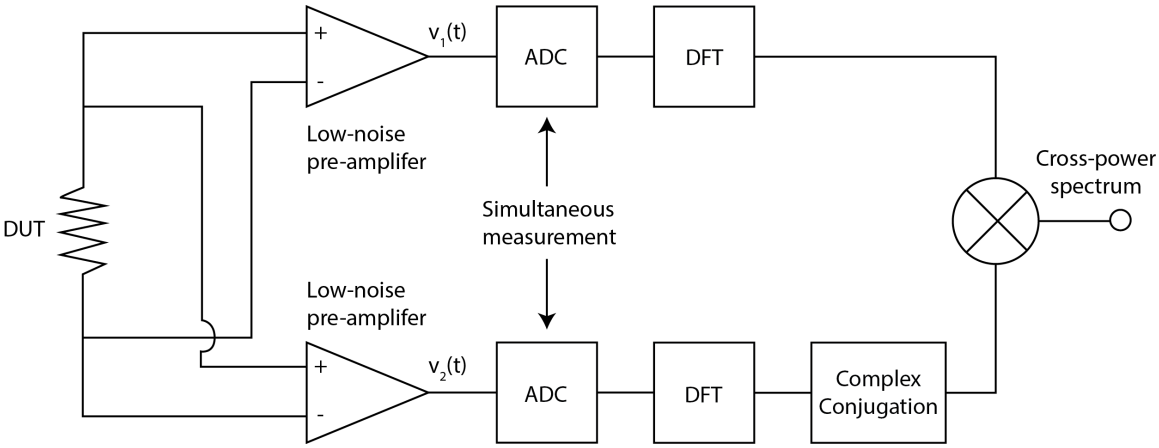

Figure 4.12: **a)** Schematic of the cross-correlation process. The signal is first split into two as close to the device-under-test (DUT) as possible. These two signals are then amplified well above the base quantization level of the analog-to-digital-converter (ADC), and sampled at the same time. The amplifiers will add some noise to the signal, but the noise between the two will be uncorrelated, so it will drop out in the end to the process. The now-digital signals undergo a discrete Fourier transform and we multiply one with the other's complex conjugate. The final result is the cross-power spectrum, which after averaging over multiple runs converges to the actual power spectrum of the device without all of the additional noise from everything after splitting the signal.

you those quantities.

Normally, shot noise measurements are done at very high frequencies in order to avoid from all the various sources of low-frequency noise. However, high frequency measurements are difficult in their own right, and there is another way to get around the mess of low-frequency. If you take two simultaneous samples of the noise, you can compare the two waveforms. The parts of the signal that are intrinsic to the sample will be the same, while the noise from everywhere else (such as the instrumentation, interference along the lines, and thermal noise from the long resistive signal lines) is different between the two. Cross-correlation is the method to figure out this difference.

If the noise is uncorrelated between the two waveforms, the frequency spectra are also going to be different. By taking the Fourier transform of each and multiplying one with the complex conjugate of the other, you get what is called the power cross-spectrum. By taking this data repeatedly and averaging each cross-spectrum, the uncorrelated noise parts drop out and just the signal remains. Each frequency bin on the Fourier spectrum converges independently as $1/\sqrt{m}$, where m is the number of trials. By taking the average cross-spectrum and then averaging all of the frequency bins of the average, the calculated noise value converges quickly. The time it takes to converge on the actual value is a strong function of the ratio of the uncorrelated noise to the correlated noise, so it is still prudent to remove as many sources of interference and unimportant noise as possible.

4.3.5.2 Custom Amplifiers

In order to actually read these small signals into a analog-to-digital converter (ADC), we need to amplify them several orders of magnitude. A high precision ADC still has a minimum quantization step size on the order of microvolts, and in order to read actual waveforms our signal needs to be much higher than this. Since the noise values we are looking at are in the order of hundreds of picovolts, we need amplification on the order of 10^5 in order to fully capture the waveform. In addition, our amplifiers must have extremely low noise values, as any noise they add before the amplification will be included in the final noise spectrum and need to be removed by

cross-correlation.

The standard SR560 pre-amplifier has a base noise value of approximately 10nV, which is 100 times greater than the size of the signals we are trying to see. As the time it takes to converge on the actual noise value using cross-correlation is a strongly increasing function of the ratio of the external noise to the intrinsic noise, decreasing this value can vastly decrease the measurement time. We used a custom amplifier based on a design[12] that has a base noise value of 1nV/Hz, as well as a flat frequency response from 0.1-20000Hz. In addition, I have customized it by adding an additional amplification step to bring the amplification from 10,000 to 100,000, as well as additional low-pass filtering. The additional amplification does not contribute to the base noise since it occurs after the designed amplification, and helps resolve low-amplitude signals that would normally be close to the quantization level on the ADC (see Figure 4.14). The additional active low-pass Butterworth filter was added to dampen high frequency oscillations that were intermittently overloading the ADC.

In order to further remove sources of interference from our measurement, I created a Faraday cage to contain both the amplifiers and their batteries. This cage was created by purchasing two professional Wilton cake decorator pans and putting them on top of each other, drilling holes for the connections. The thick layer of aluminum created a cut-off frequency of approximately 3000Hz, above which all outside interference would be attenuated.

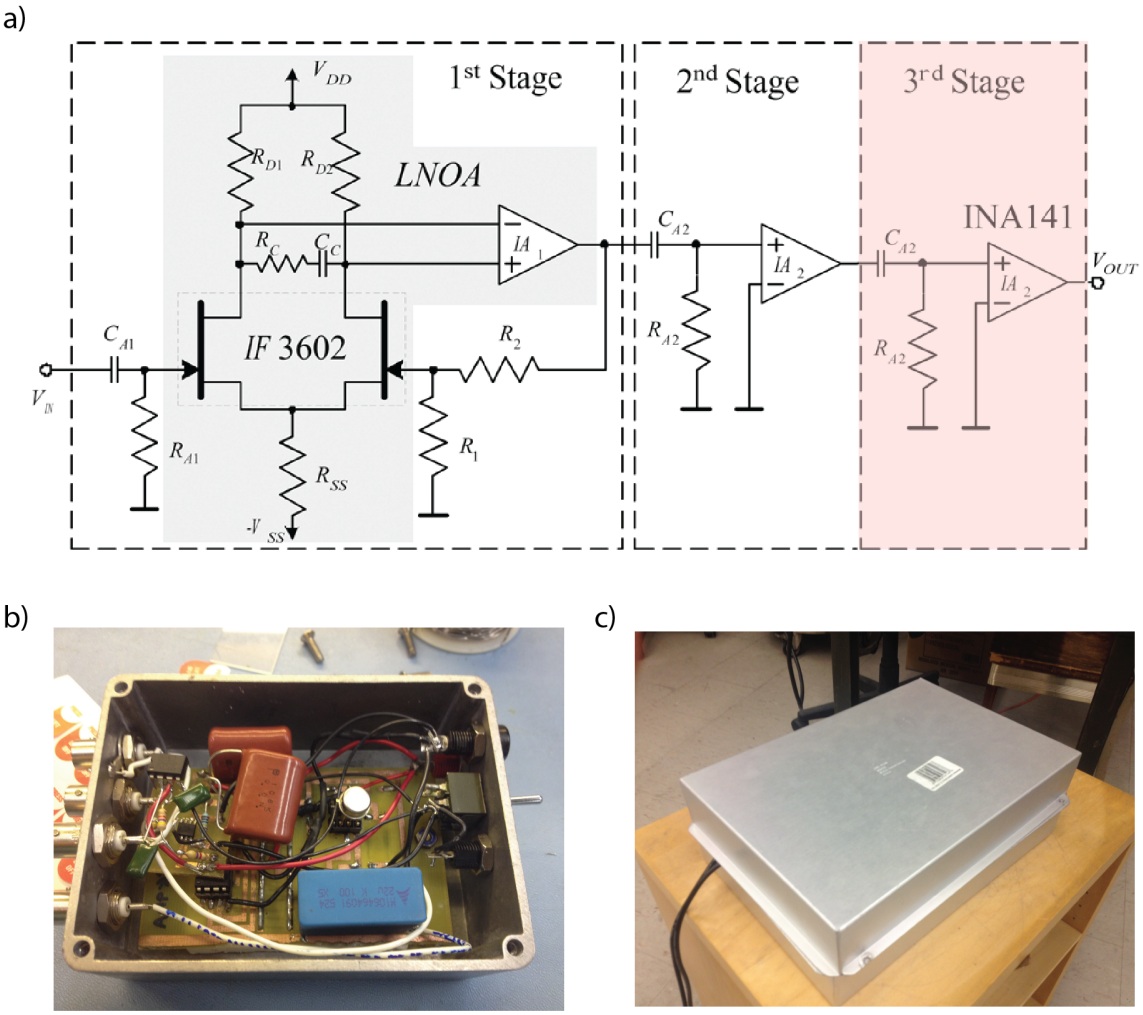

Figure 4.13: Custom amplifier design and Wilton cake-pan Faraday cage. We see here a slightly modified version of an amplifier designed for ultra-low noise amplification for low-frequency signals.[12] Part a) is the modified design, including another amplification step to bring the total amplification to 100,000 and not showing an additional low-pass filter at the output. Part b) is the actual amplifier's interior, and part c) is the Faraday cage made by placing two Wilton cake decorator pans on top of each other and clamping them together.

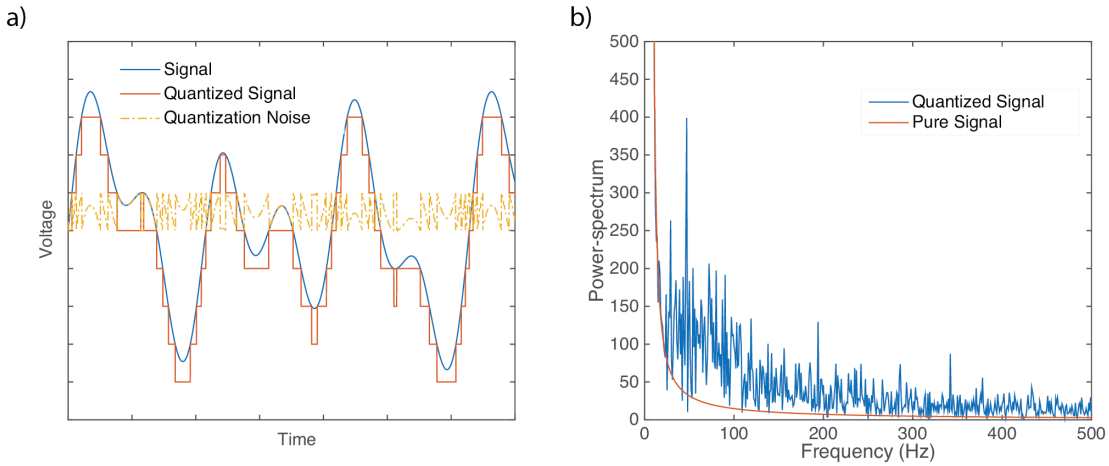

Figure 4.14: Demonstration of the effect of quantization noise. Part **a)** shows how representing an analog waveform digitally requires some degree of approximation, but if the signal is close to the step size of the ADC (given by the voltage range divided by 2^n, where n is the number of bits in the ADC) this noise can be significant. This is shown in part b, which is the Fourier transform of both the original signal and the quantized version. Increasing the signal size far above the step size of the ADC level can greatly reduce the effect of this noise.

4.3.6 LabVIEW

Interfacing with the equipment to actually collect the data is done in a variety of ways. There are libraries for Python, Matlab and a variety of languages for directly sending commands to equipment, but in this thesis I have used National Instrument's LabVIEW software to both control my experiments and collect data.

LabVIEW is a visual programming language, where data can be thought to move along "wires." As it travels along a wire, it can enter a VI, or virtual instrument, which acts much like a function in a traditional programming language. By hooking the outputs of these functions to other functions, data can be manipulated and presented quickly as the measurement runs. In addition, input variables can be represented in

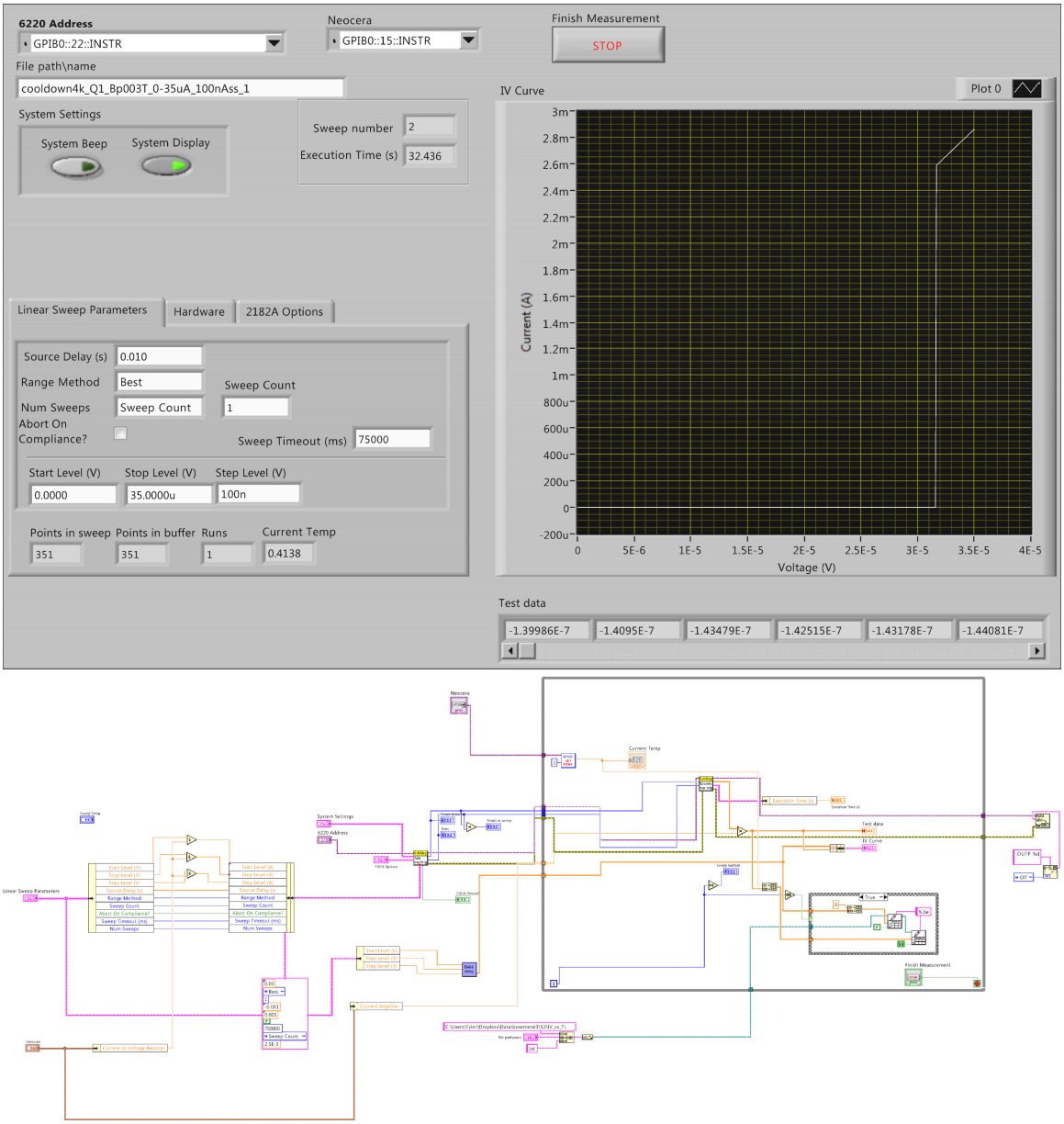

Figure 4.15: Picture of a LabVIEW program front panel and corresponding block diagram. Buttons and dials on the front panel initialize parameters to functions in the block diagram. Traditional for and while loops are represented by boxes that loop the code inside of them. By placing the data acquisition code inside a loop, long measurements can be performed.

a virtual "Front Panel" for the program and easy changed.

LabVIEW is particularly useful for data acquisition because of the large number of libraries available as well as the ease in prototyping a measurement (especially for National Instruments-designed equipment). However, it is not well suited for much more than acquisition, as actually analyzing the data in LabVIEW is awkward due to the confusing "spaghettification" of the code when it becomes more complex. Thus, once the acquisition is complete, the data was analyzed and plotted in a more suitable analysis-centric environment (such as Python, Matlab, and R).

Chapter 5

Etching

5.1 Introduction

Superconducting properties of a nanowire become significantly altered as its diameter is decreased to the order of the coherence length.[13] The superconducting transition itself becomes broadened[14,15] due to the phase slips, which can occur though thermal activation[16,17] or quantum tunneling.[18] As the temperature is further decreased towards absolute zero, one-dimensional nanowires are expected to undergo a quantum phase transition[19–22] between a superconducting and an insulating state. The nature of this transition generally depends on disorder, magnetic field, boundary conditions and the coupling to the environment. Superconducting nanowires could be a useful model system in which to study these effects, but in order to do a systematic study, one needs a variety of nanowires with well controlled properties.

CHAPTER 5. IN-SITU ETCHING OF ALUMINUM

Various methods have been used to fabricate superconducting nanowires with dimensions that are smaller than what is achievable by electron beam lithography: step edge method,[23] molecular templating,[24,25] electrodeposition into nanopores,[26,27] mechanical stencil methods,[28,29] and focused ion beam milling.[30] All these methods have succeeded in reducing the diameters of the nanowires and have enabled discovery of new phenomena, but each has its limitations and disadvantages. For example, ion milling will typically damage the samples to some extent by ion implantation, molecular templating offers very little control over the size and the structure of the wires, and the electrodeposition in nano-pores yields nanowires that usually remain encapsulated in the nanopores. Additionally, most of these methods do not lend themselves to four-probe measurements, nor offer good control of the dissipative environment.

In this chapter, I describe a controlled etching method for fabrication of uniform aluminum nanowires with diameters below 15nm. The resistance is measured *in situ* as the wire is being etched, allowing a precise control of normal state resistance of each wire. Given that aluminum is often the material of choice in superconducting devices, this method offers a clean and controllable alternative for fabrication of superconducting nano-structures on a variety of substrates.

5.2 Sample preparation and etching mask creation

We start with clean silicon substrates, on which we define gold bonding pads using standard ultraviolet lithography and thermal evaporation. The substrates are then cleaned and spin-coated with 4% poly-methyl-methacrylate (PMMA) at 4000 RPM, patterned using electron beam lithography (EBL), and developed using the cold methyl isobutyl ketone (MIBK) process.[31] 80-100nm of aluminum is thermally evaporated onto the substrate in a vacuum of 10^{-7} Torr. After evaporation, the nanowires are sonicated in acetone to achieve uniform lift-off. Fig. 5.1 shows a schematic of a nanowire before, during and after the etching process. The nanowires are patterned in a four-probe configuration, as shown in Fig. 5.1.a., with dimensions of 200nm in width and 5μm in length, as measured between the voltage leads. The samples are then wire-bonded to the chip carrier using 25μm wide aluminum wires. After wire-bonding, a layer of 4% PMMA is spun at 4000 RPM on top of the sample, and a window is created using e-beam lithography, as shown in Fig. 5.1.b. The window defines the area that is to be etched, while the PMMA protects the rest of the sample, serving as the etching mask. See Chapters 3 and 4 for more information on the fabrication process.

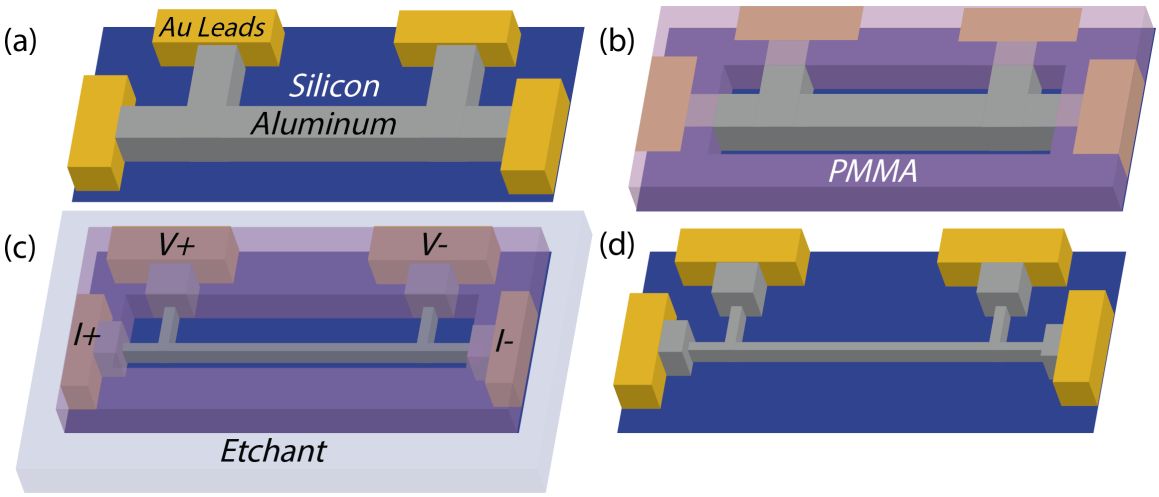

Figure 5.1: (a) An aluminum nanowire with a four-probe lead configuration is created using electron beam lithography and thermal evaporation of 80-100nm of aluminum on top of pre-fabricated gold leads. The gold leads were fabricated using optical lithography and thermal evaporation of 5nm of Cr, followed by 80nm of Au. (b) The gold leads are wire-bonded to a chip carrier, and a PMMA etching mask is created using electron beam lithography. (c) As a drop of the etching solution is placed on the sample, the area defined by the window in the PMMA mask is etched, while the resistance of the sample is monitored in a four-probe configuration. (d) When the desired resistance is reached, the etching is stopped by removing the droplet of the etchant using N_2 gas. The PMMA is then dissolved in acetone, leaving only the etched wire.

5.3 Sample etching and measurement

At this point, the sample is connected to a lock-in amplifier (Princeton Applied Research 124A) and the resistance is measured in a four-probe configuration (typically using 100nA at 27Hz, see Chapter 4 for details). To begin the etching process, a droplet of the solution can now be placed on top of the sample. The etching solution was 100mL deionized water : 5g sodium bicarbonate : less than 50mg sodium nitrite. The concentration of the sodium bicarbonate was chosen in order to set the pH between the barrier of the corrosion and passivation zones in the Pourbaix diagram for aluminum.[32] The trace amount of sodium nitrite acts to prevent over-oxidation of the aluminum, which would result in insulating nanowires. As the area defined by the PMMA mask is etched, as shown in Fig. 5.1.c., the resistance is monitored as a function of time. When the desired resistance is reached, the solution is removed using compressed N_2, and the PMMA is dissolved in acetone, leaving a thinner, narrower nanowire (Fig. 5.1.d).

5.4 In-situ etching data

The resistance as a function of time for three representative nanowires is shown in Fig. 5.2. One of these nanowires was etched all the way through, to the point where it was no longer electrically connected (shown in green in 5.2). Another nanowire was etched until the resistance reached 1600Ω, at which point the etching process

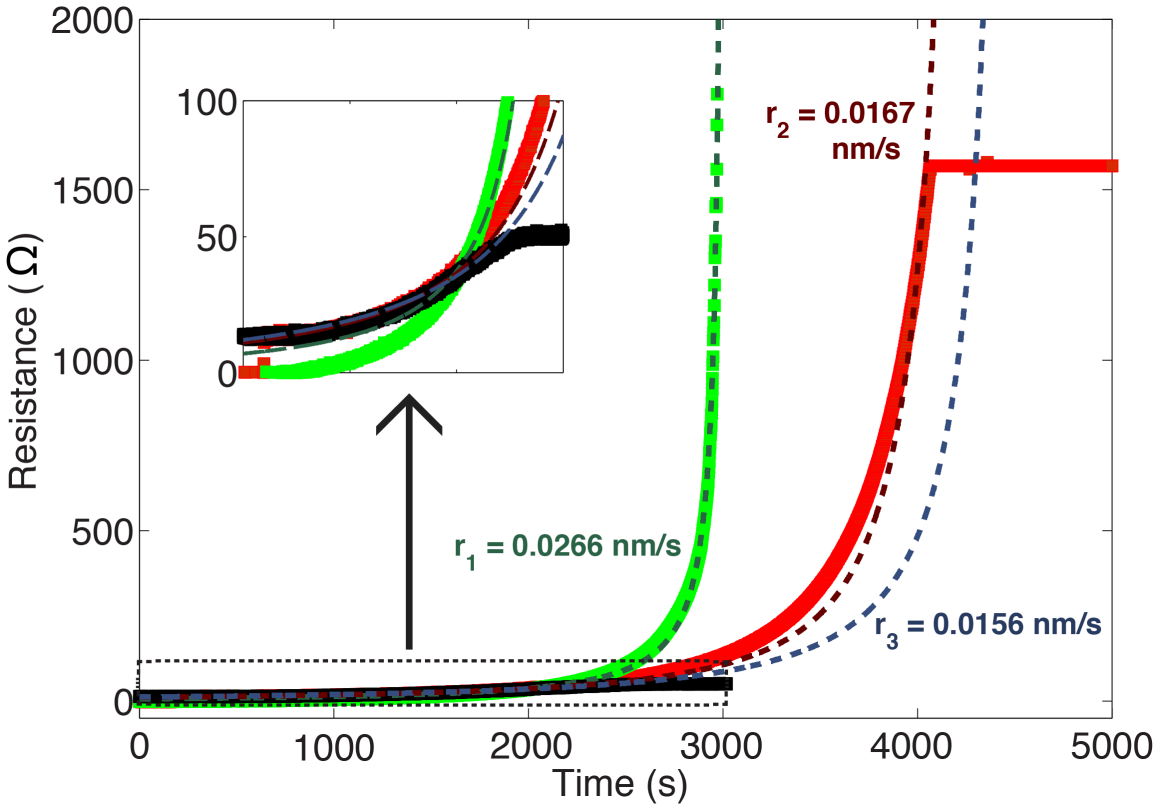

Figure 5.2: Resistance as a function of time for three aluminum nanowires (solid lines), measured during and after the etching process. Nanowire 1 (green) was etched all the way through, and its resistance diverged when the wire was no longer continuous. Nanowire 2 (red) was etched until its resistance reached 1600Ω, at which point the etching solution was abruptly removed, and nanowire 3 (black) was etched until the resistance reached 50Ω. All wires were 5μm x 80 nm x 200 nm. The inset zooms in the lower resistance region to show that the resistance of nanowire 3 remains at 50Ω after the etching is stopped. The expression in Eq. 5.1 was used to fit the data, using the etching rate as the fitting parameter. The fits are shown as dashed lines, with the extracted etching rates shown for each nanowire. All three nanowires were etched at the ambient temperature of 25°C.

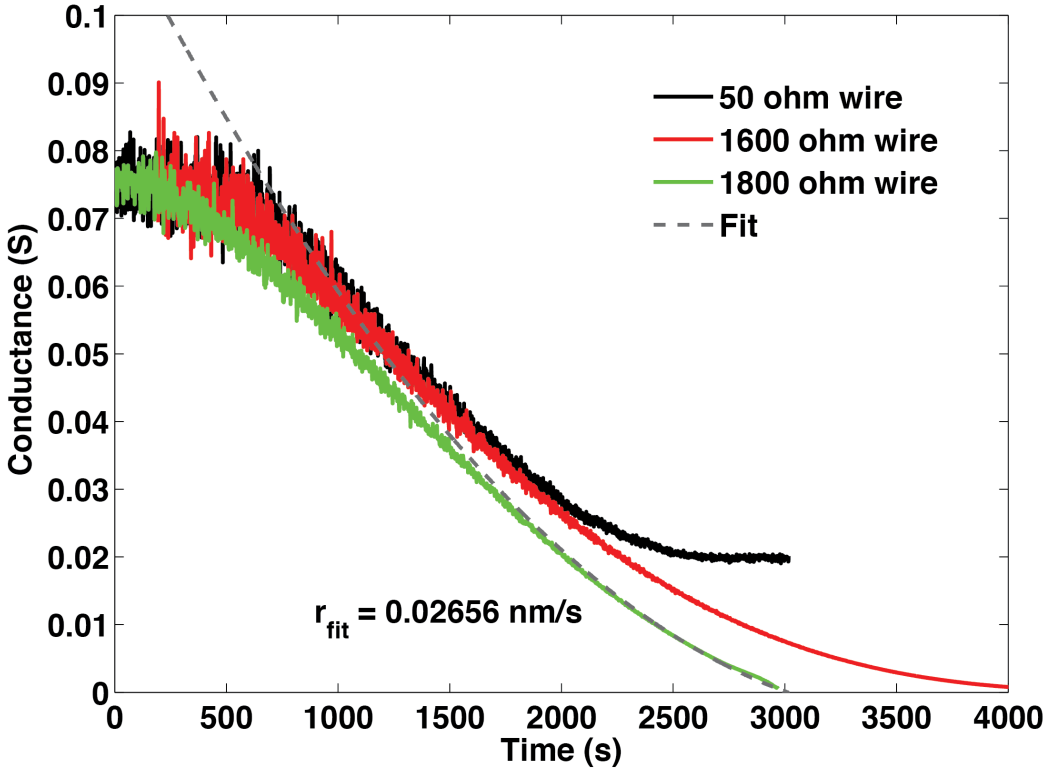

Figure 5.3: Conductance as a function of time for etched wires. The conductance curves follow a decreasing parabola as the wires etch according to the model used. The fit for the green data is shown here, with r_{fit} as the rate. The difference between the data and the model at the onset of etching is due to the thin oxide layer already present on aluminum, which the solution must etch through first before changing the conductance.

was stopped by abruptly blowing the solution off (shown in red in Fig. 5.2). After the etching solution was removed, the resistance of the nanowire remained constant at 1600Ω. The third nanowire (shown in black in Fig. 5.2) was etched until the resistance reached 50Ω, at which point the droplet of the etching solution was allowed to gradually slide off the sample. The resistance also remained firmly at 50Ω, as shown in the inset of Fig. 5.2. The minimum size (and thus maximum resistance) of a nanowire made by this technique is controlled by the initial dimensions of the wire. Nanowires with an initial width-to-thickness ratio of 2:1 are found to retain that ratio as they are etched, while nanowires with other width-to thickness ratios are etched entirely through the smallest dimension first.

5.5 Etching model

Assuming that the nanowires are uniform enough that the resistivity is constant, we construct a simple model to describe the etching process. Since the dimensions of the nanowire are changing as a function of time, the resistance of the nanowire will be determined by the changes in its thickness and the width in the following way:

$$R_{\text{wire}}(t) = \frac{\rho L}{(W - 2rt)(T - rt)} \tag{5.1}$$

here ρ is the resistivity of aluminum, L is the length of the nanowire, T is the thickness, W is the width, r is the etching rate and t is time. This model assumes that the

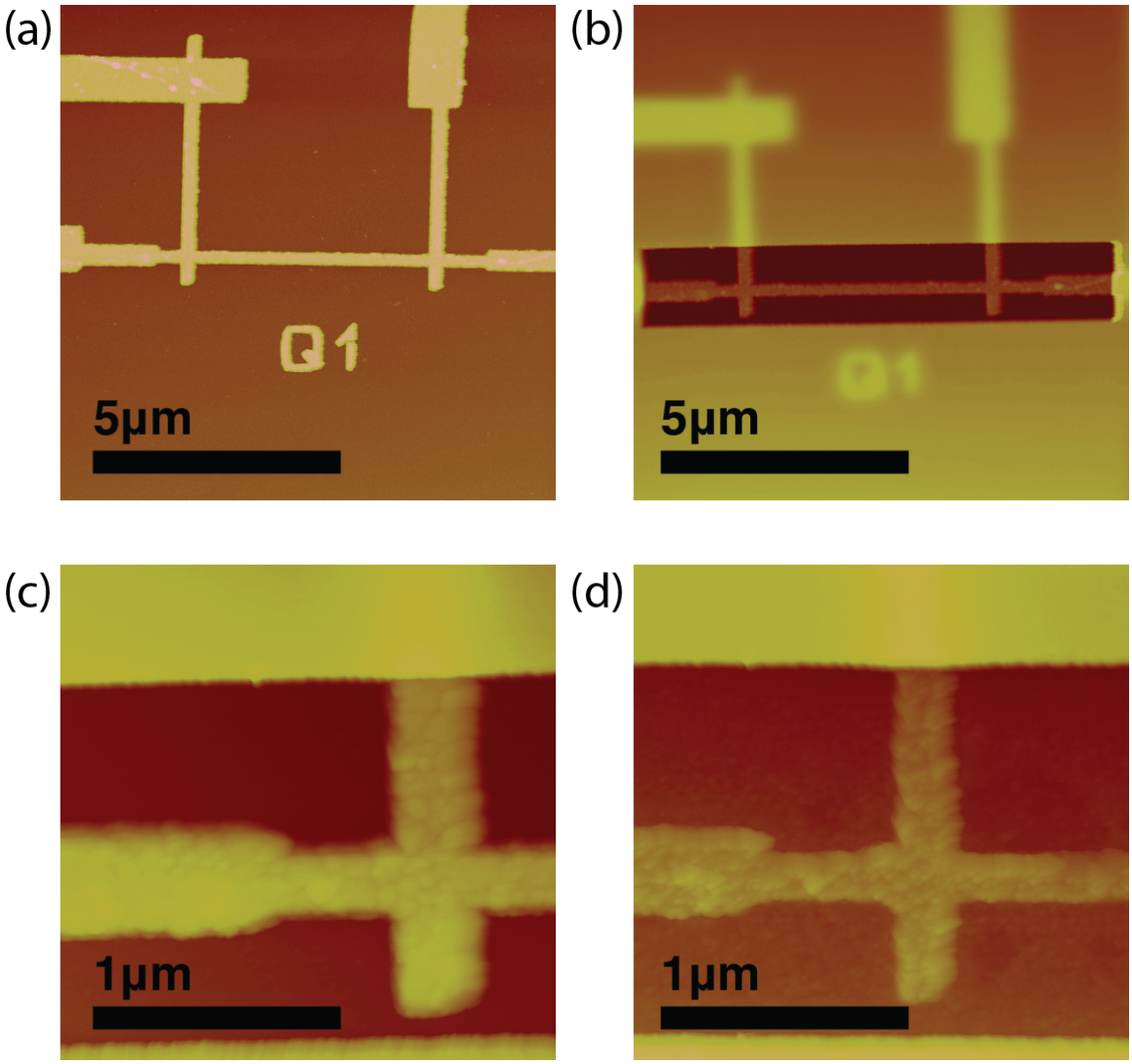

Figure 5.4: (a) Atomic force microscope (AFM) image of an aluminum wire before the PMMA mask is placed on top. (b) AFM image with the PMMA window. (c) A close-up AFM image of a section of a nanowire before etching. (d) A close-up AFM image of the same section of the nanowire shown in (c) after etching for 600 seconds. Note that the nanowire is both thinner and narrower, and the measured dimensions agree with the etching rate extracted from the resistance measurements.

nanowire has a rectangular cross-section and that the etching rate is the same on each face. The width (W) decreases at twice the rate as the thickness (T), because the nanowire is etched from both sides and from the top, but not from the bottom.

Using the measured values for L, T and W, and the resistivity for bulk aluminum, the etching rate can be treated as a fitting parameter and extracted from the data in Fig. 5.2. The fits to the resistance as a function of temperature and the corresponding etching rates are shown in Fig. 5.2. In order to account for slight variations in the width due to the resolution limits of our lithography, we introduced a second fitting parameter for the width. This parameter turned out to be of order one, which means the starting width of the nanowire was close to the intended design. The etching rates were found to be in the range of 0.01-0.03 nm/s for the chosen concentrations of sodium bicarbonate in the etching solution. The etching rate can be controlled by adjusting the concentration of the sodium bicarbonate in the etching solution - a lower pH factor resulted in a slower etching rate. The etching rate was also somewhat sensitive to the ambient temperature, and could be increased by placing the sample under a heat lamp (the results shown in Fig. 5.2. were obtained at the ambient temperature of 25°C).

The etching rate and the uniformity of the etched nanowires is further confirmed by atomic force microscopy (AFM). An AFM image of a nanowire before etching is shown in Fig. 5.4.a (illustrated in the schematic in Fig. 5.7.a), and Fig. 5.4.b. shows a nanowire with the PMMA mask on top (as illustrated in Fig. 5.1.b). A

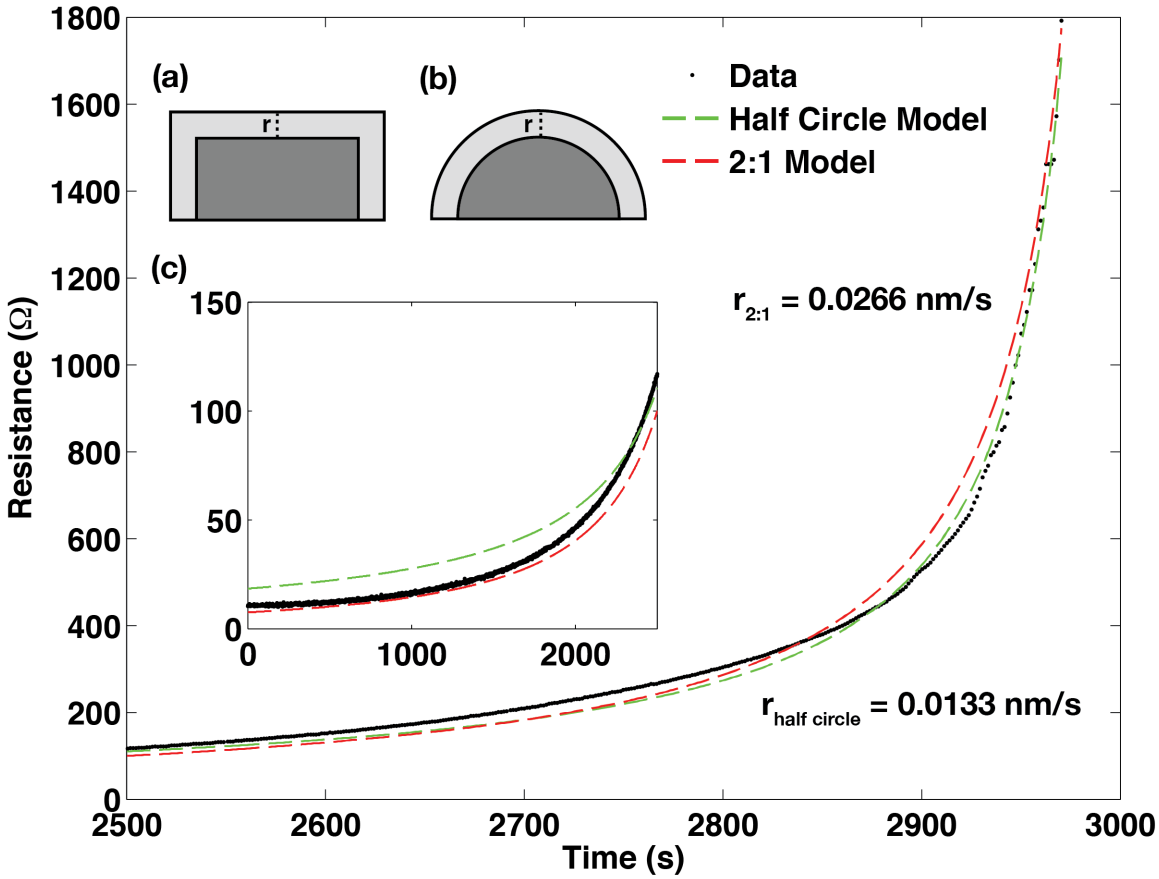

Figure 5.5: A graph of two separate models for fitting the resistance vs etching time data. The 2:1 model (red) is what was discussed in the body, and other model (green) treats the wire as a half-circle etching uniformly. The half-circle model better accounts for the loss of sharpness in the corners during the end of the etching session, but the difference between the two models shrinks as the wire shrinks. Insets: (a) Cross-section of the 2:1 model discussed in the main body, with r as the rate. (b) Cross-section of half-circle model, with r as the rate. (c) Etching data and models from 0 to 2500 seconds. The half-circle model starts with a radius of 80 nm (the height of the sample), which gives it an initial area smaller than the 2:1 model (and thus a higher initial resistance). The amount of area to be etched is thus lower, which results in a lower overall rate compared to the 2:1 model.

close-up of a section of a nanowire is shown before etching (Fig. 5.4.c) and after etching (Fig. 5.4.d). It is evident that the wire is both thinner (indicated by the darker color on the image) and narrower. The etching rate can be determined from the height measurements, and it is consistent with the etching rates extracted from the resistance measurements.

5.6 Low temperature transport properties

Superconducting properties of the etched nanowires were measured down to 250mK in a He3 cryostat (see Chapter 4 for details). Resistance as a function of temperature for an etched nanowire with a normal state resistance R_N=400Ω and two lithographically produced nanowires with R_N=80Ω and R_N=180Ω is shown in Fig. 5.6. a. The etched nanowire undergoes the superconducting transition around 1.4K, at a similar temperature as the lithographically produced nanowires (additional transition at 1.2K is closer to the bulk transition temperature for aluminum, and it is due to a small unetched section between the voltage leads on that particular sample). The smoothness of the transition further confirms that the nanowire is fairly uniform, without large variations in width and thickness. In order to compare the transition widths for the three nanowires, we show their normalized resistance as a function of temperature in Fig. 5.6.b. The etched nanowire exhibits a slightly broader transition,

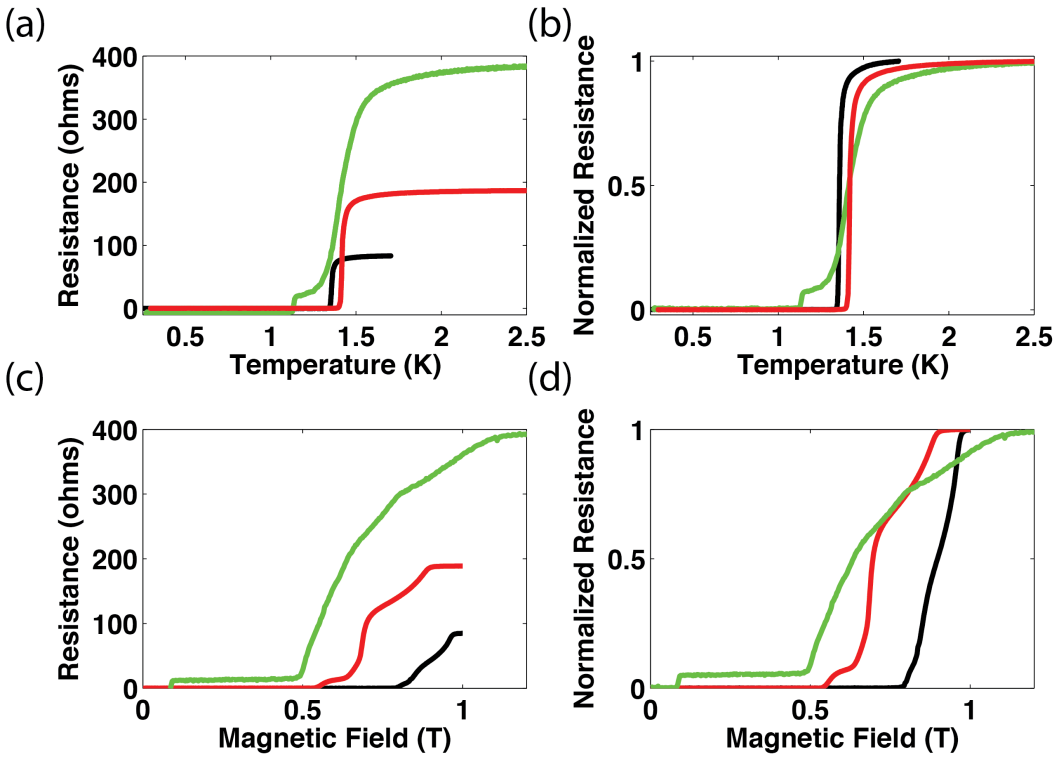

Figure 5.6: (a) Resistance as a function of temperature of a nanowire (with R_N=400Ω) produced using the etching method, compared with two nanowires (R_N=80Ω and R_N=180Ω) produced using electron beam lithography. (b) Normalized resistance as a function of temperature for the same nanowires. The etched nanowire has a wider transition than the lithographically produced wires, which is expected for a nanowire with a smaller cross-section. (c) Resistance as function of magnetic field for the same nanowires. The transition broadens as the nanowire gets more resistive. (d) Normalized resistance as a function of magnetic field. The non-zero resistance at the bottom of the etched nanowire's transition occurs because this particular nanowire was etched only between the voltage leads and not over them, so the measurement includes a small non-etched section that goes through the transition at a different magnetic field.

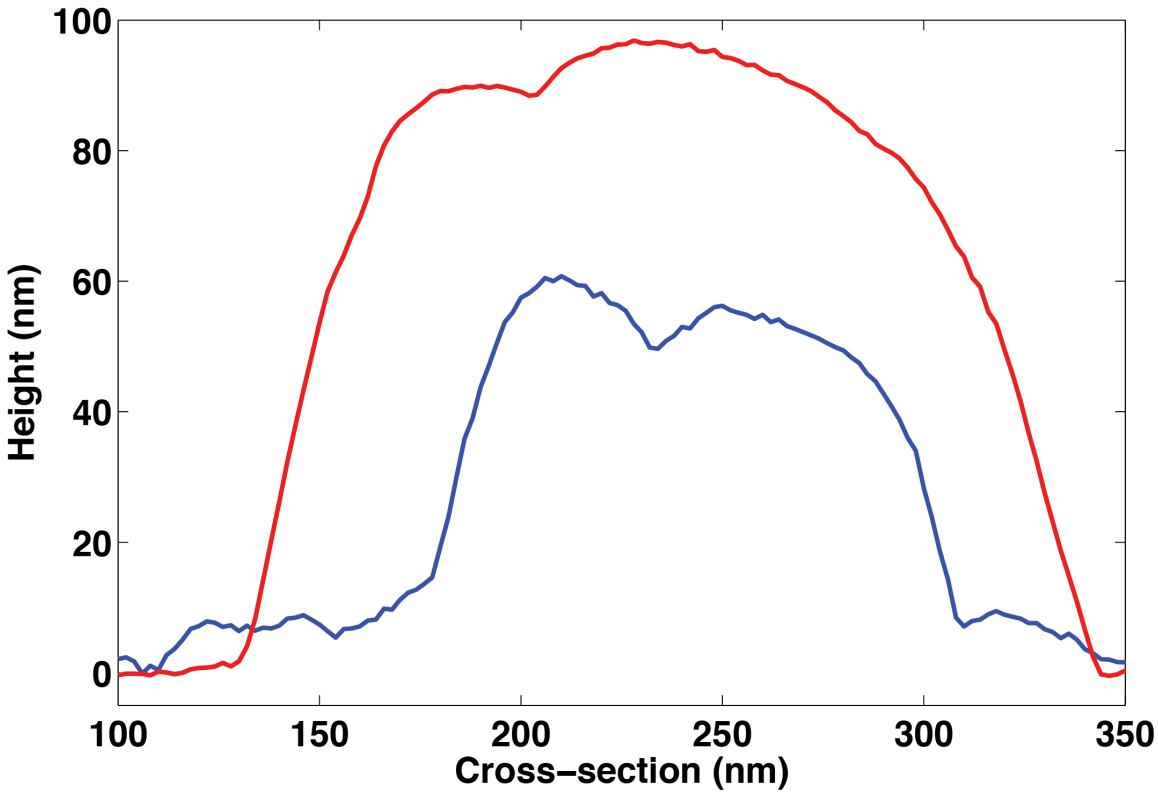

Figure 5.7: An AFM cross-section of the same area on a wire before and after etching. The slanted edges are due to convolution with the AFM tip and are not present in the actual wire.

which is typically found in nanowires that have a smaller diameter.[14] Resistance as a function of magnetic field is shown in Fig. 5.6.c., with the normalized resistance shown in Fig. 5.6.d. The transition to the normal state for the etched nanowire occurs at a slightly lower magnetic field, and the transition is broader and smoother than the transitions of the lithographically defined nanowires. Both the temperature and the magnetic field dependence of the resistance are consistent with the AFM images, which show that the etched nanowire is uniform and has a smaller cross section than the lithographically defined nanowires.

The controlled etching method allows for creating uniform aluminum nanowires with a precise geometry and the normal state resistance, but it is not limited to making nanowires. The geometry of the etched area is determined by the PMMA mask, which means that arbitrary areas can be etched while others are kept intact. Combined with the real-time monitoring of the resistance of the device, the slow etching allows for great control over the final sample's dimensions.

Chapter 6

Weber Blockade in Superconducting Nanowires

6.1 Introduction

Vortices in superconductors are topological excitations that carry quantized magnetic flux.[3] The shape of the vortices and the configurations in which they can exist in a superconductor are strongly affected by the dimensions and the geometry of the sample.[3,33–42] In thin films, in which the penetration depth λ is larger than the film thickness d, vortices are of the Pearl type,[33] and are shaped like pancakes. As the width of the film is reduced, vortices in narrow strips arrange themselves in rows.[37] Vortices cannot exist in nanowires that are narrower than the coherence length ξ,[15] but if the width of a nanowire is on the order of a few ξ, vortices will be able to enter

the nanowire in a single row. If the nanowire is also short enough that the energy difference between the states containing different number of vortices is significant, then an entry and an exit of a single vortex might be visible in transport measurements.[38,40–42] Using charge-vortex duality,[43] nanowires may exhibit Weber blockade for vortices,[38] analogous to Coulomb blockade for electrons in quantum dots.[44]

6.2 Coulomb Blockade

When nano-devices become small enough, their transport properties begin to deviate from the classical description of their behavior. This is because the low-dimensional nature of the devices means the transport properties can be determined by individual charge carriers. These charge carriers are inherently quantum mechanical entities, so our device's properties become quantum mechanical as well. This behavior is clearly seen in what is called Coulomb Blockade, which is the "turning off and on" of the conductance as a function of the chemical potential of a quantum dot.

6.2.1 Quantum Dot

What is a quantum dot? If we model the quantum dot as a 1-D infinite quantum well and solve Schrödingers equation, it will have a wavefunction given by

$$E_n = \sqrt{\frac{2}{a}} \sin\left(\frac{n\pi x}{a}\right) \tag{6.1}$$

and energy levels

$$E_n = \frac{n^2 h^2}{8ma^2} \tag{6.2}$$

where a is the width of the well, m is the mass of the particle in the well, h is Planck's constant and n is an integer. The energy levels are discrete (given by different integers n), and are spaced inversely with the square of the width of the well.

In a real 1-D quantum dot, the potential barriers at the edges are not infinite. This changes the details of the solution, but the general features still remain and bound solutions still exist at discrete energy levels. Classically, if we have a conductor interrupted by an insulating layer (as shown in Fig 6.1.a.), current will not flow across the barrier and the conductance should be zero. However, quantum mechanics permits tunneling through short insulating barriers, so we should be able to read some value for the conductance/resistance for small insulating barriers. This resistance value will depend exponentially on thickness of the insulating film, as the probability to tunnel across a barrier decreases exponentially the as a function of the thickness of the barrier. If we designate one side of the dot as the source and the other as the drain, the conductance is determined by adding a voltage bias between the two and recording the current.

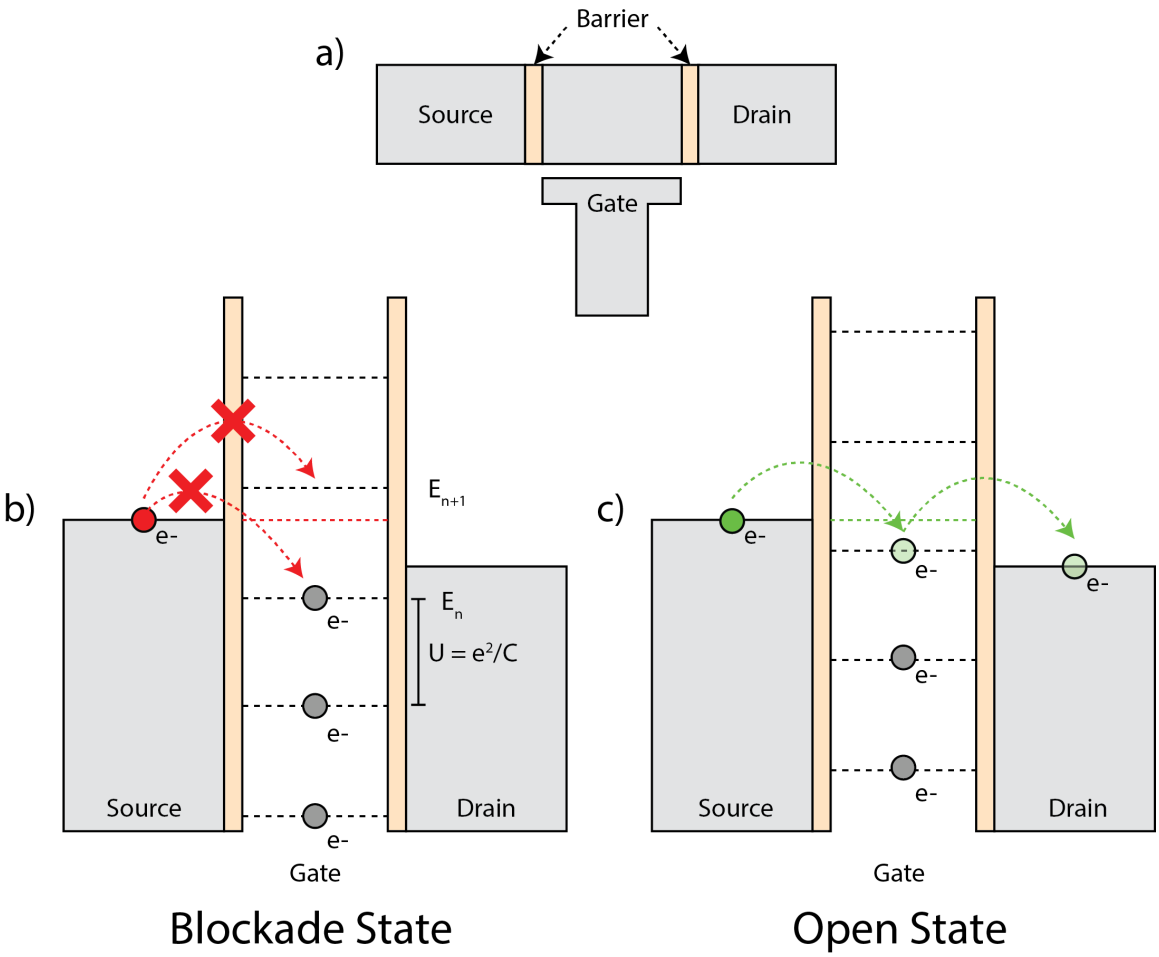

Figure 6.1: a) A schematic of a quantum dot. Here we have the dot in the center with two leads to either side, separated by a thin insulating layer. The dot is capacitively couple to a nearby gate, which can change the number of electrons on the dot. b) When the gate and source/drain bias is adjusted so there are no energy levels available to tunnel into, there is no current across the dot (ignoring second order processes). This effect is known as coulomb blockade. c) If we adjust the chemical potential so an energy level rests between the source and drain voltages, the current turns on again.

6.2.2 Coulomb Blockade

If we make the conducting "island" in the center small enough, we can describe it as a quantum dot with discrete energy levels. This discretizing is because when a single electron tunnels on to the island, the island will have a slight charge. This charge results in a repulsive force associated with trying to put another charge onto the island, and thus some discrete amount of energy

$$U = \frac{e^2}{2C} \tag{6.3}$$

(where C is the capacitance of the island) needed to overcome it. The capacitance scales with the size of the dot, so a smaller dot will have a smaller capacitance, and thus a larger energy. If the condition

$$U = \frac{e^2}{2C} >> k_B T \tag{6.4}$$

is also met, these energy levels will be thermally inaccessible to each other, and thus their discreteness should be able to be observed.

By adding charge by changing the chemical potential with respect a separate adjacent lead (henceforth referred to as the gate) the number of electrons on the island can be adjusted. This is because the relation

$$Q_{dot} = V_G C_G \tag{6.5}$$

means the charge scales linearly with the voltage.

Thus, the conductance as a function of chemical potential can be measured. Ignoring second-order processes (such as co-tunneling), the conductance of the dot will be zero unless there is an energy level accessible from an electron in the source. When an energy level drops below the source potential but is still above the drain, an electron can tunnel into the dot and tunnel out. For these values of the chemical potential, the conductance has a non-zero value. For chemical potentials where there are no energy levels in-between the source and the drain, the conductance is zero.

By mapping out the conductance as a function of both the source/drain voltage and the chemical potential, diamonds of zero conductance appear. These "Coulomb diamonds" each correspond to the addition of a single electron to the dot. See Fig.6.2 for more details.

6.3 Fabrication and measurement

The nanowires were fabricated using cold-developer electron-beam lithography.[31] A scanning electron microscope image of an aluminum nanowire and the schematic of the measurement are shown in Fig. 6.3.a. The nanowires are 25nm thick, 50-100nm wide and range from 1.5-4.5μm in length. The low temperature resistivities are on the order of $10^{-7}\Omega m$, and the residual resistance ratios are about 1.5, yielding estimates for the mean free path on the order of 1nm and the penetration depth λ around

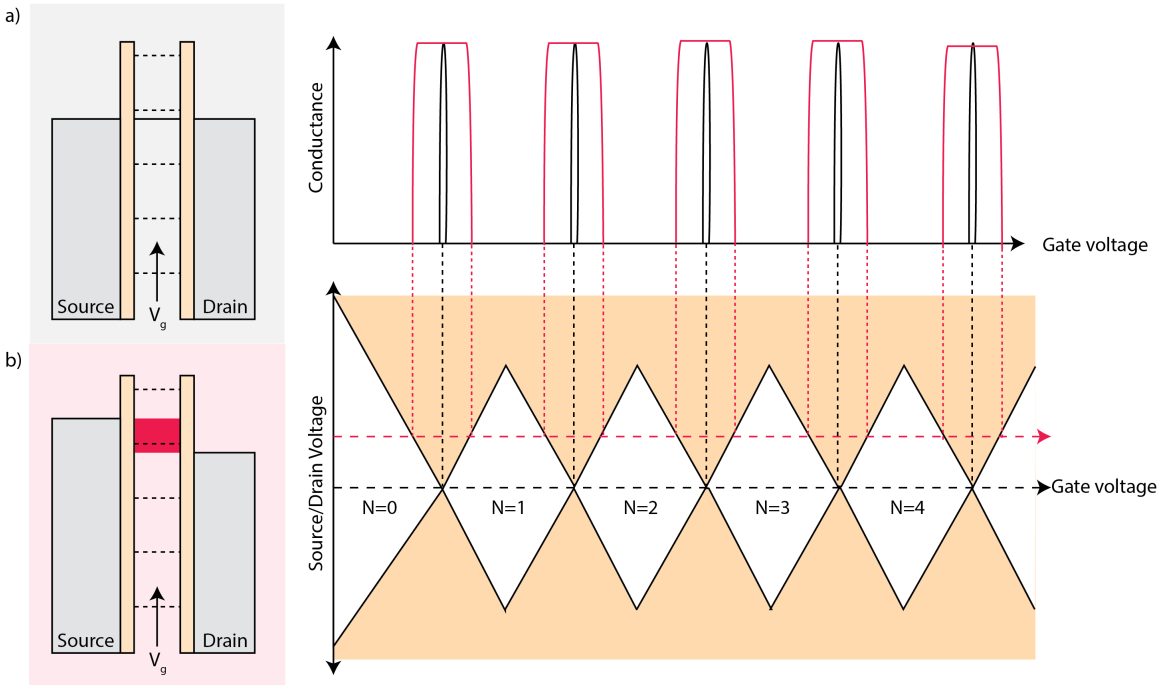

Figure 6.2: Coulomb diamonds. a) If there is no potential difference across the source and drain, current can only flow when there is an energy state equal to the two (ignoring second order processes). As the gate changes the chemical potential of the dot, there will be sharp delta-function like peaks whenever an available state passes by the source/drain potential. b) If we add a potential across the source and drain, instead of delta functions we get plateaus of resistance, as there there is now a range of gate voltages in which an energy state is available to tunnel into.

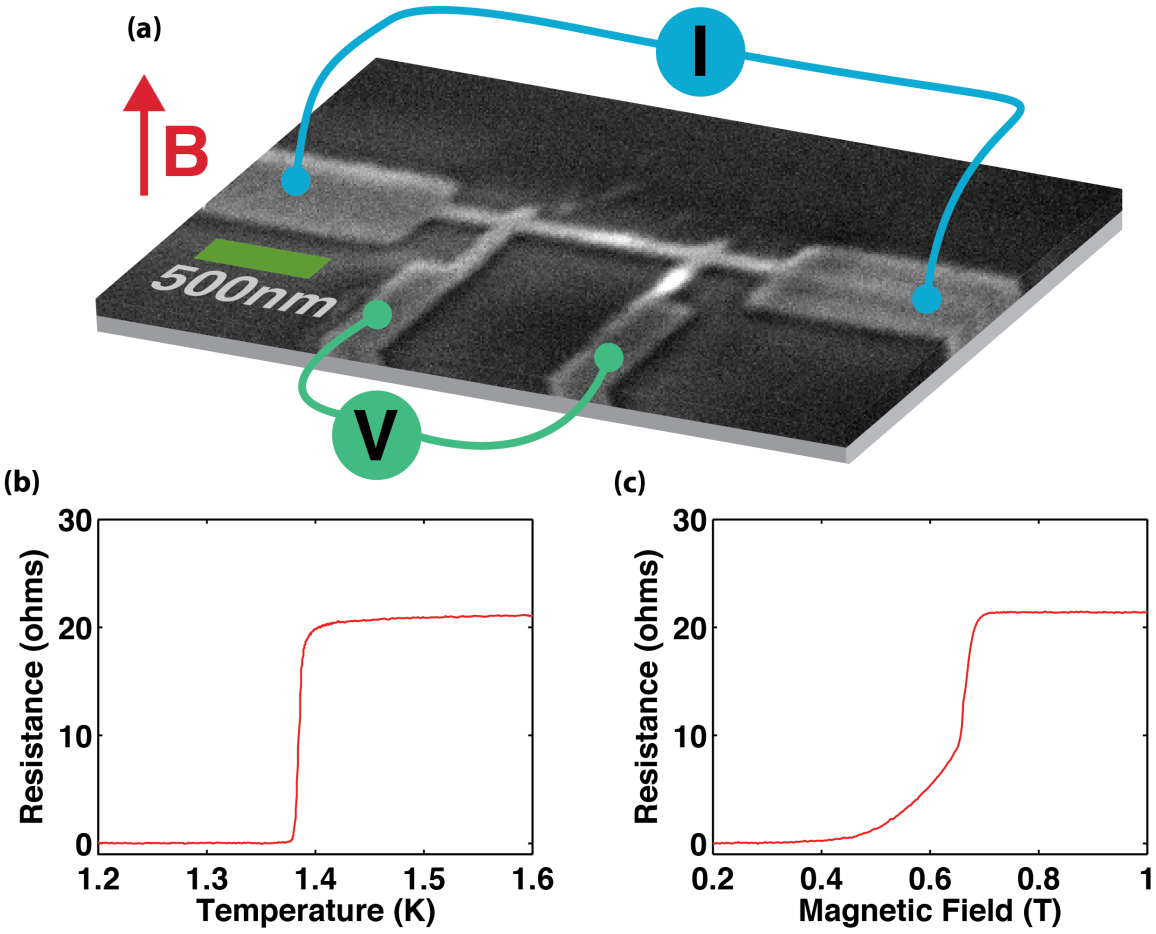

Figure 6.3: **(a)** Scanning electron microscope image of an aluminum nanowire. The scale bar is 500nm long. All nanowires are 25nm thick. The nanowire on the image is 70nm wide and 1.5μm long between the current leads (750nm between the voltage leads). The width of other measured nanowires ranges between 50nm and 100nm, and the length ranges between 1.5μm to 4.5μm as measured between the current leads. The resistance measurements are carried out in a four-probe configuration, as shown, and the magnetic field is applied in a direction perpendicular to the plane of the substrate. **(b)** Resistance as a function of temperature for one of the 1.5μm long nanowires (as shown in Fig. 6.3.a). The normal state resistance R_N is 20Ω and the T_C is 1.38K. **(c)** Resistance as a function of magnetic field for the same nanowire, measured at 250mK.

$700nm$.[3] ξ=$27nm$ was estimated from measurements of the upper critical field B_{c2} of wider strips (with a range of ξ=$15-30nm$ obtained using the slope of $B_{c2}(T)$ at T_C, shown in Fig. 6.4). As discussed below, superconductivity in our nanowires is not destroyed at B_{c2}, but at a higher field B_{C3}, as the narrow nanowires exhibit surface superconductivity at the edges.[3,45] The typical resistance as a function of temperature is shown in Fig. 6.3.b. and the resistance as a function of magnetic field is shown in Fig. 6.3.c.

The current-voltage characteristics as a function of magnetic field for a 1.5μm long nanowire at 250mK are shown in Fig 6.6.a. At low fields and low currents, the nanowire is in the superconducting state and the measured voltage is zero. When the current reaches the critical value of I_C, a sharp transition to the normal state is observed (I_C signifies the onset of non-zero resistance). The voltage is shown as a function of increasing current (hysteresis due to Joule heating[46] is shown in Fig. 6.5) . As the magnetic field is increased, I_C decreases to a lower value and begins to oscillate, as shown in a close-up in Fig. 6.6.b.

The critical current as a function of magnetic field for the same nanowire is shown in Fig. 6.6.c. After the initial drop around 60mT, oscillations in the critical current are clearly visible in the range of magnetic fields between 80-127mT. The inset in Fig. 6.6.c. shows an average over seven high-resolution magnetic field and current scans (see Fig. 6.12). There is a clear pattern in the critical current as a function of the magnetic field: apart from a few small irregularities, the critical current increases

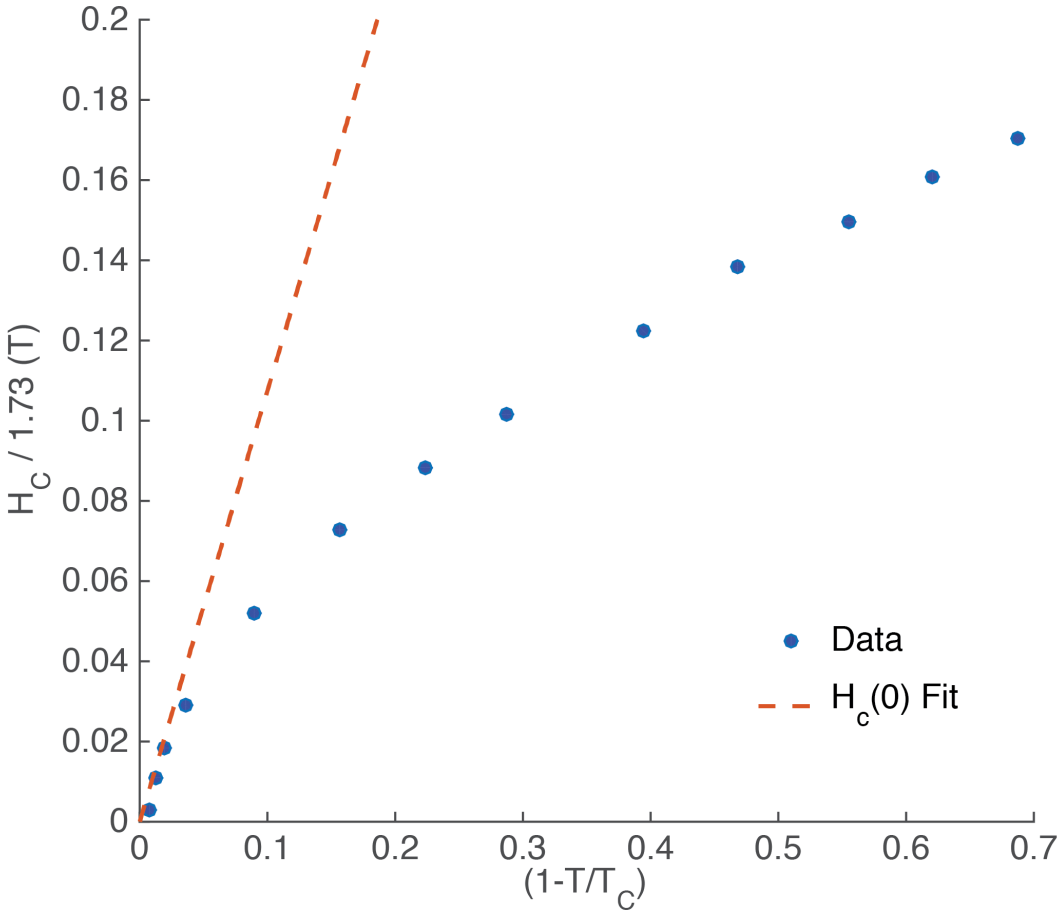

Figure 6.4: The critical field as a function of reduced temperature for a narrow superconducting strip. The dashed line represents a linear fit near T_c, the slope of which yields an estimate for the coherence length of 19nm. A reasonable fit can be obtained for 15-30nm in various samples. A direct measurement of B_{c2} at the base temperature of 250mK gives B_{c2} =0.44T, which yields an estimate of ξ=27nm by using $B_{c2} = \Phi_0/2\pi\xi^2$.

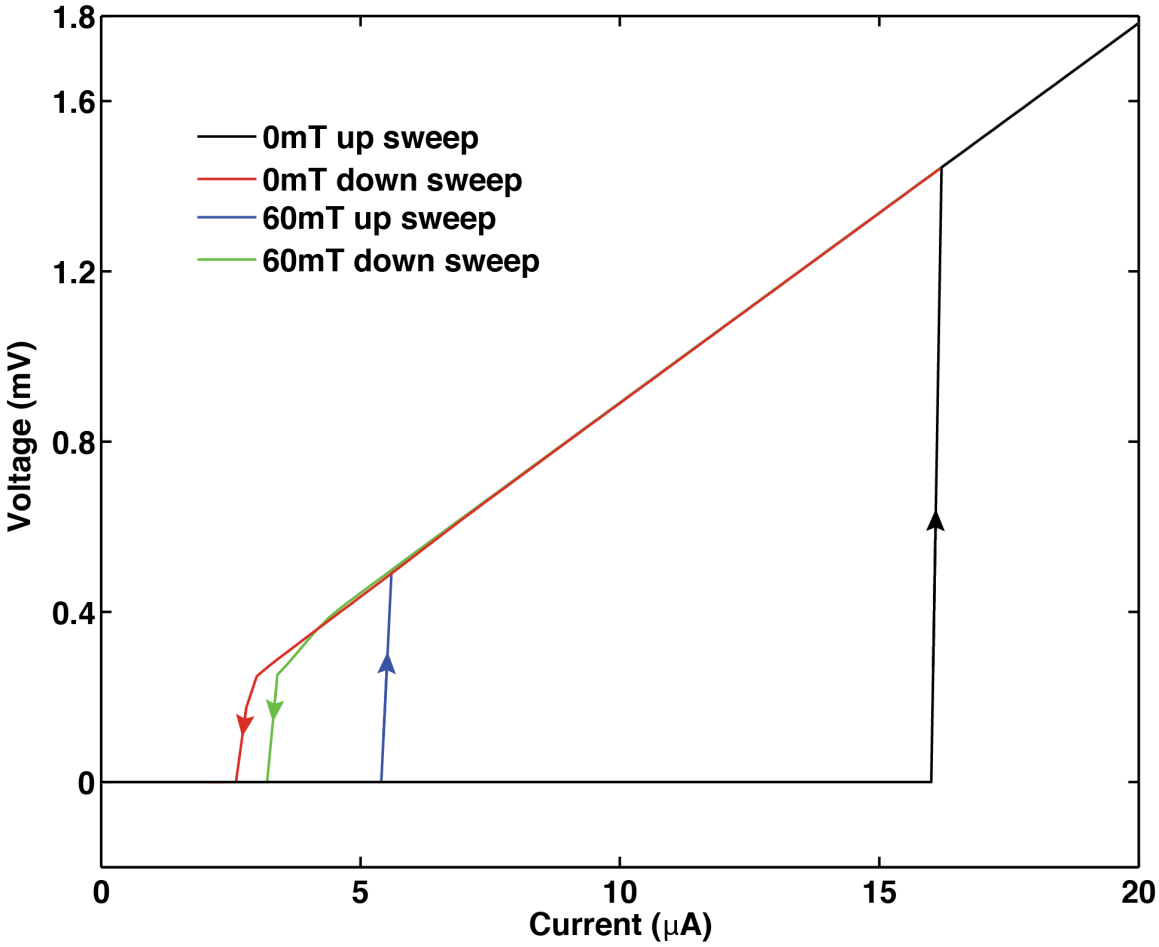

Figure 6.5: I-V measurement for a nanowire in magnetic field. As the current is increased in the superconducting wire, it remains in a superconducting state until some critical current I_c. At this point, the wire transitions into the normal state. As the current is then lowered, it does not transition to the superconducting state at the same critical current, as the wire is being heated by the Joule heating. As the current is decreased, eventually the wire transitions back into the superconducting state at some lower critical current (this is known as the "re-trapping" current). This is shown for two magnetic fields which show a different critical current but a similar re-trapping current, arising from the different origins of both.

linearly, reaches a peak, and then decreases linearly. This pattern repeats with a periodicity of about 5mT, and it stops abruptly upon reaching a peak at 127mT. Above 127mT, the critical current decreases linearly to zero.

The voltage as a function of magnetic field and the applied current is shown in Fig. 6.7.a. (data from additional samples are shown in Fig. 6.11). Fig. 6.7.b. shows a phase diagram for the nanowire and the current leads. The resistance of the current leads was measured separately in a four-probe measurement, as shown in Figs. 6.8 and 6.9. The light blue area represents the values of the currents and magnetic fields at which both the leads and the nanowire are superconducting. As the current is increased, the current leads are driven normal (see Fig 6.9), but the nanowire remains superconducting (dark blue area). Note that the nanowires have a higher T_C and a higher $I_C(0)$ than the leads.[47] The current leads are normal at the current levels at which the critical current oscillations are observed in the nanowire, and the critical current of the leads decreases monotonically with the magnetic field, with no oscillations. We found oscillations in nanowires that were up to 4.5μm long, although they were no longer strictly periodic when the length of the wire exceeded about 2μm. We have not observed any significant asymmetry for the opposite polarity of the magnetic field, nor a hysteresis in I_C with respect to the magnetic field. To highlight the oscillations in I_C, which appear to be superimposed on a background of decreasing critical current as a function of magnetic field, I also show the phase diagram as a function of current and magnetic field in Fig. 6.7.c. with the background

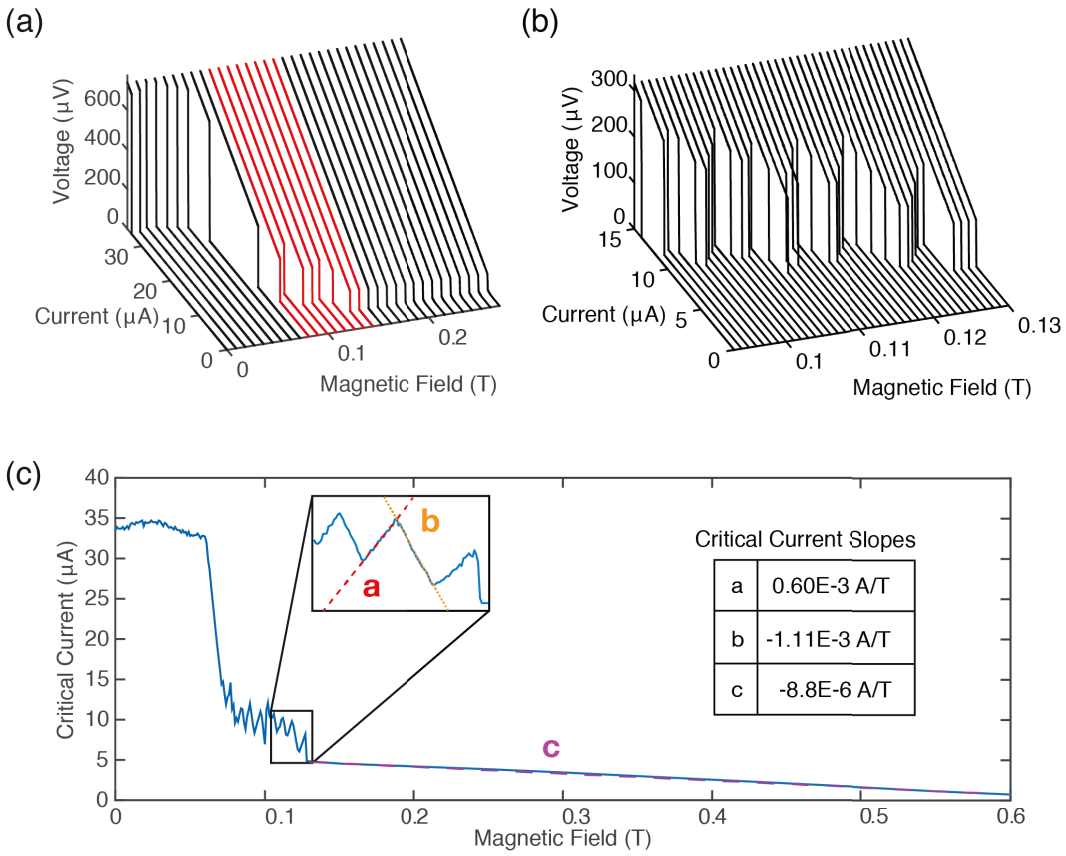

Figure 6.6: **(a)** Voltage (vertical axis) as a function of current measured at different discrete values of magnetic field from 0 to 270mT for a 1.5μm long nanowire at 250mK. Each line is a measurement of voltage as a function of applied current at a constant magnetic field. **(b)** Current-voltage characteristics in the range of magnetic fields between 90 and 130mT, where the critical current shows non-monotonic behavior as a function of magnetic field. **(c)** Critical current as a function of magnetic field for a 1.5μm long wire at 250mK. The inset shows an average over seven high-resolution magnetic field and current scans. The average slopes of three linear regions are listed in the inset.

subtracted.

6.4 Analysis

As I argue below, the observed critical current oscillations can be understood in terms of discrete entry and exit of single vortices in the nanowire. The appearance of vortices in thin films of superconductors has been studied extensively, both theoretically[37,48–57] and experimentally.[34,58–60] In order to understand the observed oscillations of the critical current in magnetic field, we have to consider the characteristic dimensions of our samples. In thin and narrow strips, where both the thickness and the width are of the order of ξ, the finite size of the vortex core cannot be ignored and one should use the Ginzburg-Landau model,[50,51,53,56] rather than the London theory. Within the Ginzburg-Landau model, it has been argued that vortices can enter a thin film strip if its width is at least 1.8ξ.[37] Assuming that the coherence length in our samples is about ξ=27nm, the width of our samples (50-100nm) is just large enough to allow entry of a single row of vortices.

In general terms, the stability of vortices in a superconducting strip is governed by their potential energy, which varies across the width of the strip. The potential

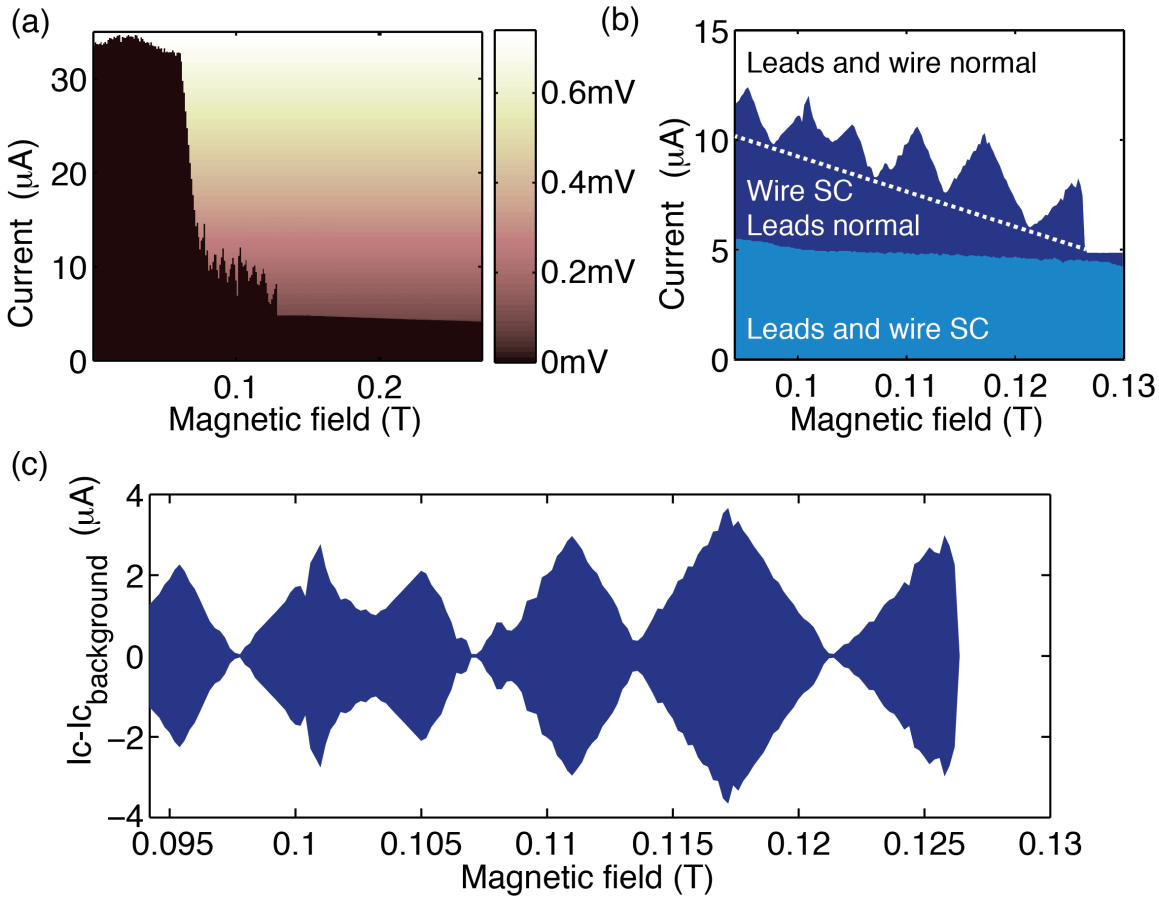

Figure 6.7: **(a)** A color plot of the voltage as a function of magnetic field and current at 250mK. The black area is superconducting, and the voltage there is zero.**(b)** A phase diagram as a function of magnetic field and current at 250mK. The boundary between the dark blue and the white region is extracted from seven high-resolution magnetic field sweeps (shown in Fig. 6.12). **(c)** The phase diagram as a function of current and magnetic field for a 1.5μm long wire at 250mK in the oscillating regime, with the linear background (shown as a white dashed line in Fig 6.7.b.) subtracted. The slope of the subtracted portion was chosen to run along the dips of the oscillations and is somewhat arbitrary - it is not meant to be quantitative, but rather intended to highlight the oscillations only. As argued in the main text, this is also an attempt to separate the vortex degrees of freedom (linear increase and decrease of critical current) from the effects of suppressing the superconductivity in the bulk of the wire (approximated as a linear decrease in the range of magnetic fields in which the oscillations are observed). The resistance is zero inside the diamond-shaped regions (blue).

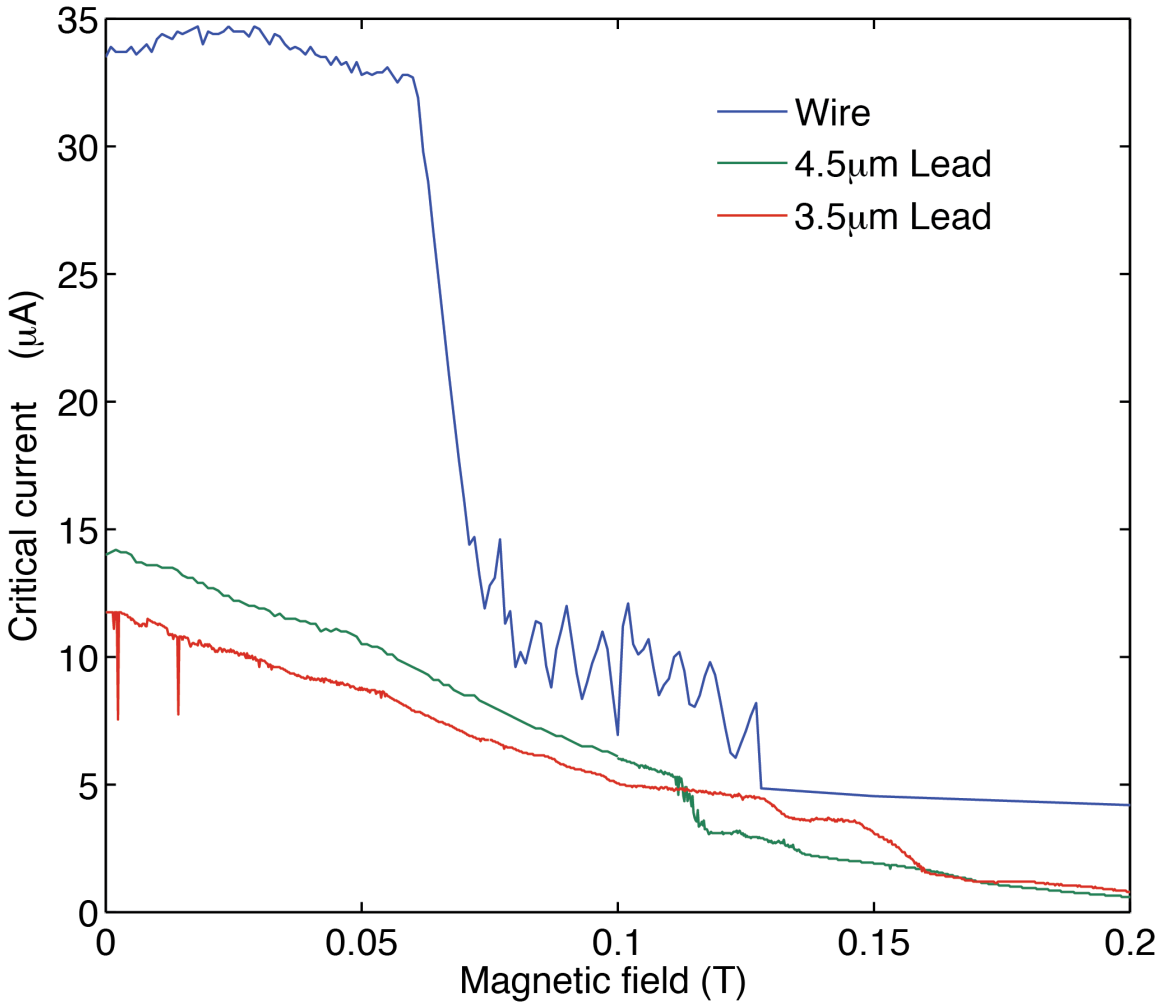

Figure 6.8: Critical current as a function of magnetic field at 250mK for a 1.5μm long and 70nm wide nanowire (blue), and two leads: both leads are 400nm wide, but one is 4.5μm long (green) and the other is 3.5μm long (red). It is clear that the leads undergo a transition into the normal state at lower current values than the nanowire. This shows that the leads are in the resistive state at the current levels at which the oscillations are observed in the nanowire. Although some non-monotonic features are visible in the critical current of the leads, these features do not seem to be related to the oscillations in the wire in any obvious way and there are no clear oscillations in the leads themselves.

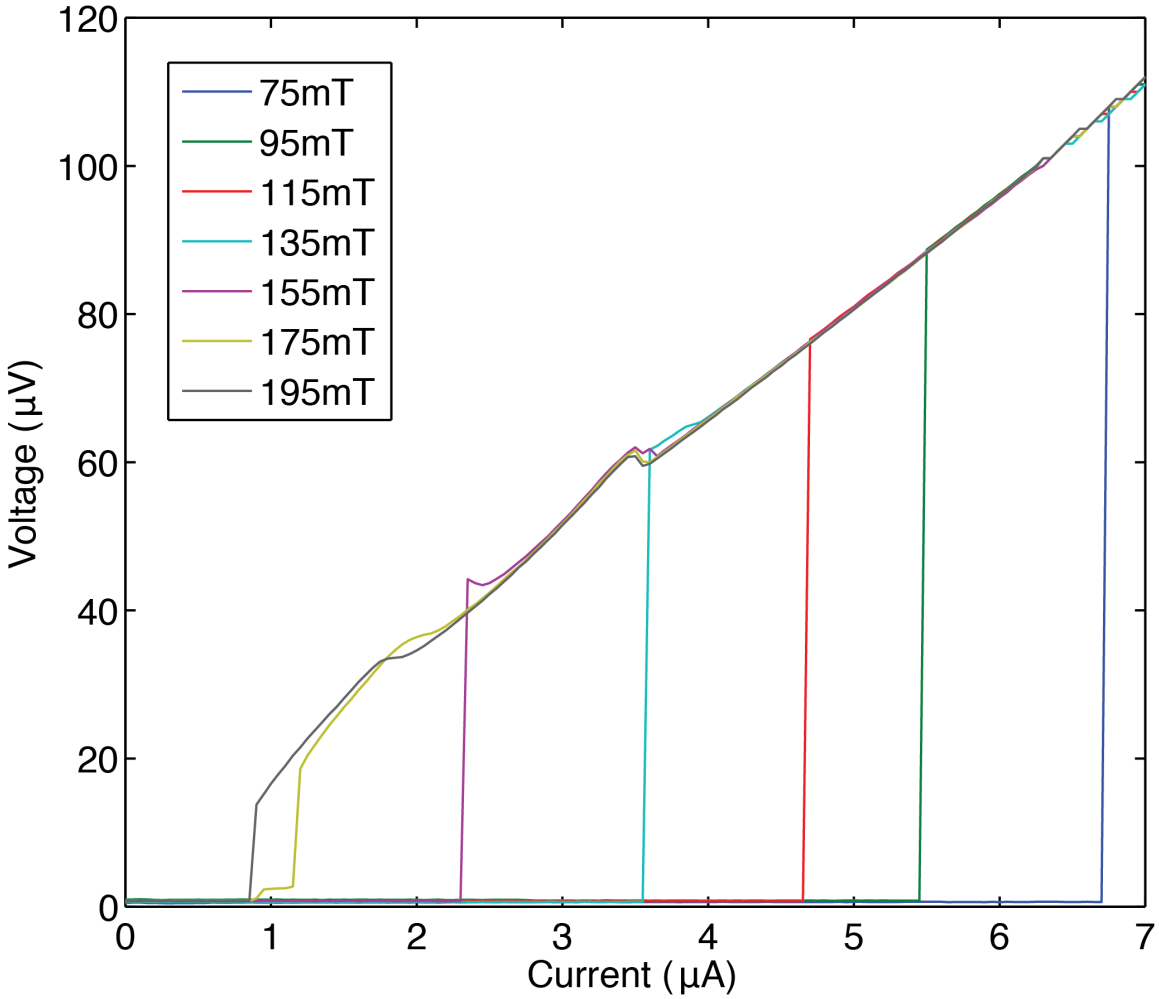

Figure 6.9: Current-voltage characteristics measured on one of the current leads (not the nanowire) in a four-probe configuration. The lead is 400nm wide, 3.5μm long and 25nm thick. The current is ramped from zero to 7μA in all cases. The temperature is 250mK.

energy of a single vortex in the nanowire can be written as follows:[38,48,50,51,61]

$$E = 2\pi\rho \ln \frac{\sin \pi y/w}{\sin \pi \xi/w} + \frac{4\pi^2 \rho B}{\Phi_0}\Big[\big(y - \frac{w}{2}\big)^2 - ... \\ \big(\xi - \frac{w}{2}\big)^2\Big] + \frac{\Phi_0 J}{w}\big(y - \frac{w}{2}\big) \tag{6.6}$$

where y is the coordinate across the width of the wire, w is the width, B is the magnetic field, J is the current density, ρ is the superfluidic stiffness, ξ is the coherence length, and Φ_0 is the flux quantum. The first term is a contribution from the vortex image interaction, where the divergence at the edges is cut off by the finite size of the vortices. The second term arises from the interaction energy between the vortex and the applied magnetic field - this term is responsible for creating a potential well for vortices in the center of the nanowire. The two terms in the square parentheses come from integrating over the distance near the edges in which the current is non-zero,[50] which is on the order of $\frac{w}{2} - \xi$, assuming that we only have one vortex in the center of the wire. The third term is the potential from the force that arises from the interaction between the vortex and the applied current - this term tilts the potential towards one edge of the nanowire. The potential energy of a vortex is shown in Fig. 6.10.a. At low magnetic fields, the potential energy is positive everywhere, and the vortices cannot enter the sample. As the magnetic field is increased to B_0, the potential energy develops a local minimum in the center of the nanowire, but it remains positive everywhere. Upon further increase of the magnetic field to B_S, the potential energy reaches zero in the center of the strip, and becomes negative

in higher fields. Above B_S, the vortices can exist in the film in a stable state,[48] but potential barriers at the edges[49,55,59,62] will impede the entry of vortices until a higher magnetic field B_E is reached, at which the potential barriers at the edges disappear. For large enough currents, both barriers disappear, as shown in Fig. 6.10.b.

Since the vortices need to both enter and exit the nanowire for the resistance to appear, we expect the larger of the two barriers to determine I_C. For a fixed number of vortices in the nanowire, the increasing magnetic field will cause the exit barrier to increase and the entry barrier to decrease, until another vortex can enter the nanowire.[37] If the nanowires are shorter than 100 ξ, this may manifest as oscillations in the critical current.[37] The periodicity observed in shorter nanowires corresponds to $\Phi_0/2\pi$Lw (L is the length and w is the width).

In the regime in which vortices can enter the nanowire, the critical current is determined by the sum of the applied current, vortex current and the screening currents generated in the superconducting regions. After the first vortex enters the nanowire, an increasing magnetic field will generate screening currents in order to expel additional flux. In this regime, the exit barrier is lower than the entry barrier, and the critical current is determined by the entry barrier. The entry barrier decreases with magnetic field,[37] causing a decrease in the critical current, $I_C \propto w^2(B_S - B)/4\pi\lambda$.[50] This continues until the additional flux reaches one half of a flux quantum - the entry barrier now becomes lower than the exit barrier, so the onset of resistance is determined by the exit barrier,[37] causing an increase in the critical current, $I_C \propto w^2 B/4\pi\lambda$,[50] in

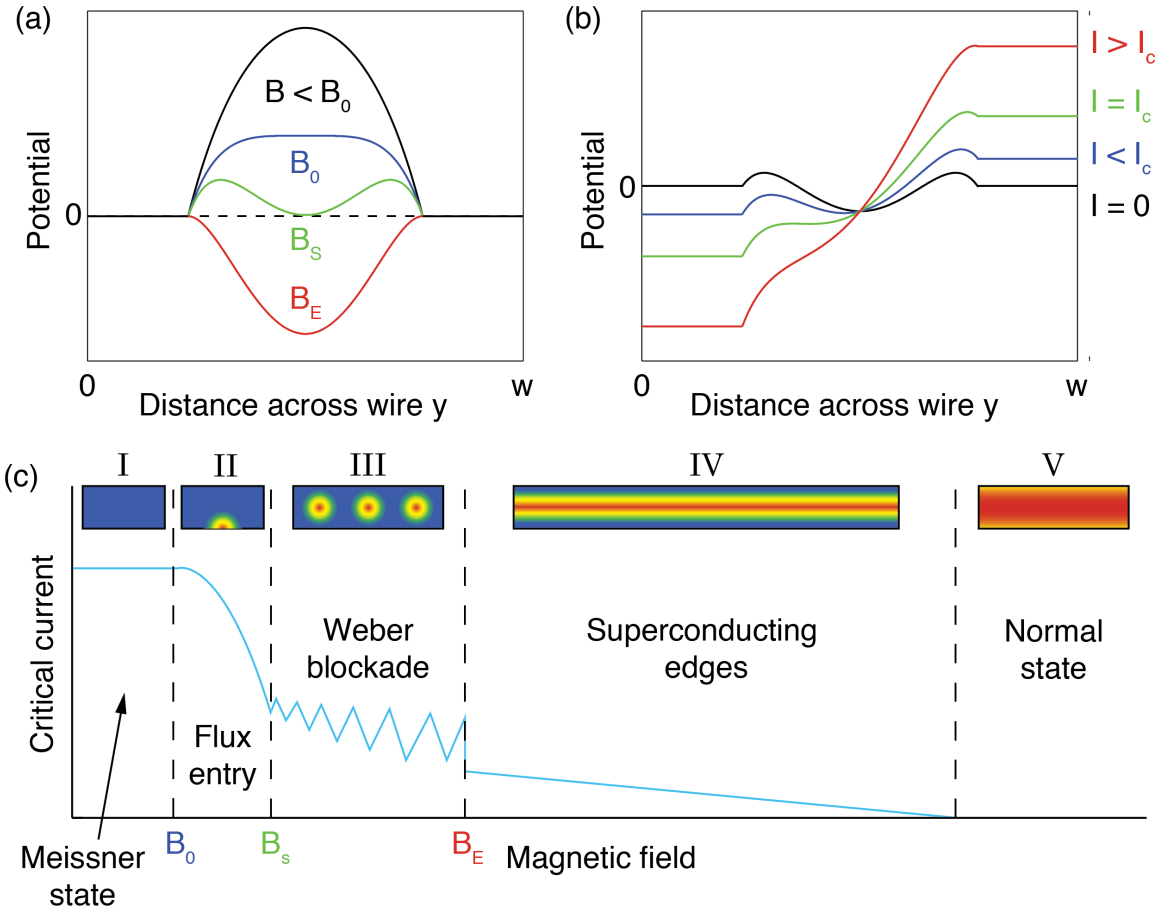

Figure 6.10: **(a)** Potential energy of a vortex as a function of its position across the width of the wire for different magnetic fields, with no applied current. At B_0, the potential develops a minimum which reaches zero at B_S. B_E is the field at which the potential barriers at the edges disappear. **(b)** Potential energy of a vortex as a function of its position along the width of the wire for different applied currents in a magnetic field between B_0 and B_S. **(c)** A schematic of different vortex regimes in the nanowire as a function of current and magnetic field. The blue color denotes the superconducting regions and the red color corresponds to the normal regions.

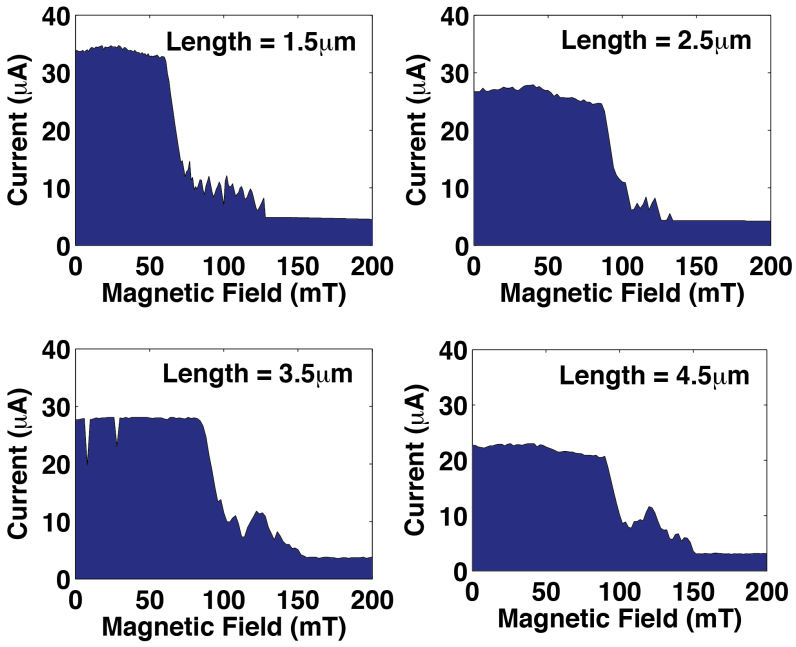

Figure 6.11: Phase diagram as a function of current and magnetic fields for four wires of different length at 250mK. The dark areas represent zero voltage, while the white areas represent the resistive state (the voltage scale is shown in Fig. 6.6). While critical current oscillations are present in all the nanowires, they cease to be periodic as the length of the nanowire increases close to and above 100ξ (b, c and d).

agreement with the observed linear slopes in Fig. 6.7.c. The cycles repeat until the vortices begin to overlap, and the oscillations stop abruptly at the last local maximum in I_C.

The full phase diagram is shown in Fig. 6.10.c. Because the width of our nanowires is on the order of ξ (and much smaller than λ), they behave like thin films in a parallel field[3] and I_C is only weakly affected at low fields (region I). At higer fields, I_C starts to decrease (region II). Once the vortices can enter the nanowire, they are arranged in a single row (region III).[37] As the magnetic field is increased further, the potential barriers at the edges decrease, the vortex row becomes denser, eventually merging into a normal channel in the center of the strip (region IV).[39,53] Region IV shows a slow linear decrease in I_C until the magnetic field is large enough to destroy the surface superconductivity at the edges[3,39,45] and the sample enters the normal state (region V).

An equivalent description of the Weber blockade regime in Region III can be obtained by considering only the vortex degrees of freedom. Using the vortex-charge duality, our nanowire can be viewed as a vortex analog of a Coulomb-blockaded quantum dot, as seen in Fig. 6.14. The magnetic field is the analog of the gate voltage, as it tunes the number of vortices in the nanowire. The applied current is the analog of the bias voltage, as it causes the vortices to cross the nanowire. In the dual picture, zero resistance corresponds to zero conductance for vortices (as illustrated in Fig. 6.7.c.), in analogy with the Coulomb diamonds in quantum dots,

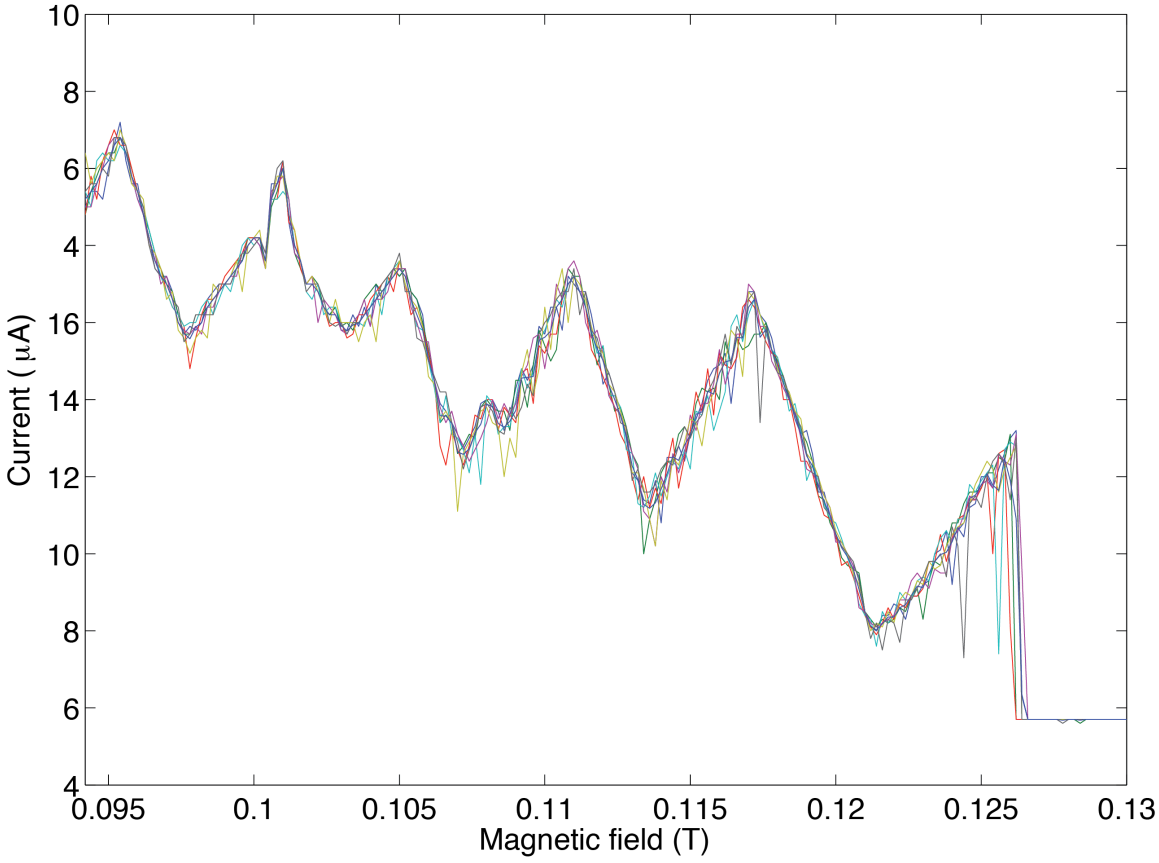

Figure 6.12: **(a)** Voltage (vertical axis) as a function of current measured at different discrete values of magnetic field from 0 to 270mT for a 1.5μm long nanowire at 250mK. Each line is a measurement of voltage as a function of applied current at a constant magnetic field. **(b)** Current-voltage characteristics in the range of magnetic fields between 90 and 130mT, where the critical current shows non-monotonic behavior as a function of magnetic field. **(c)** Critical current as a function of magnetic field for a 1.5μm long wire at 250mK. The inset shows an average over seven high-resolution magnetic field and current scans. The average slopes of three linear regions are listed in the inset.

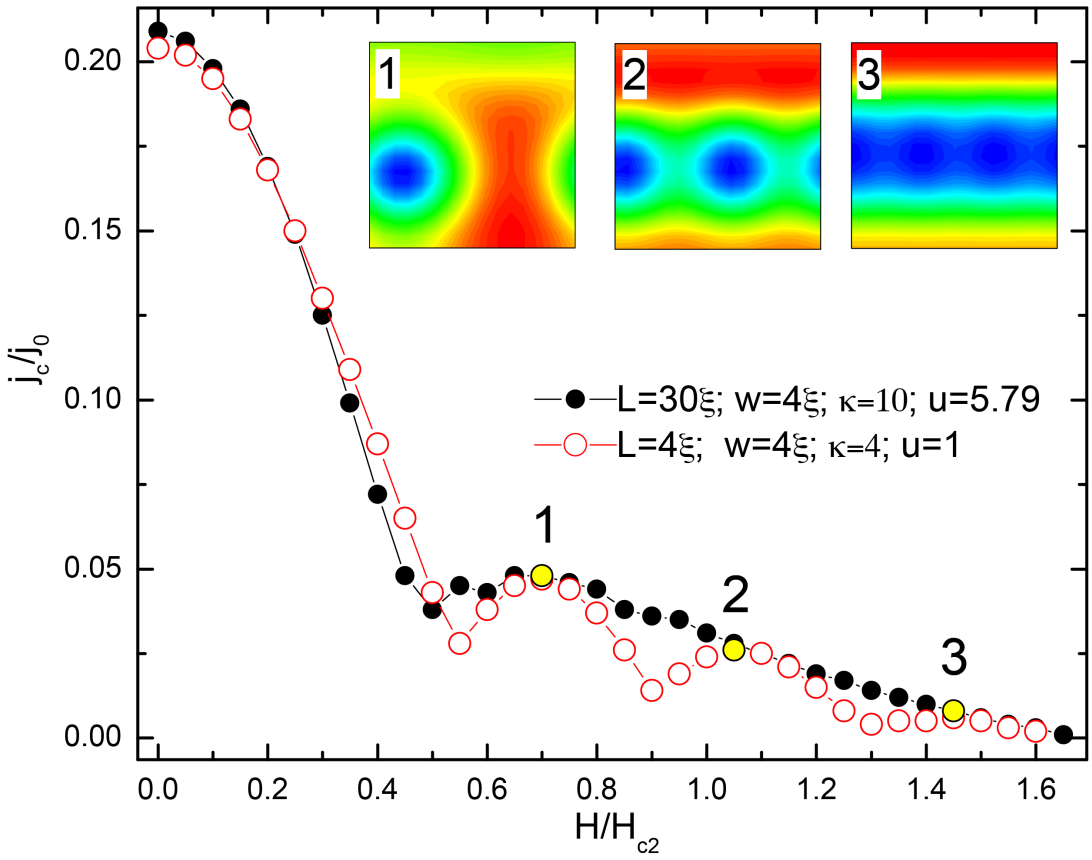

Figure 6.13: Time-dependent Ginzburg-Landau simulation of the superconducting order parameter in a thin, narrow nanowire. We see oscillations that correspond to the addition of a single flux quantum to the wire. For a longer wire, we see the individual oscillations replaced by one single bump, which we can see in our two wires above 2.5μm. Thanks for Francois Peeters and Golibjon Berdiyorov for running these simulations.

inside which the electron conductance is zero, and the number of electrons is fixed.

We conclude that the number of vortices in narrow and short superconducting nanowires can be precisely tunable by applied magnetic field, which can be used as an advantage in flux-based superconducting devices.

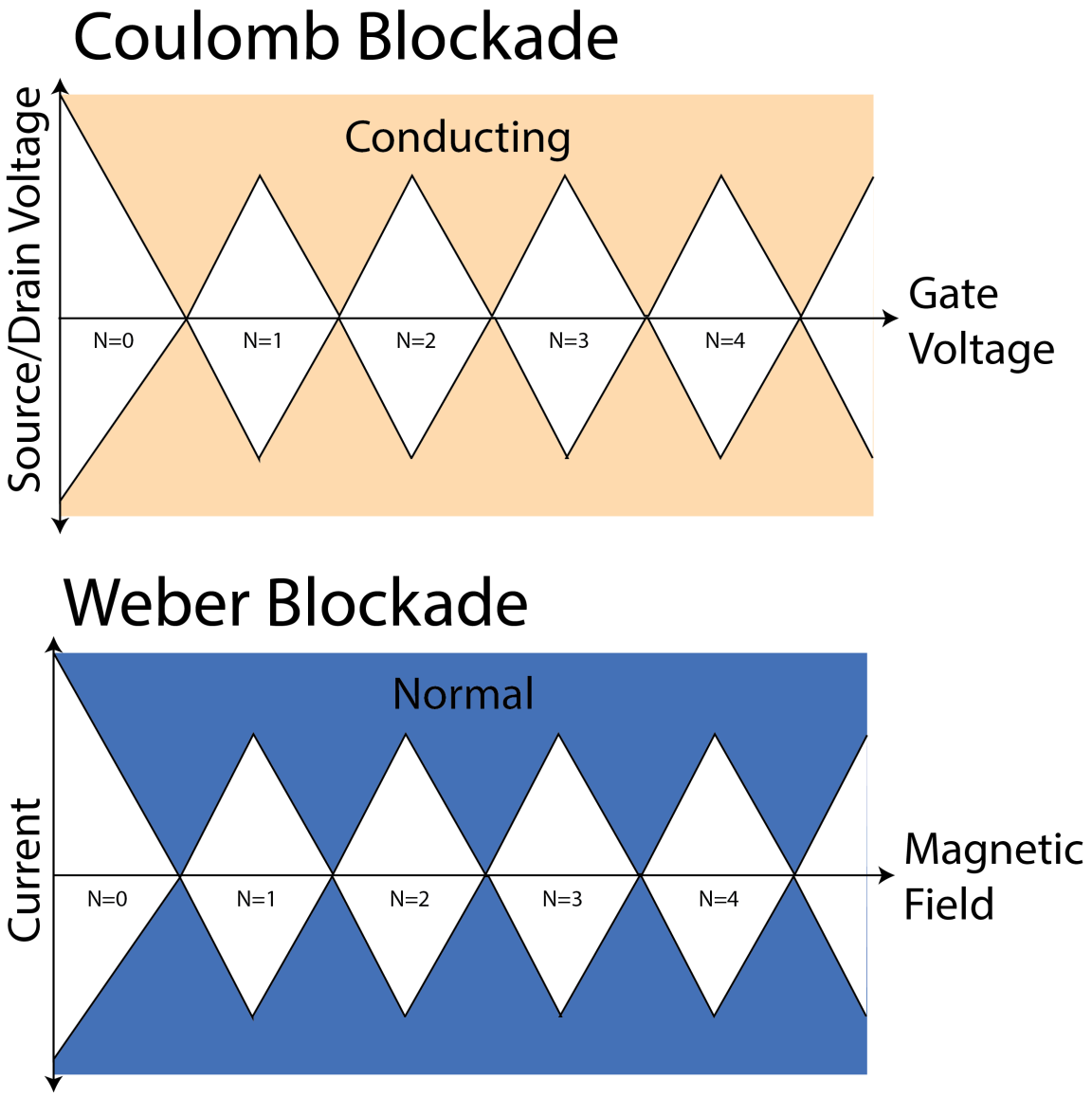

Figure 6.14: Charge-flux duality between Coulomb blockade and Weber blockade. The magnetic field is the analog of the gate voltage, as it tunes the number of vortices in the nanowire. The applied current is the analog of the bias voltage, as it causes the vortices to cross the nanowire.

Chapter 7

Vortex Transport

7.1 Flux flow

As seen in Chapter 6, we can think of a superconducting vortex as an standalone particle. It can experience force (Eqn. 2.31), move through the superconductor, (Eqn. 2.33), and it can interact with applied fields, currents, and other vortices. Indeed, charge-flux duality implies we can think of a vortex much like we would an charge carrier. We can then investigate the transport properties of vortices in a similar manner to how we investigate electron transport.

Unlike an electron, however, a vortex has no charge. How are we to investigate it with equipment meant to measure and interact with electrons? A vortex does not interact directly with an applied electric field like an electron would, however, it does interact with the current. This Lorentz force results in an vortex experiencing a force

transverse to the direction of the current and the magnetic field (see Eqn. 2.31 and section 2.4.1) for more details). This Lorentz force is the equivalent to a Magnus force experienced by a vortex in a moving flow.[63] This force moves the flux lines, and a moving magnetic field results in an electric field parallel to the current, so a voltage drop is observed. The magnitude of this voltage drop is proportional to the velocity and number of vortices moving, so we can now investigate this "current" of vortices moving perpendicular to the superconducting current.

However, there are difficulties in measuring the flow of vortices. Particularly, vortices tend to get stuck, or "pinned" to impurities and inhomogeneities in the superconductor. Indeed, this pinning force is quite strong and is the dominating factor at low currents and low fields for large samples. As the current and field is increased, the Lorentz force increases as well. When the Lorentz force exceeds the pinning force, the vortex can move and there is an onset of resistance in the device.

7.1.1 Flux flow device

Figure 7.1 shows a schematic of the device measured to investigate this phenomena. Part a) shows the sample in a perpendicular field configuration, where the field is applied perpendicular to the long axis of the wire. The current is applied from the outermost leads and read from the inner two in a four-probe configuration (See section 4.3.2). Part b) shows the zero-field resistance versus temperature data. The device undergoes a transition to a superconducting state at approximately 1.35K. Part c)

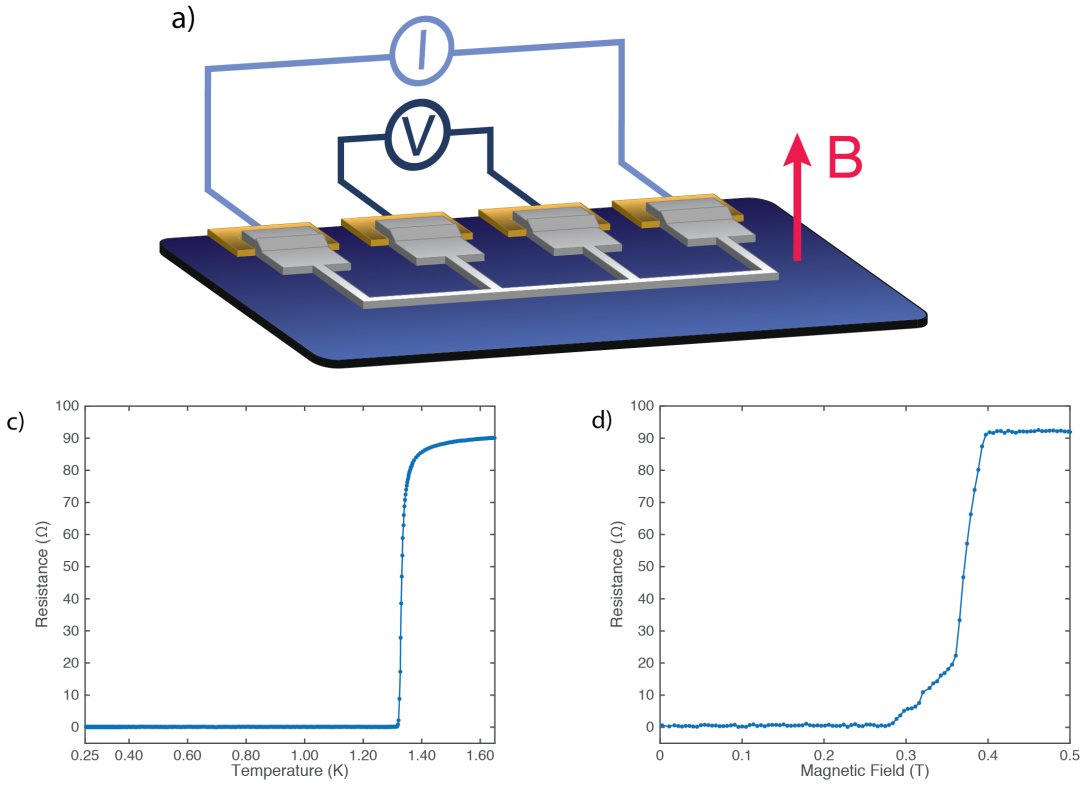

Figure 7.1: Schematic of the flux-flow device and basic transport features

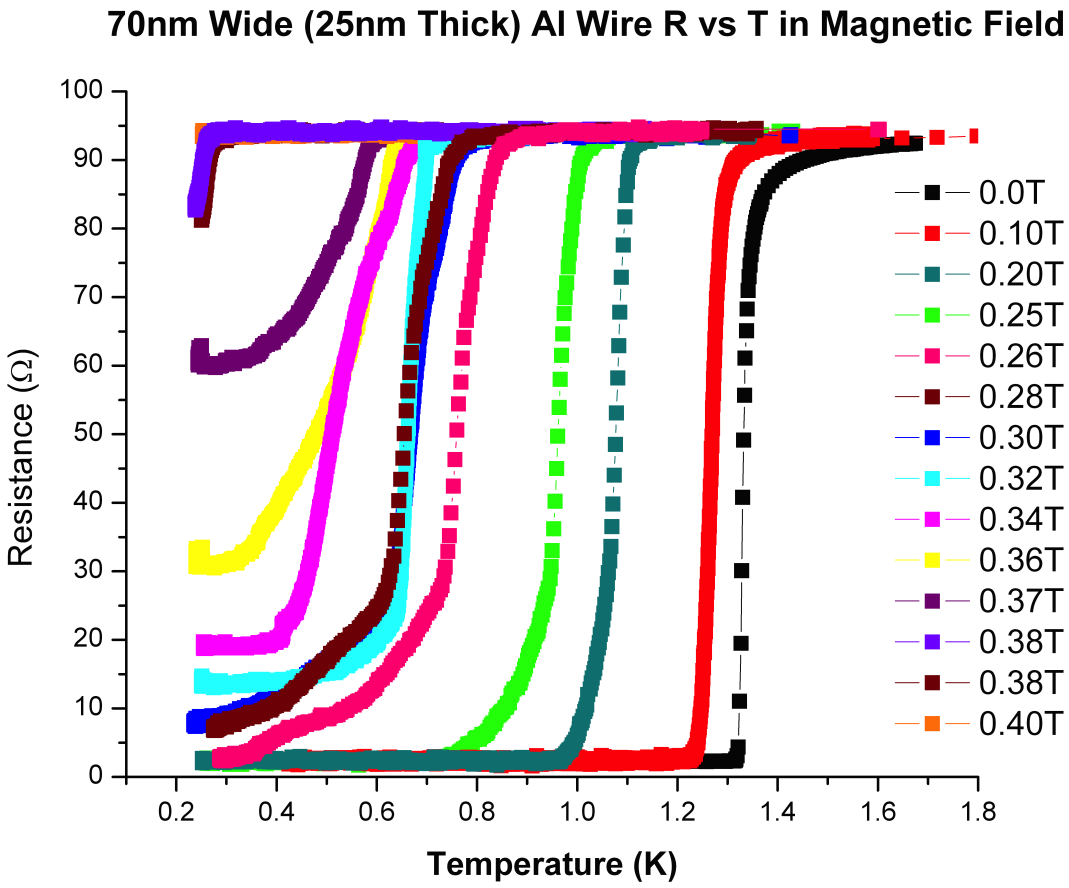

Figure 7.2: Resistance vs temperature for different magnetic fields

shows the resistance versus magnetic field data at 250mK. The wire transitions to an intermediate resistance flux flow state at 0.28T and then transitions to a normal state at 0.36T. This increasing magnetoresistance as a function of magnetic field in this flux flow regime is linear as predicted in the Bardeen-Stephen model (see Eqn. 2.41).

In order to fully understand what is going on with this flux flow state, we studied it over the full resistance versus field versus temperature phase diagram of the wire. Figure 7.2 shows the resistance vs temperature for many different fields for a thin,

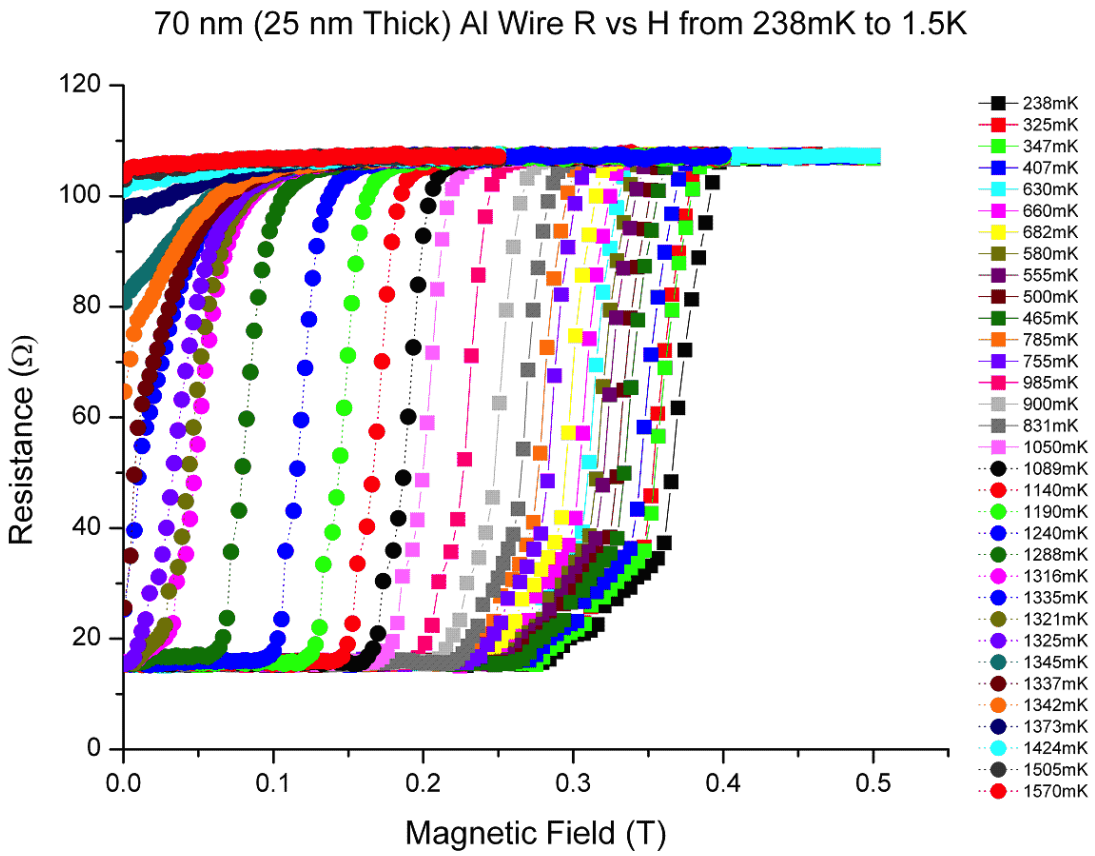

Figure 7.3: Resistance vs magnetic field for different temperatures. Note: 17 Ω base resistance is due to an offset on the lock-in and is not real. That resistance corresponds to zero.

narrow superconducting wire. The gradual widening at the bottom of the transition as the temperature rises shows the temperature dependence of the flux flow region for various set fields. There is a plateau in the resistance around 0.3T where the resistance is heading to some finite value as $T \to 0$. This feature will be explained as well as the small drop in resistance for the 0.38T field at 250mK when we arrive at the full 3D phase diagram in Figure 7.6.

More interestingly, in Figure 7.3 we have the resistance versus field for many

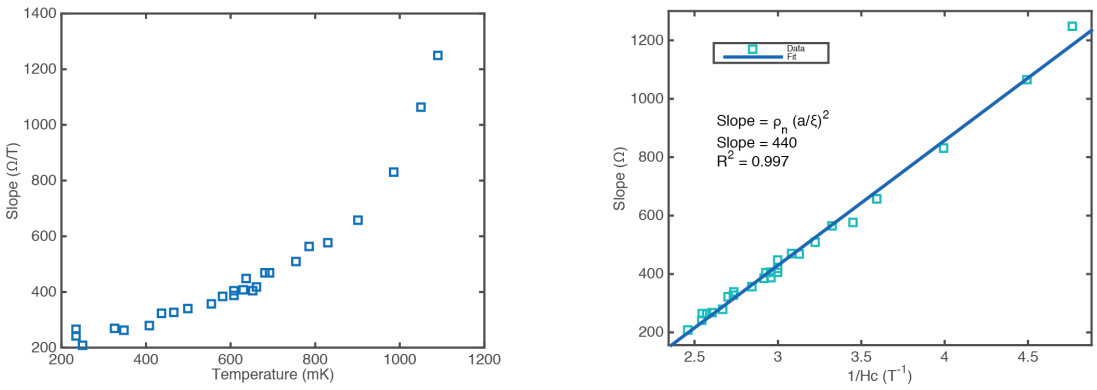

Figure 7.4: Slope of the flux flow magnetoresistance.

different temperatures for a thin, narrow superconducting wire in a field perpendicular to the wire. The "foot" at the bottom of the transition to the normal state marks the flux flow regime, where vortices are de-pinned and able to move freely across the wire. As the temperature rises, the critical field H_{c2} drops. The maximum flux flow resistance stays the same regardless of temperature; however, the slope of the flux flow magnetoresistance rises with the temperature.

We can see this clearly in Figure 7.4, where the slope of the flux flow region has been plotted both as both a function of temperature and the inverse critical field. Looking at this figure, we see that the slope as a function of $1/H_{c2}$ is linear. This is expected under the Bardeen-Stephen model (see Section 2.4.1). That model states that the flux flow resistance ρ_f should be

$$\rho_f = \rho_n \left(\frac{a}{\xi}\right)^2 \frac{B}{H_{c2}} \tag{7.1}$$

where a is the size of the vortex and ρ_n is the normal state resistance. By plotting

these slopes as a function of $1/H_{c2}$, the remarkably linear data that results suggests that the Bardeen-Stephen model is accurately representing our data.

The fact that there is an additional jump at $1/H_{c2}$ and the flux flow resistance does not smoothly join into the normal state resistance suggests under this model that the vortex size is in fact different than the coherence length. In addition, the changing value of the coefficient $\rho_n(a/\xi)^2$ means that the vortex size is growing linearly with $1/H_{c2}$. Since H_{c2} shrinks as we get closer to T_c, this means the vortex size should diverge at that point. This agrees with the divergence of $\lambda_L(T)$ at T_c (see Eqn. 2.7),[3] which is closely related to the size of the vortex.

7.1.2 Vortex Magnetoresistance

To better represent the resistance versus field data, Figure 7.5 shows the magnetoresistance curves plotted as a function of temperature. This shows the gradual widening of the flux flow region with decreasing temperature, as well as the shape of the superconducting, flux flow, and normal boundaries. In addition, a plateau/kink in the resistance appears at all temperatures at approximately 8Ω.

We can now understand the resistance versus temperature data by superimposing it on top of the 3D resistance vs field data. Figure 7.6 shows the magnetoresistance in dark blue and the resistance versus temperature data in light blue. The two axis commute in that we can see the temperature data are just cuts along the temperature axis through the magnetic field data. The reason for the plateaus in the temperature

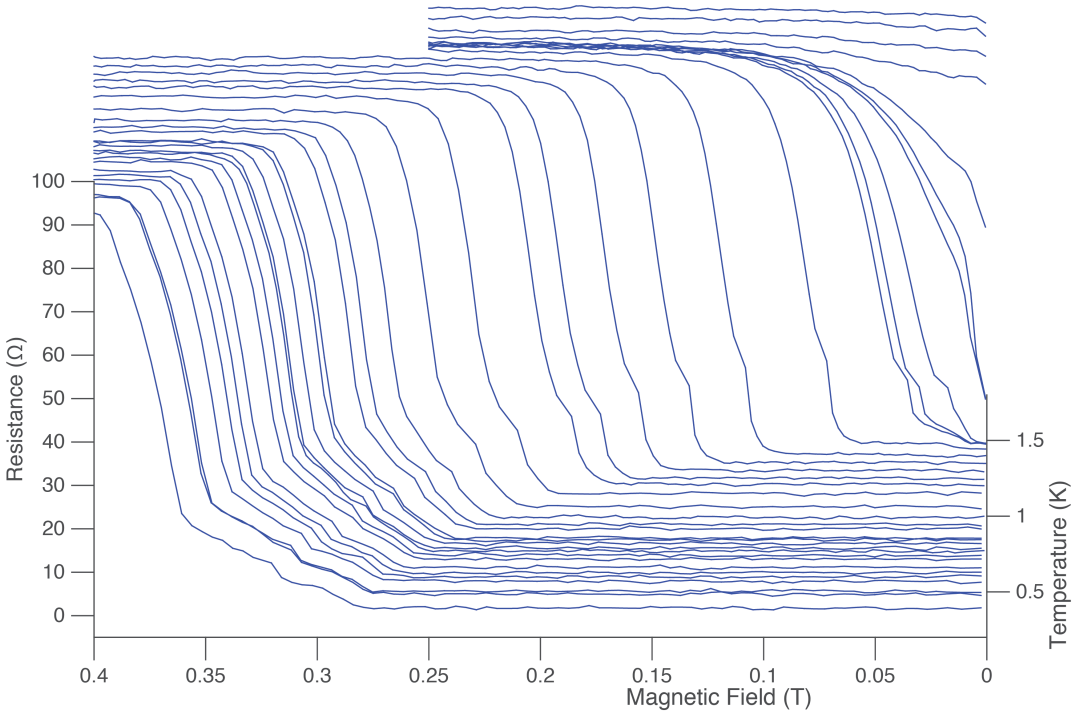

Figure 7.5: Resistance vs magnetic field for different temperatures, plotted with resistance on the z-axis.

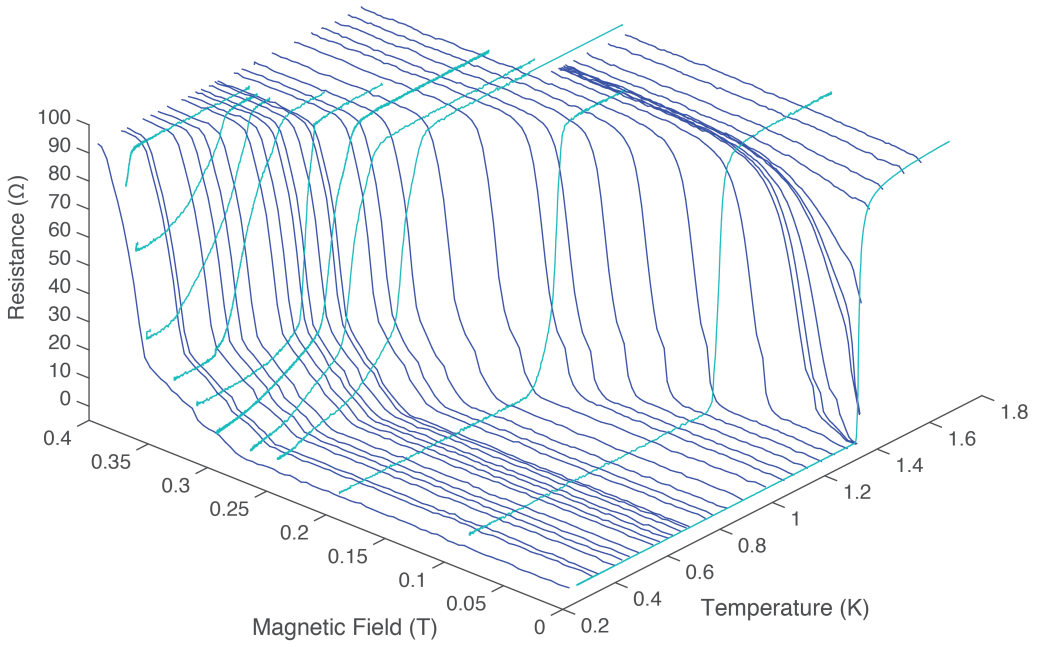

Figure 7.6: Resistance vs magnetic field at different temperatures as well as resistance vs temperature at different magnetic fields.

data is now clear: they are cuts through regions of constant flux flow resistance.

Figure 7.7 shows a color plot of the resistance vs magnetic field and temperature. This plot is created from the resistance vs field at different temperature data, with the area between each run's resistance interpolated from nearby data (low resolution is what results in the jumps near T_c). We can interpret these data as a phase diagram for the wire, as the regions of superconductivity, flux flow, and the normal state are clearly distinct. Part b) shows such a phase diagram superimposed on the color plot data. These data demonstrate three electronic phases of the material: The zero-

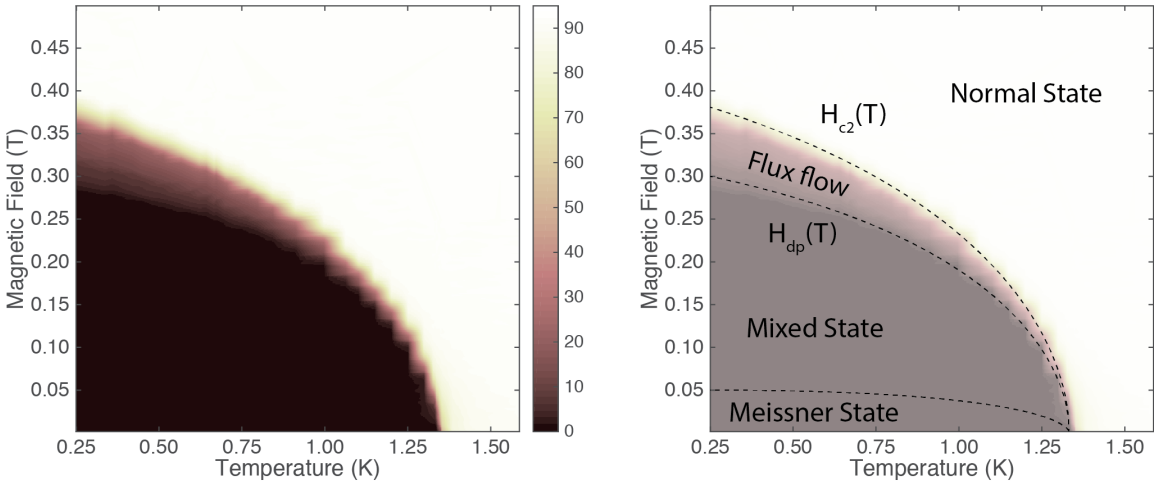

Figure 7.7: Resistance color plot and phase diagram for the flux flow device

resistance superconducting state, the flux flow state where vortices can move and thus produce a non-zero resistance, and the normal state after the critical field H_{C2}(T) is reached. Not visible in this color plot but inferred from current-voltage data is the switch from the Meissner state to the mixed state at 0.04T at 250mK (See Figure 7.8 for information).

Figure 7.8 shows the dV/dI characteristics for both the upsweep and the downsweep for the flux flow device. The two are distinct for low fields, as Joule heating in the wire means the re-trapping current on the downsweep will be much lower than the initial critical current. Part a) shows the initial upsweep in current in both directions for the flux flow device. As the field is increased, the critical current I_c (here plotted as the boundary between the blue and green regions) drops around 0.03T. This drop is associated with destroying the Meissner state and entering the mixed state for a type-II superconductor. Part b) is the dV/dI for the re-trapping current

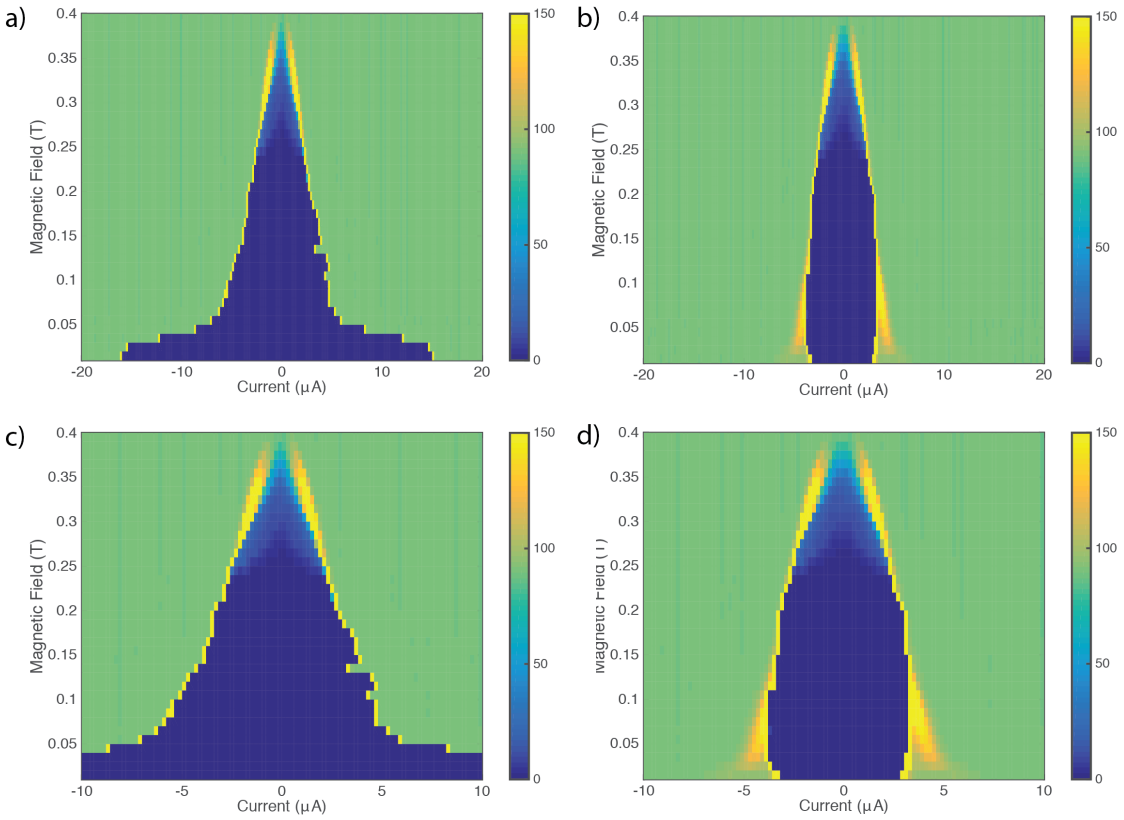

Figure 7.8: dV/dI for the flux flow device

in both directions for the flux flow device. Part c) is the zoomed in version of the upsweep data, showing the flux flow region (light blue regions) in more detail, and part d is the same but for the re-trapping current.

Figure 7.9 shows the resistance versus magnetic field for many different temperatures for a thin, narrow superconducting wire in a field parallel to the wire. This state differs from the perpendicular field data in that the current is not producing a Lorentz force on the vortices in the wire (as the current is running parallel to the field), so there is not the same region of flux flow as there is in the perpendicular field case.

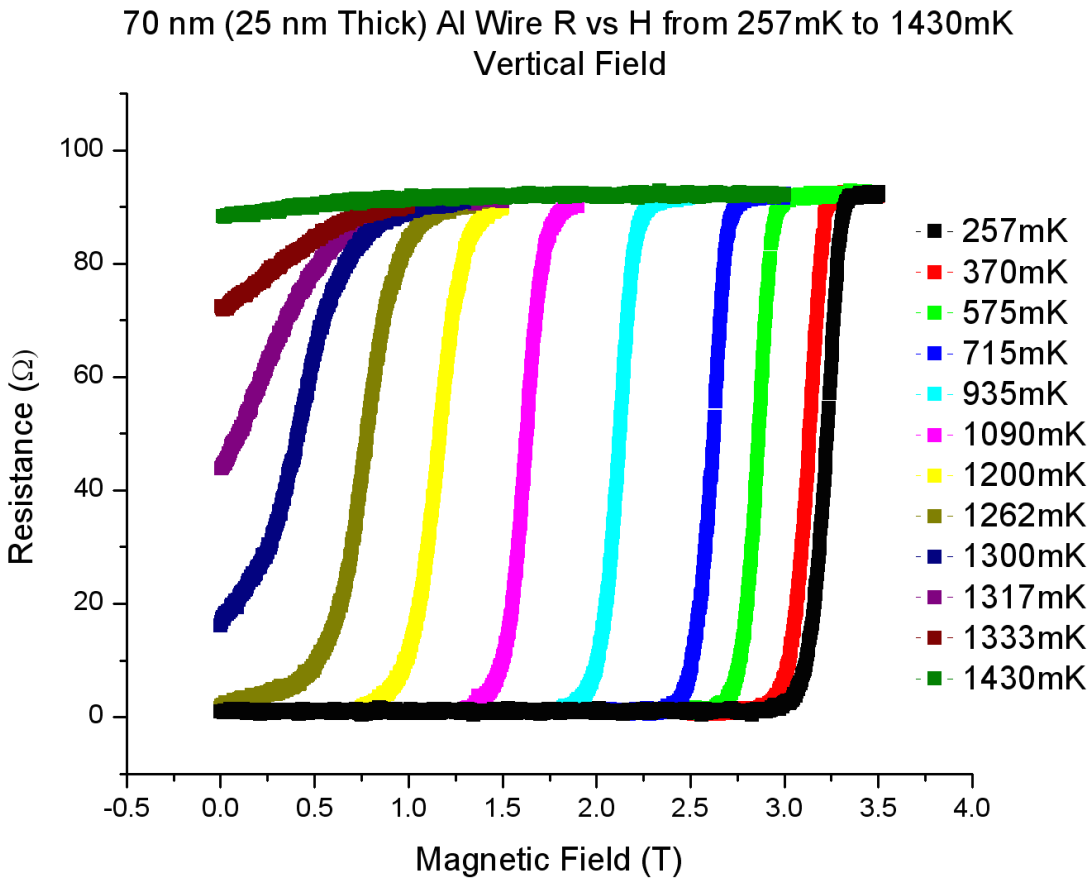

Figure 7.9: Resistance vs parallel magnetic field

Bibliography

[1] H. K. Onnes, *Leiden Comm*, vol. 21, 1911.

[2] W. Meissner and R. Ochesenfeld, *Naturwissenschaften*, vol. 21, p. 787, 1933.

[3] M. Tinkham, *Introduction to Superconductivity.* McGraw-Hill Inc., 1996.

[4] F. London and H. London, *Proc. Roy. Soc.*, vol. A149, p. 71, 1935.

[5] v. L. Ginzburg and L. D. Landau, *Zh. Eksperim. i. Teor. Fiz.*, vol. 20, p. 1064, 1950.

[6] J. Bardeen, N. L. Cooper, and J. R. Schrieffer, *Phys. Rev.*, vol. 108, p. 1175, 1957.

[7] J. Bardeen and M. J. . Stephen, *Phys. Rev.*, vol. 140, p. A1197, 1965.

[8] S. Yasin, D. G. Hasko, and H. Ahmed, "Fabrication of <5 nm width lines in poly(methylmethacrylate) resist using a water:isopropyl alcohol developer and ultrasonically-assisted development," *Applied Physics*

Letters, vol. 78, no. 18, pp. 2760–2762, 2001. [Online]. Available: http://scitation.aip.org/content/aip/journal/apl/78/18/10.1063/1.1369615

[9] M. J. Rooks, E. Kratschmer, R. Viswanathan, J. Katine, R. E. Fontana, and S. A. MacDonald, "Low stress development of poly(methylmethacrylate) for high aspect ratio structures," *Journal of Vacuum Science & Technology B*, vol. 20, no. 6, pp. 2937–2941, 2002. [Online]. Available: http://scitation.aip.org/content/avs/journal/jvstb/20/6/10.1116/1.1524971

[10] S. Yasin, D. G. Hasko, M. N. Khalid, D. J. Weaver, and H. Ahmed, "Influence of polymer phase separation on roughness of resist features," *Journal of Vacuum Science & Technology B*, vol. 22, no. 2, pp. 574–578, 2004. [Online]. Available: http://scitation.aip.org/content/avs/journal/jvstb/22/2/10.1116/1.1651106

[11] B. Cord, J. Lutkenhaus, and K. K. Berggren, "Optimal temperature for development of poly(methylmethacrylate)," *Journal of Vacuum Science & Technology B*, vol. 25, no. 6, pp. 2013–2016, 2007. [Online]. Available: http://scitation.aip.org/content/avs/journal/jvstb/25/6/10.1116/1.2799978

[12] G. Cannatá, G. Scandurra, and C. Ciofi, "An ultralow noise preamplifier for low frequency noise measurements," *Review of Scientific Instruments*, vol. 80, no. 11, pp. –, 2009. [Online]. Available: http://scitation.aip.org/content/aip/journal/rsi/80/11/10.1063/1.3258197

[13] Y. Oreg and A. M. Finkel'stein, "Suppression of T_c in superconducting

amorphous wires," *Phys. Rev. Lett.*, vol. 83, pp. 191–194, Jul 1999. [Online]. Available: http://link.aps.org/doi/10.1103/PhysRevLett.83.191

[14] C. N. Lau, N. Markovic, M. Bockrath, A. Bezryadin, and M. Tinkham, "Quantum phase slips in superconducting nanowires," *Phys. Rev. Lett.*, vol. 87, p. 217003, Nov 2001. [Online]. Available: http://link.aps.org/doi/10.1103/PhysRevLett.87.217003

[15] N. Markovic, C. N. Lau, and M. Tinkham, "The limits of superconductivity in MoGe nanowires," *Physica C*, vol. 387, p. 44, 2003.

[16] J. S. Langer and V. Ambegaokar, "Intrinsic resistive transition in narrow superconducting channels," *Phys. Rev.*, vol. 164, pp. 498–510, Dec 1967. [Online]. Available: http://link.aps.org/doi/10.1103/PhysRev.164.498

[17] D. E. McCumber and B. I. Halperin, "Time scale of intrinsic resistive fluctuations in thin superconducting wires," *Phys. Rev. B*, vol. 1, pp. 1054–1070, Feb 1970. [Online]. Available: http://link.aps.org/doi/10.1103/PhysRevB.1.1054

[18] D. S. Golubev and A. D. Zaikin, "Quantum tunneling of the order parameter in superconducting nanowires," *Phys. Rev. B*, vol. 64, p. 014504, Jun 2001. [Online]. Available: http://link.aps.org/doi/10.1103/PhysRevB.64.014504

[19] S. Sachdev, P. Werner, and M. Troyer, "Universal conductance of nanowires near the superconductor-metal quantum transition," *Phys. Rev. Lett.*, vol. 92,

p. 237003, Jun 2004. [Online]. Available: http://link.aps.org/doi/10.1103/PhysRevLett.92.237003

[20] G. Refael, E. Demler, and Y. Oreg, "Superconductor to normal-metal transition in finite-length nanowires: Phenomenological model," *Phys. Rev. B*, vol. 79, p. 094524, Mar 2009. [Online]. Available: http://link.aps.org/doi/10.1103/PhysRevB.79.094524

[21] I. F. Herbut, "Critical behavior at superconductor-insulator phase transitions near one dimension," *Phys. Rev. B*, vol. 58, pp. 971–981, Jul 1998. [Online]. Available: http://link.aps.org/doi/10.1103/PhysRevB.58.971

[22] A. Del Maestro, B. Rosenow, M. Müller, and S. Sachdev, "Infinite randomness fixed point of the superconductor-metal quantum phase transition," *Phys. Rev. Lett.*, vol. 101, p. 035701, Jul 2008. [Online]. Available: http://link.aps.org/doi/10.1103/PhysRevLett.101.035701

[23] N. Giordano, "Evidence for macroscopic quantum tunneling in one-dimensional superconductors," *Phys. Rev. Lett.*, vol. 61, pp. 2137–2140, Oct 1988. [Online]. Available: http://link.aps.org/doi/10.1103/PhysRevLett.61.2137

[24] A. Bezryadin and P. Goldbart, "Superconducting nanowires fabricated using molecular templates," *Advanced Materials*, vol. 22, p. 1111, 2010. [Online]. Available: http://dx.doi.org/10.1002/adma.200904353

[25] A. Bezryadin, L. C. N., and M. Tinkham, "Quantum suppression of superconductivity in ultrathin nanowires," *Nature*, vol. 404, p. 971, 2000. [Online]. Available: http://dx.doi.org/10.1038/35010060

[26] M. Tian, J. Wang, J. Snyder, J. Kurtz, Y. Liu, P. Schiffer, T. Mallouk, and M. H. W. Chan, "Synthesis and characterization of superconducting single-crystal Sn nanowires," *Applied Physics Letters*, vol. 83, p. 1620, 2003. [Online]. Available: http://dx.doi.org/10.1063/1.1601692

[27] S. Michotte, S. Matefi-Tempfli, and L. Piraux, "Currentvoltage characteristics of Pb and Sn granular superconducting nanowires," *Applied Physics Letters*, vol. 82, p. 4119, 2003.

[28] D. Natelson, R. L. Willett, K. W. West, and L. N. Pfeiffer, "Fabrication of extremely narrow metal wires," *Applied Physics Letters*, vol. 77, p. 1991, 2000.

[29] F. Altomare, A. M. Chang, M. R. Melloch, Y. Hong, and C. W. Tu, "Ultranarrow AuPd and Al wires," *Applied Physics Letters*, vol. 86, p. 172501, 2005.

[30] M. Zgirski, K.-P. Riikonen, V. Tuboltsev, P. Jalkanen, T. T. Hongisto, and K. Y. Arutyunov, "Ion beam shaping and downsizing of nanostructures," *Nanotechnology*, vol. 19, p. 055301, 2008.

[31] W. W. Hu, K. Sarveswaran, M. Lieberman, and G. H. Bernstein, "Sub-10 nm electron beam lithography using cold development of poly(methylmethacrylate),"

Journal of Vacuum Science & Technology B, vol. 22, no. 4, pp. 1711–1716, 2004. [Online]. Available: http://scitation.aip.org/content/avs/journal/jvstb/22/4/10.1116/1.1763897

[32] E. Deltombe and M. Pourbaix, "The electrochemical behavior of aluminum: potential pH diagram of the system Al-H2 at 25 C," *Corrosion*, vol. 14, pp. 496–500, 1958.

[33] J. Pearl, "Current distribution in superconducting films carrying quantized currents," *Appl.Phys. Lett.*, vol. 5, pp. 65–66, 1964. [Online]. Available: http://scitation.aip.org/content/aip/journal/apl/5/4/10.1063/1.1754056

[34] V. V. Moshchalkov, L. Gielen, C. Strunk, R. Jonckheere, X. Qiu, C. Van Haesendonck, and Y. Bruynseraede, "Effect of sample topology on the critical fields of mesoscopic superconductors," *Nature*, vol. 373, p. 319, 1995. [Online]. Available: http://www.nature.com/nature/journal/v373/n6512/pdf/373319a0.pdf

[35] M. V. Milošević, A. Kanda, S. Hatsumi, F. M. Peeters, and Y. Ootuka, "Local current injection into mesoscopic superconductors for the manipulation of quantum states," *Phys. Rev. Lett.*, vol. 103, p. 217003, Nov 2009. [Online]. Available: http://link.aps.org/doi/10.1103/PhysRevLett.103.217003

[36] B. Xu, M. V. Milošević, S.-H. Lin, F. M. Peeters, and B. Jankó, "Formation of multiple-flux-quantum vortices in mesoscopic superconductors

from simulations of calorimetric, magnetic, and transport properties," *Phys. Rev. Lett.*, vol. 107, p. 057002, Jul 2011. [Online]. Available: http://link.aps.org/doi/10.1103/PhysRevLett.107.057002

[37] D. Y. Vodolazov, "Vortex-induced negative magnetoresistance and peak effect in narrow superconducting films," *Phys. Rev. B*, vol. 88, p. 014525, Jul 2013. [Online]. Available: http://link.aps.org/doi/10.1103/PhysRevB.88.014525

[38] D. Pekker, G. Refael, and P. M. Goldbart, "Weber blockade theory of magnetoresistance oscillations in superconducting strips," *Phys. Rev. Lett.*, vol. 107, p. 017002, Jun 2011. [Online]. Available: http://link.aps.org/doi/10.1103/PhysRevLett.107.017002

[39] R. Cordoba, T. I. Baturina, J. Sese, A. Yu Mironov, J. M. De Teresa, M. R. Ibarra, D. A. Nasimov, A. K. Gutakovskii, A. V. Latyshev, I. Guillamn, H. Suderow, S. Vieira, M. R. Baklanov, J. J. Palacios, and V. M. Vinokur, "Magnetic field-induced dissipation-free state in superconducting nanostructures," *Nat. Comm.*, vol. 4, p. 1437, 2013. [Online]. Available: http://dx.doi.org/10.1038/ncomms2437

[40] Y. Atzmon and E. Shimshoni, "Superconductor-insulator transitions and magnetoresistance oscillations in superconducting strips," *Phys. Rev. B*, vol. 83, p. 220518, Jun 2011. [Online]. Available: http://link.aps.org/doi/10.1103/PhysRevB.83.220518

[41] ——, "Alternating superconductor-insulator transport characteristics in a quantum vortex chain," *Phys. Rev. B*, vol. 85, p. 134523, Apr 2012. [Online]. Available: http://link.aps.org/doi/10.1103/PhysRevB.85.134523

[42] A. Johansson, G. Sambandamurthy, D. Shahar, N. Jacobson, and R. Tenne, "Nanowire acting as a superconducting quantum interference device," *Phys. Rev. Lett.*, vol. 95, p. 116805, Sep 2005. [Online]. Available: http://link.aps.org/doi/10.1103/PhysRevLett.95.116805

[43] M. P. A. Fisher, "Quantum phase transitions in disordered two-dimensional superconductors," *Phys. Rev. Lett.*, vol. 65, pp. 923–926, Aug 1990. [Online]. Available: http://link.aps.org/doi/10.1103/PhysRevLett.65.923

[44] C. W. J. Beenakker, "Theory of coulomb-blockade oscillations in the conductance of a quantum dot," *Phys. Rev. B*, vol. 44, pp. 1646–1656, Jul 1991. [Online]. Available: http://link.aps.org/doi/10.1103/PhysRevB.44.1646

[45] D. Saint-James and P. G. de Gennes, "Onset of superconductivity in decreasing fields," *Phys. Lett.*, vol. 7, p. 306, 1963. [Online]. Available: http://www.sciencedirect.com/science/article/pii/0031916363900477

[46] M. Tinkham, J. U. Free, C. N. Lau, and N. Markovic, "Hysteretic I-V curves of superconducting nanowires," *Phys. Rev. B*, vol. 68, p. 134515, Oct 2003. [Online]. Available: http://link.aps.org/doi/10.1103/PhysRevB.68.134515

[47] J. Romijn, T. M. Klapwijk, M. J. Renne, and J. E. Mooij, "Critical pair-breaking current in superconducting aluminum strips far below T_c," *Phys. Rev. B*, vol. 26, pp. 3648–3655, Oct 1982. [Online]. Available: http://link.aps.org/doi/10.1103/PhysRevB.26.3648

[48] K. K. Likharev, "The formation of a mixed state in planar superconductor films," *Sov. Radiophys.*, vol. 14, p. 722, 1972.

[49] M. Benkraouda and J. R. Clem, "Critical current from surface barriers in type-II superconducting strips," *Phys. Rev. B*, vol. 58, pp. 15 103–15 107, Dec 1998. [Online]. Available: http://link.aps.org/doi/10.1103/PhysRevB.58.15103

[50] G. Maksimova, "Mixed state and critical current in narrow semiconducting films," *Physics of the Solid State*, vol. 40, no. 10, pp. 1607–1610, 1998. [Online]. Available: http://dx.doi.org/10.1134/1.1130618

[51] P. Sánchez-Lotero and J. J. Palacios, "Critical fields for vortex expulsion from narrow superconducting strips," *Phys. Rev. B*, vol. 75, p. 214505, Jun 2007. [Online]. Available: http://link.aps.org/doi/10.1103/PhysRevB.75.214505

[52] E. Bronson, M. P. Gelfand, and S. B. Field, "Equilibrium configurations of pearl vortices in narrow strips," *Phys. Rev. B*, vol. 73, p. 144501, Apr 2006. [Online]. Available: http://link.aps.org/doi/10.1103/PhysRevB.73.144501

[53] J. J. Palacios, "Vortex lattices in strong type-II superconducting two-

dimensional strips," *Phys. Rev. B*, vol. 57, pp. 10 873–10 876, May 1998. [Online]. Available: http://link.aps.org/doi/10.1103/PhysRevB.57.10873

[54] G. R. Berdiyorov, X. H. Chao, F. M. Peeters, H. B. Wang, V. V. Moshchalkov, and B. Y. Zhu, "Magnetoresistance oscillations in superconducting strips: A ginzburg-landau study," *Phys. Rev. B*, vol. 86, p. 224504, Dec 2012. [Online]. Available: http://link.aps.org/doi/10.1103/PhysRevB.86.224504

[55] G. M. Maksimova, N. V. Zhelezina, and I. L. Maksimov, "Critical current and negative magnetoresistance of superconducting film with edge barrier," *EPL (Europhysics Letters)*, vol. 53, no. 5, p. 639, 2001. [Online]. Available: http://stacks.iop.org/0295-5075/53/i=5/a=639

[56] I. Aranson, M. Gitterman, and B. Y. Shapiro, "Onset of vortices in thin superconducting strips and wires," *Phys. Rev. B*, vol. 51, pp. 3092–3096, Feb 1995. [Online]. Available: http://link.aps.org/doi/10.1103/PhysRevB.51.3092

[57] A. V. Kuznetsov, D. V. Eremenko, and V. N. Trofimov, "Onset of flux penetration into a thin superconducting film strip," *Phys. Rev. B*, vol. 59, pp. 1507–1513, Jan 1999. [Online]. Available: http://link.aps.org/doi/10.1103/PhysRevB.59.1507

[58] G. Stan, S. B. Field, and J. M. Martinis, "Critical field for complete vortex expulsion from narrow superconducting strips," *Phys. Rev. Lett.*, vol. 92,

p. 097003, Mar 2004. [Online]. Available: http://link.aps.org/doi/10.1103/PhysRevLett.92.097003

[59] B. L. T. Plourde, D. J. Van Harlingen, D. Y. Vodolazov, R. Besseling, M. B. S. Hesselberth, and P. H. Kes, "Influence of edge barriers on vortex dynamics in thin weak-pinning superconducting strips," *Phys. Rev. B*, vol. 64, p. 014503, Jun 2001. [Online]. Available: http://link.aps.org/doi/10.1103/PhysRevB.64.014503

[60] J. Gutierrez, B. Raes, J. Van de Vondel, A. V. Silhanek, R. B. G. Kramer, G. W. Ataklti, and V. V. Moshchalkov, "First vortex entry into a perpendicularly magnetized superconducting thin film," *Phys. Rev. B*, vol. 88, p. 184504, Nov 2013. [Online]. Available: http://link.aps.org/doi/10.1103/PhysRevB.88.184504

[61] G. Stejic, A. Gurevich, E. Kadyrov, D. Christen, R. Joynt, and D. C. Larbalestier, "Effect of geometry on the critical currents of thin films," *Phys. Rev. B*, vol. 49, pp. 1274–1288, Jan 1994. [Online]. Available: http://link.aps.org/doi/10.1103/PhysRevB.49.1274

[62] C. P. Bean and J. D. Livingston, "Surface barrier in type-II superconductors," *Phys. Rev. Lett.*, vol. 12, pp. 14–16, Jan 1964. [Online]. Available: http://link.aps.org/doi/10.1103/PhysRevLett.12.14

[63] L. P. Gor'kov and N. B. Kopnin, "Vortex motion and resistivity of type-ll superconductors in a magnetic field," *Soviet Physics Uspekhi*, vol. 18, no. 7, p. 496, 1975. [Online]. Available: http://stacks.iop.org/0038-5670/18/i=7/a=R02

Vita

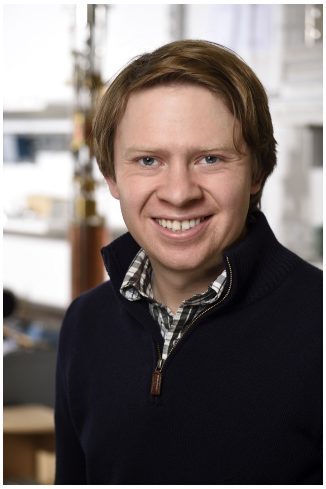

Tyler Thomas Morgan-Wall was born in 1987 in Horsham, Pennsylvania. After graduating from Hatboro-Horsham High School in 2005, he attended the University of Pennsylvania in Philadelphia, PA. In 2009 he graduated from the University of Pennsylvania *cum laude* with a Bachelor of Arts degree in Physics with a minor in Mathematics. He then moved to Baltimore, MD and began a doctoral program in condensed matter physics at Johns Hopkins University working under Nina Marković on the transport properties of superconducting nanodevices. He received his Ph.D. in Physics from Johns Hopkins in May of 2015.